PHAGOCYTIC ASTROCYTES AND THE FORMATION OF LIPID DROPLETS IN THE MYELINATION TRANSITION ZONE OF THE OPTIC NERVE HEAD IN THE DBA/2J MOUSE GLAUCOMA MODEL

by

Judy V. Nguyen

A dissertation submitted to Johns Hopkins University in conformity with the requirements for the degree of Doctor of Philosophy

Baltimore, Maryland

August, 2014

Abstract

Glaucoma is a progressive disease that results in the degeneration of retinal ganglion cells and their axons, which make up the optic nerve. From the comparative analysis of degeneration patterns in the retina and of the axons directly exiting the retina, it has been proposed that damage to the axons in the optic nerve head occurs before the loss of retinal ganglion cells. Therefore, the focus of this dissertation was to identify biology in the optic nerve head that might contribute to the development of glaucoma.

The phagocytic activity of astrocytes was discovered by studying the effects of disease and injury on the cells in the optic nerve using genetic and acute mouse models. These astrocytes were initially identified by the expression of *Lgals3*, a phagocytosis-related gene more commonly found in phagocytes. Astrocytes had specific *Lgals3* expression in the myelination transition zone that increased in mouse models of glaucoma. Further analysis of myelination transition zone astrocytes using electron microscopy revealed the presence of axonal debris, myelin remnants, and lipid droplets inside the astrocyte cytoplasm. Primary astrocyte cultures demonstrated that continuous and repeated phagocytosis of myelin induced lipid droplet formation.

These studies describe a dynamic role of astrocytes in optic nerve biology. Optic nerve astrocytes actively phagocytose myelin and, in disease, do so to the point that the myelin accumulates within the cell and lipid droplets form. Further investigations of myelin stability and astrocyte phagocytosis may lead to new clues in the progression of axon damage, while understanding lipid droplet biology in the optic nerve might lead to the identification of biomarkers in glaucoma.

Acknowledgements

I never imagined that I would have the opportunity to earn a Ph.D. It has been an incredible and unforgettable experience. I would like to first thank my thesis advisor, Nicholas Marsh-Armstrong, for giving me the chance to work with him in his lab. He has provided guidance, understanding, and patience during the course of my studies. Every graduate student's journey is unique and I am very grateful that Nick has been so accommodating of my needs. I have been able to learn and grow as a scientist and as a person from working with him.

I have spent a significant amount of time in lab with some very talented and hard-working people. I would like to thank and acknowledge my fellow graduate student Elizabeth Mills, for always being willing to lend a helping hand and for her generosity in always providing the lab with weekly treats and birthday specials; Chung-ha Davis for his friendship and willingness to go the extra mile to complete what is necessary; Shannon Emmel for being a fellow cat lover and always a source for interesting and insightful conversation; Pooja Karukonda for her help with experiments and being a wonderful labmate.

I would like to thank Jonathan Pevsner, Mollie Meffert, and Solomon Snyder for allowing me to rotate in their labs. I would also like to thank my thesis committee members, Donald Zack, Dwight Bergles, and Michael Wolfgang for their support and insights. I would like to thank Paul Watkins for always entertaining my office visits and for his invaluable help in giving my project direction from the very beginning, and Derek Welsbie for his thoughtfulness and good-natured patience in reading my thesis.

My graduate student career would have not been possible without the Biochemistry, Cellular, and Molecular Biology program at Johns Hopkins University School of Medicine and the people that were fundamental to my admission and graduation: Jeffrey Corden, Carolyn Machamer, Leslie Brown, Sharon Root, Margie Policastri, Arhonda Gogos, Jess Rexroad, and members of the admissions committee. I would also like to thank the Solomon H. Snyder Department of Neuroscience, the Hugo W. Moser Research Institute at Kennedy Krieger, and the people working within those departments, for being my second and third academic homes.

I would like to thank my friends and fellow BCMB alumni Kipchirchir Bitok and Sharrol Bachus for leading by example with their dedication, perseverance, and intelligence. I also thank Valentin Sluch, who was my fellow Oklahoman in Baltimore and always had an interesting perspective to offer.

I would like to thank Laurence Frelin, who was the first friend I made at Hopkins. I am so lucky that we were able to find a common interest in food. Larry has helped me through so many things, both inside and outside the lab. My time at Hopkins would not have been the same without him.

I was able to develop my fundamental technical and troubleshooting skills under the guidance of Susannah Rankin at the Oklahoma Medical Research Foundation. I am very grateful for her patience in my scientific training, and her encouragement and support to apply to graduate school and “go big”. Without the recommendations from Susannah, Dean Dawson, and Richard Broughton, I would mostly likely be in a different place today.

I would like to thank my family, who supported my desire to go into research without question. I would especially like to thank my father, Thu Nguyen, who helped me start my new life in Baltimore with as little worries as possible. To my stepmother Hong Le, brothers Viet and Thanh, and sisters Linh and Theresa, thank you for your support and for being proud of me. Thank you to my late mother, The Nguyen, for teaching me about hard work and sacrifice from an early age. I will always remember your fierce pride and the lesson you taught me that no job was small or insignificant.

Lastly, I would like to thank Truong Tran for showing me the meaning of unconditional love. Words cannot express how much you have impacted my life. It was always a privilege to be your friend and now it is an honor to share the rest of my life with you. You are my hero. I look forward to our adventures together.

Table of Contents

List of Figures

List of Abbreviations

aa	Amino acid
Abca1	ATP-binding cassette transporter, sub-family A, member 1
Aldh1L1	Aldehyde dehydrogenase 1 family, member L1
Atgl	Adipose triglyceride lipase
Ced	Cell death abnormal
CNS	Central nervous system
D2	DBA/2J
D2-Gpnmb$^+$	DBA/2J-Gpnmb$^+$/SjJ
GFAP	Glial fibrillary acidic protein
GFP	Green fluorescent protein
GLAST/EAAT1	Glutamate aspartate transporter/ Excitatory amino-acid transporter 1
GLT-1/EAAT2	Glial glutamate transporter 1/Excitatory amino-acid transporter 2
HSV-TK	Herpes simplex virus thymidine kinase
Iba1	Ionized calcium binding adapter molecule 1
iNOS	Inducible nitric oxide synthase
eNOS	Endothelial nitric oxide synthase
nNOS	Neuronal nitric oxide synthase
IOP	Intraocular pressure
IPD	Iris pigment dispersion
ISA	Iris stromal atrophy
Lgals3	Galectin-3/Mac-2
Lrp1	Low density lipoprotein receptor-related protein 1

Megf10	Multiple EGF-like-domains 10
Mertk	C-mer proto-oncogene tyrosine kinase
Mfge8	Milk fat globule-EGF factor 8 protein
MLG	Milk lipid globule secretion
mRNA	Messenger RNA
mSOG	Mini Singlet Oxygen Generator
MSV	Multiple segmentation values
MTZ	Myelination transition zone
NAC	Non-A beta component
NACP precursor	Non-A beta component of Alzheimer’s disease amyloid
NND	No noticeable degeneration
ONH	Optic nerve head
PACG	Primary angle closure glaucoma
POAG	Primary open angle glaucoma
PD	Parkinson’s disease
PK	Proteinase K
Plin	Perilipin
pNF	Phosphorylated neurofilament
RGC	Retinal ganglion cell
ROS	Reactive oxygen species
SBEM	Serial block-face scanning electron microscopy
SNARE protein receptor	Soluble N-ethylmaleimide-sensitive factor attachment
SNAP-23	Synaptosomal-associated protein 23
Snca	Alpha synuclein

Sncb	Beta synuclein
Sncg	Gamma synuclein
SV	Segmentation value
Syn	Synuclein
TEM	Transmission electron microscopy
Thy1	Thymocyte differentiation antigen 1
TNFα	Tumor necrosis factor, alpha
xSncg	*Xenopus tropicalis* Sncg

Chapter 1: Introduction

Introduction to glaucoma

Glaucoma is an optic neuropathy that is one of the leading causes of blindness in the world [1]. It is an irreversible disease that interferes with the processing and transmission of images from the retina to the brain due to the death of retinal ganglion cells (RGCs). Glaucoma primarily affects the elderly population and risk factors include elevated intraocular pressure (IOP) and excavation of the optic disk.

Elevated IOP is typically due to the decreased outflow of the aqueous humor. When the angle between the iris and cornea is narrowed or closed, this is diagnosed as primary angle closure glaucoma (PACG). The angle remains open in primary open angle glaucoma (POAG) and microscopic blockage in the trabecular meshwork reduces the outflow pathway. Secondary glaucoma may result from anterior synechia, which is when the iris presses anteriorly against the cornea or trabecular meshwork. Glaucoma can also occur in eyes with normal pressure. IOP modulation through pharmacological agents or surgery is currently the only method that has shown to be effective in the treatment of glaucoma, even though the mechanism is not well understood [2].

Excavation of the optic disk is also known as cupping. The optic cup is the central region of the optic disk and there is an increase in the ratio of the optic cup to the optic disk that can be observed in glaucoma. The region between the cup and disk is the neuroretinal rim. The neuroretinal rim also decreases with optic disk cupping. Altogether these signs can indicate damage to the lamina cribrosa and optic nerve [3-5], but the appearance of the optic disk is variable and is insufficient to diagnose on that parameter alone. Cupping is thought to occur due to elevated IOP deforming the lamina cribrosa, which is a collagenous structure that axons pass through before forming the optic nerve. However, optic disk cupping also occurs without elevated IOP.

There are two important observations that have framed the direction of glaucoma research. The first observation is that RGC loss in the retina occurs in a particular arcuate pattern [6; 7]. In animal models, RGC loss is seen as a sectorial pattern [8-12]. The regions of RGC loss are well-defined and, in humans, the arcuate pattern of RGC death typically does not cross the horizontal meridian. The reason for these observations is that there is a spatial relationship between RGCs somas and their axon bundles in the optic nerve head (ONH) [13-15]. Axon bundles at the superior or inferior poles of the optic disk correspond to RGCs that are superior or inferior, respectively, to the horizontal meridian. Therefore an injury which affects the axons in the ONH is likely the cause of the pattern of RGC death observed in glaucoma.

The optic nerve head

The ONH is the region of interest in this thesis because of the likelihood that the injury that initiates glaucoma occurs here. The most anterior portion of the ONH is the pre-laminar region, which contains bundles of axons that have emerged from the retinal nerve fiber layer (NFL) and are exiting the optic disk. Posterior to the pre-laminar region is the laminar region which contains the lamina cribrosa. Mice do not have a collagenous lamina cribrosa [3; 12; 15; 16] and this region has been referred to as the glial lamina to make that distinction [12; 15]. In humans and other mammals including mice, the axons in the pre-laminar and laminar region are unmyelinated [3].

Myelination of the optic nerve begins distally and proceeds proximally, in contrast to other nerves in the central nervous system (CNS) where myelination begins near the cell body and myelinates in a distal direction [17]. In humans, myelination reaches up to the retrolaminar optic nerve, which begins at the posterior edge of the lamina cribrosa. In mice, there is a more gradual transition region and myelination completely ends further posteriorly to the sclera than in humans [16]. This region has been referred to as the retina-optic nerve junction [18; 19] and we have referred to this region as the myelination transition zone (MTZ) [11]. In this thesis, the region from the pre-lamina to the posterior edge of the retrolaminar region is included when referring to the ONH.

Mouse models of glaucoma

Animal models are essential to understanding the molecular mechanisms of glaucoma or any other disease. Primates, dogs, cats, pigs, and rodents have all been used to study glaucoma [20]. Animal models allow researchers to address specific questions to learn more about glaucoma, but researchers must be vigilant in extending the results to humans due inherent biological differences between humans and animals. The anatomy of the rodent eye, optic nerve, and aqueous humor dynamics are similar to human [21; 22], except that rodents have less developed lamina cribrosas which lack collagen beams [3; 12; 15; 16; 23]. Primate eye anatomy is most similar to humans, especially in the structure of the lamina cribrosa. Surgical manipulations can be easier to perform on primates due to their relatively large size, but the ethical and financial cost to support a large primate colony limits how many biological replicates are feasible to perform. Rodents are much more amenable to experimentation because they can be kept in higher population numbers and cost less to maintain. The methods to genetically manipulate mice and rats have also been well-developed. This thesis relies on the DBA/2J (D2) mouse strain as a model for glaucoma. As such, the D2 model is described in more detail and alternative mouse models are briefly discussed.

DBA/2J glaucoma model

The work to establish D2 as a glaucoma model has largely been pioneered by Simon W. M. John and colleagues [24-26]. D2 is an inbred mouse strain that spontaneously develops signs similar to iridocorneal endothelial syndrome and pigment dispersion syndrome in humans [24]. These signs develop with age and have varying degrees of penetrance, despite the genetically identical nature of the strain. The genetics of D2 simplify the model in some ways, but the variability of a disease phenotype demonstrates that there are influences yet to be uncovered. These influences may be insightful in the application of D2 findings in a human population.

D2: Iris defects

Slit lamp examination of 3-6 month (mo) old D2 revealed transillumination defects from the deterioration of the iris stroma and iris pigmented epithelial cells [24; 27]. The free-floating iris pigments may become trapped in the trabecular meshwork and block the pores that drain the aqueous humor. Iris displacement can also result in synechia that prevents the flow of aqueous humor through the chambers and out the trabecular meshwork. Pigment dispersion or synechia can lead to elevated IOP in D2, which is similar to pigmentary glaucoma or closed angle glaucoma, respectively [24].

D2: Genetics

In order to identify the genetics behind iris stromal atrophy (ISA) and iris pigment dispersion (IPD), D2 mice were crossed with C57Bl/6J mice and examined for signs of glaucoma [25]. Mice displaying iris abnormalities were analyzed using microsatellite markers and segregating coat colors. All the mice with iris defects were homozygous for two loci inherited from D2 and had brown coat colors instead of the typical black coat of C57Bl/6J mice. The loci were isolated from each other using genetic crosses and the inheritance of recessive genes in either loci produced a phenotype that was reflective of ISA or IPD.

The ISA locus contained the gene tyrosinase-related protein 1 (*Tyrp1*) [25; 26]. The *Tyrp1*^{b} allele in D2 contained two amino acid substitutions as compared with the C57Bl/6J allele. This gene is involved in the production of melanin and produces a brown pigment. *Tyrp1*^{b} alleles are also responsible for the brown coat color in D2 mice. Defects in *Tyrp1* was proposed to allow toxic intermediates of melanin production to form and cause damage to the melanocytes [28]. Interestingly, the *Tyrp1*^{b} allele is only toxic when the pigment forming pathway is activated. *Tyrp1*^{b} in albino BALB/cByJ does not cause ISA [25]. ISA was induced with the addition of a functional *Tyrp1* gene in the same BALB/cByJ background strain. *Tyrp1*^{b} has a direct role in the formation of ISA in D2.

The gene identified in the *ipd* locus was glycosylated protein nmb (*Gpnmb*) [29]. The D2 allele, *Gpnmb*^{R150X}, encoded a premature stop codon. *Gpnmb*^{R150X}, like *Tyrp1*^{b}, also appeared to induce toxicity through pigment production. A naturally occurring D2 strain with hypopigmentation called pearl (D2-*pe*) was used to show that reduced pigment production can negate the effects of *Gpnmb*^{R150X} or *Tyrp1*^{b} expression. Signs of glaucoma did not manifest in D2-*pe* unless at least one copy of *pe* was corrected to wildtype. Lower pigment production prevented the manifestation of glaucoma signs in mice with *Gpnmb*^{R150X} and *Tyrp1*^{b} mutations.

D2.B6-*Tyrp1*^{B6}*Gpnmb*^{B6}/Sj (D2.*Tyrp1*^{B6}*Gpnmb*^{B6}) mice were generated to better understand the contribution of these two genes to glaucomatous pathology [30]. The mice also provide the benefit of being a control strain to D2. The wildtype alleles were obtained from C57Bl/6J mice. There is predicted to be no more than 3.3% of C57Bl/6J DNA in D2.*Tyrp1*^{B6}*Gpnmb*^{B6}. Mice up to 12-mos-old did not have the appearance of iris disease, IOP elevation, or ocular degeneration [30]. Mice that were 16 to 21-mos old did develop some signs of degeneration, but the frequency was low and might be attributed to old age.

A second strain generated as a control to D2 was D2-*Gpnmb*$^{+}$/Sj (D2-Gpnmb^{+}). This *Gpnmb*$^{+}$ allele was present in ancestral D2 mouse strains before the *Gpnmb*^{R150X} mutation occurred [26]. The only known difference between D2 and D2-Gpnmb^{+} is the base in *Gpnmb*$^{+}$ that reverts the premature stop codon back to an arginine. D2-Gpnmb^{+} have mild signs of ISA but do not generally develop the signs of glaucoma [30]. As in D2.*Tyrp1*^{B6}*Gpnmb*^{B6}, there were a few instances that disease was observed. This may be attributed to the *Tyrp1*^{b} allele or other age-related biology. The ability to use age-matched mice that are genetically controlled to D2 expands the usefulness of D2 as a model. Control strains decrease the variabilities that might arise from comparing mice of difference ages or with different genetics. The studies performed in this thesis infrequently used young D2 mice in comparison with aged D2, and primarily utilized age-matched D2-*Gpnmb*$^{+}$.

D2: Glaucomatous degeneration

Elevated IOP occurred at approximately 6 to 9 mos of age [24; 27]. Female mice tended to have iris defects and elevated IOP earlier than males, but the two groups were not significantly different in terms of histology. The severity of degeneration within a cohort of similarly aged mice can be grouped into stages from no or early signs of degeneration (NOE) to severe [8; 27]. These groupings apply to both retinas and optic nerves.

Progressive thinning of the NFL, RGC layer, and inner nuclear layer (INL), as well as cupping of the optic disk were seen in sagittal sections [24; 27]. By 10 mos of age, 34% of D2 had severe loss while 55% of the cohort displayed NOE [27]. In 17 to 19-mo-old D2, the percentage with severe RGC loss increased to 80%. Wholemount retinas demonstrated that the pattern of degeneration in D2 started tended to start focally and then expanded to wedge-shaped regions [8-12]. This pattern of RGC loss was analogous to the pattern observed in human glaucoma [6; 7] and also implicated damage to the axons in the ONH as the site of initial injury.

Degeneration of axons occurred around 9-10 mos of age [8; 10; 12; 27]. The early signs of degeneration involved disorganization of the glial lamina, axon swellings, and the accumulation of organelles and neurofilament [12; 24]. These features were predominantly found in the glial lamina, prior to observations in other regions such as the distal optic nerve or NFL. Axon degeneration and gliosis followed with increasing disease severity.

D2: Effect of Bax-deficiency

In human glaucoma, the loss of RGCs occurs through a programmed cell death pathway, apoptosis [31; 32]. RGC death may also result from secondary degeneration independent of apoptosis [33]. Apoptosis can be initiated through extrinsic receptor-mediated signaling or intrinsic mitochondrial signaling pathways [34]. Intrinsic apoptotic initiation involves changes to the membrane permeability of mitochondria. The change in membrane permeability can permit the leakage of pro-apoptotic protein cytochrome c into the cytoplasm. Cytochrome c release is also regulated by the B-cell lymphoma (Bcl-2) family of genes. Bcl-2 genes can be pro-apoptotic or anti-apoptotic. A Bcl-2 member gene, Bcl2-associated X protein (Bax) is pro-apoptotic and can initiate the release of cytochrome c from the mitochondria independent of mitochondrial membrane permeability [35; 36].

The inhibition of Bax activity through transgenic lines carrying null alleles (D2.*Bax*$^{-/-}$ or 129 Sv/C57Bl/6J-*Bax*$^{-/-}$), anti-sense oligonucleotides, or function-blocking peptides in mice or rats was shown to protect the RGC cell body from apoptosis in multiple models including D2, optic nerve crush, and axotomy [37-40]. However, the axons were not completely protected. Instead, axon degeneration appeared to be delayed, as determined by an upward shift in age in which a significant fraction of a cohort had severe degeneration [37]. A different model that induced RGC death through glutamate toxicity did not show any effects from Bax deficiency [37; 38]. Excitotoxicity may represent a model for secondary degeneration. The RGC loss in D2 is through an intrinsic apoptotic pathway, but axon degeneration occurs through a different pathway.

D2.*Bax*$^{-/-}$ mice were also used to support the theory that the ONH is the likely site of glaucomatous injury in D2 [12]. In Wallerian degeneration, axons proximal to a focal injury do not degenerate as long as the cell body survives, but axons distal to the lesion degenerate [41]. Since RGC bodies are preserved in D2.*Bax*$^{-/-}$, optic nerves in late glaucomatous degeneration should survive to the point of the injury. Optic nerves with over 95% axon loss were selected for examination. Although there was massive loss of axons, there were surviving axons left at the anterior edge of the glial lamina. The site of injury most likely occurred at the glial lamina or very close to it.

As a complementary experiment, the Slow Wallerian degeneration (Wld^{s}) gene was crossed in the D2 strain (D2.*Wld*^{s}) [12]. *Wld*^{s} confers protection to axons after injury, but not to the cell body [42]. In D2.*Wld*^{s}, there were much less severe cases of axon degeneration in 12-mo-old mice compared to D2 [12]. The number of surviving RGCs correlated well with surviving axons, though there were some reductions in soma size that suggested that the RGCs were not healthy. This experiment showed that protecting the axons from degeneration also preserved the RGC body.

The use of the D2.*Bax*$^{-/-}$ demonstrated important concepts to understanding the biology of neurodegeneration in D2 [37; 43]. These findings may influence the research on neuroprotective strategies in human glaucoma. The first concept is that the factors leading to degeneration in the axons and in the RGC body are separable. This means that the development of therapeutic agents should be assessed for whether the agents would affect the axon or the RGC. Any injury models used should also consider whether the injury should affect the retina or optic nerve to assist in the interpretation of results. The second concept is that, as suspected in human glaucoma, the ONH sustains glaucomatous injury before damage manifests in RGCs. It cannot be excluded that the soma may have an undetected injury that results in axon damage, but degeneration appeared first in ONH, specifically in the glial lamina.

D2: Caveats

The damage to D2 RGCs and the optic nerve is consistent with the damage observed in humans. But, it is unclear whether humans express the *Gpnmb*^{R150X} or *Tyrp1*^{b} alleles. Pigmentary glaucoma is typically due to the iris rubbing against the anterior lens zonules, resulting in the liberation of iris pigments. Human glaucoma can result through different optic neuropathies and there are likely to be other genetic factors involved in the disease. Risk factors like angle closure or elevated IOP can activate pathways that are common to degeneration in both mouse and human. This makes D2 a useful model to study glaucoma, but D2 is still a mouse model. When possible, additional models should be used to validate the findings in D2.

RGC and axon degeneration is eye-independent, variable, asynchronous, and progressive in D2. There is also some susceptibility of female D2 in developing iris defects and elevated IOP. These qualities can make it difficult to detect differences in an experiment, especially if the number of mice is limited or if the phenotype is subtle. It is important to consider the requirements for a sufficient sample size, to sex-match experimental groups and controls, and to determine the range of degeneration relevant for the study.

Acute glaucoma models

Acute models of glaucoma can be useful for answering specific types of questions. Injuries can be applied to the optic nerve or retina directly and the resulting biology can be compared with what is known to occur in glaucoma. Laser photocoagulation and optic nerve crush are two alternative methods used in this thesis. These two methods, along with excitotoxicity, are briefly discussed.

Laser photocoagulation

Laser photocoagulation surgery typically utilizes an argon or diode laser to cauterize elements of the eye with the goal of reducing aqueous humor outflow. The laser can be aimed at a combination of the trabecular meshwork, episcleral veins, or limbal veins [44-52]. Outflow is stopped at the trabecular meshwork or after the aqueous humor exits Schlemm's canal to join the circulatory system.

The number of laser pulses applied, as well as the strength and duration of each pulse, can alter the effectiveness of the surgery. The pigmentation of the mouse is also a factor to consider; albino mice eyes absorb less energy than pigmented eyes and require different laser conditions [47]. IOP can increase between 4-48 hrs after surgery and stays elevated for some time before decreasing. Elevated IOP through laser surgery can lead to a sectorial pattern of degeneration similar to human glaucoma [46; 47; 49; 53]. Empirically-derived protocols need to take into account the particular types of equipment and mouse strains used, as well as the severity or time course desired, to produce consistent results [54]. A specific time course may be useful in studying therapeutic interventions.

Optic nerve crush or axotomy

Optic nerve crush and axotomy are blunt procedures that crush or sever the optic nerve. Crush surgeries typically use self-closing or cross-action forceps that can apply a constant and consistent force onto the optic nerve [55]. The duration of the injury can be modified to induce more moderate or more severe damage. Retinal ischemia can be avoided as long as the duration is not too long and the site of injury is posterior to where the central retinal artery branches from the ophthalmic artery [16].

The benefits of this technique are that it can be performed on any strain of mouse and the time that axons are damaged is known. Timing can be important in testing drugs to determine how quickly the optic nerve is expected to degenerate and whether a particular drug can slow degeneration. Direct damage results in axon degeneration, but there are axons that are initially spared which undergo secondary degeneration [56]. The study of secondary degeneration may be most useful in understanding how to preserve remaining axons in humans. Optic nerve crush and axotomy can also be used to investigate the effects of inflammation on the glia surrounding the injury site.

Excitotoxicity

It is controversial whether glutamate-induced toxicity is a primary factor in glaucomatous RGC death [33; 57; 58]. Excessive release of glutamate from axons and glia can result in calcium accumulation in astrocytes, oligodendrocytes, and NG2 cells. Calcium accumulation can cause apoptosis or necrosis to occur. In order to study how glutamate causes RGC death, glutamate, N-methyl-D-aspartate (NMDA), or kainic acid is injected intravitreally [54]. These ligands activate their cognate receptors and lead to an increase in intracellular sodium and calcium ions. Glaucoma has a distinct pattern of

RGC degeneration and the disease specifically affects RGCs. It is difficult to explain how these two features can be achieved through excitotoxicity from an invitreal injection.

More recent work has introduced the possibility of local toxicity due to ectopic glutamate release from synaptic vesicles arising within the glial lamina after IOP elevation from a laser model [59]. Axon loss after laser-induced IOP elevation was attenuated when plugs containing drugs that block glutamate receptors and voltage-gated sodium channels were placed next to the ONH after surgery. Decreasing the amount of glutamate that might enter axons appeared to be neuroprotective. Ectopic glutamate release in the ONH provides a new target for understanding the involvement of excitotoxicity in glaucoma.

Overview of astrocytes

Astrocytes are present through the CNS and have a wide variety of functions [60-69]. Astrocytes respond to early disease signals and might be informative in understanding the events that contribute to the progression of glaucoma [62; 70].

Astrocytes can be identified by their expression of certain genes and their morphology. These markers should be used with caution however, because the location and physiological state of the astrocyte may influence which marker is expressed [66; 69]. Other cell types may also express the same genes. Regardless, there are some common markers used to identify astrocytes in the CNS and ONH. These include cytoskeletal elements like GFAP, vimentin or nestin [71-73]; glutamate transporters like GLAST/EAAT1 and glial glutamate transporter GLT-1/EAAT2 [74]; and the more recently identified Aldh1L1 [75]. Other markers that have also been used to identify astrocytes but may have less specificity are glutamine synthase [76; 77] and S100-β [78; 79].

Types of astrocytes

There are two broad categories of astrocytes that were identified by morphology and localization. These are protoplasmic astrocytes found throughout unmyelinated, grey matter and there are fibrous astrocytes that are found in white matter tracts [66]. Protoplasmic astrocytes have less glial filaments than fibrous astrocytes [80]. The optic nerve contains fibrous and protoplasmic astrocytes. Both types of astrocytes express GFAP when mature, but fibrous astrocytes can be differentiated from protoplasmic astrocytes through its reactivity against the antibody A2B5 and binding of tetanus toxin [81; 82]. A2B5 and tetanus toxin both bind to gangliosides that contain sialic acid residues on the cell surface. Fibrous astrocytes make up the majority of the optic nerve and protoplasmic astrocytes are concentrated in the nerve periphery. Protoplasmic astrocytes appeared to form the glia limitans, which is a component of the blood-brain barrier [81].

The studies that characterized the protoplasmic and fibrous astrocytes were examined in transverse optic nerve sections [81; 82]. The studies showed that both astrocyte types were found in the optic nerve, but it was not clear whether there is greater segregation of astrocyte types in the pre-lamina or glial lamina, which contains unmyelinated axons, or in the MTZ, which contains a mix of unmyelinated and myelinated axons. In the brain, protoplasmic astrocytes have a regular, tiled formation [83] but the astrocytes in the glial lamina have greater overlap [15]. The astrocytes in the glial lamina appeared to have a particular orientation that may be more informative of its function [15].

Astrocyte morphology relates to function

Astrocytes were named for their radial processes that stretch out into a star-shaped appearance. The processes of each astrocyte can extend in a predominately transverse, longitudinal, or random directions in the optic nerve [15; 84]. The discrete domains within the optic nerve may provide an environment that enables astrocytes to have lesser known activities. The morphology of astrocytes within the domains may be reflective of the functions required.

Astrocytes surround axons in both the pre-laminar and laminar regions. In species with a lamina cribrosa, astrocytes line the pores and form a continuous glial sheath around each nerve bundle [85]. In mice, transversely-oriented astrocytes organize into glial columns that axons pass through, similar to the pores of the lamina cribrosa [12; 15]. The orthogonal orientation of axons to astrocyte processes and the reinforcement of multiple astrocyte processes contacting the axon bundle may provide greater structural stability to the axons and the optic nerve. The 'honeycomb' arrangement of the astrocytes was gradually lost as the axons became myelinated, suggesting that structural support from astrocytes may not be as necessary in the optic nerve as in the glial lamina.

Transverse- and randomly-oriented astrocytes might interact with other cells, as well as with the blood supply. Astrocytes can form gap functions with one another [86; 87], which allow calcium signaling through a population of connected astrocytes [63; 88]. This may allow astrocytes to rapidly respond to excitatory stimuli by increasing their uptake of neurotransmitters or to dilute the toxic effects of increased intracellular calcium. The formation of finger-like projections of astrocytes might probe the environment at the nodes of Ranvier [89], which are the gaps that enable saltatory conduction located between segments of myelin. Astrocytes would be able to monitor the activity at the node as well as remove neurotransmitters that might be released by the axon [59; 90]. Optic nerve astrocytes also form end-feet on blood vessels and the pia mater [15]. The astrocyte end-feet contribute to the integrity of the blood-brain barrier and this association allows astrocytes to transport nutrients and ions in from the vascular system, transport waste products out of the vascular system, and regulate blood blow to neurons [63; 91].

Longitudinal astrocytes, found more often in the MTZ or myelinated optic nerve [15], might be better suited to monitor the health of a bundle of axons. The astrocyte may also exchange signals from the myelin sheaths that cover the axons. Astrocytes might therefore be sensitive to injuries in axons and myelin.

Astrocytes may be oriented in any direction in the optic nerve, but appear to have some specificity in having a transverse orientation in the glial lamina. Astrocytes have multiple processes that would enable many types of interactions, which may explain how astrocytes can be involved in so many functions.

Astrocyte reactivity to optic nerve injury

In disease or injury, astrocytes become reactive by increasing the expression of different genes controlling cytoskeletal elements, changing their cellular morphology, expressing cytokines or growth factors and their receptors, and forming a glial scar at the site of injury [63; 69; 92-94]. Increase of intermediate filaments GFAP and vimentin expression is common in reactive astrocytes, especially when the astrocyte processes thicken to form a glial scar. Astrocyte can produce cytokines and neurotrophic factors and their receptors after injury [69]. This might result in pro- or anti-inflammatory molecules, depending on the context of the astrocyte [93]. The glia scar can include other glia, such as NG2-expressing cells [95], extracellular matrix proteins such as chondroitin sulfate proteoglycans [96], and myelin proteins like myelin-associated glycoprotein (MAG) [97]. These elements can physically block axons from innervating its target and prevent axon and myelin regeneration [62; 68; 94; 95; 98].

Astrocytes appear to be the primary mediators of scar formation in the brain and spinal cord after traumatic injuries or a multiple sclerosis model, experimental autoimmune encephalomyelitis (EAE) [93]. A transgenic mouse was generated to express herpes simplex virus thymidine kinase (HSV-TK) under the GFAP promoter [99; 100]. When cells expressing HSV-TK are exposed to an antiviral prodrug, in this instance a guanosine analog ganciclovir, there is a kinase cascade that results in phosphorylation of ganciclovir [101]. Once it is incorporated into DNA, new nucleotides cannot be added to the DNA strand. This model allowed the direct ablation of astrocytes after an injury [100]. Without proliferating astrocytes after injury, scar formation was disrupted. The absence of scar formation resulted in the spread of inflammation, persistence of a broken blood-brain barrier, increased damage and degeneration, and impaired recovery [93].

The reactivity of astrocytes is proposed to be a graded response, one that is reflective of the severity of the injury [93]. Astrocytes did not appear to proliferate after acute models of glaucoma [102; 103], although a scar was formed when the optic nerve was crushed [102]. Astrocyte proliferation was observed during axon degeneration in D2 mice [104]. This reflects the heterogeneity in the astrocyte response to injury and also emphasizes the importance of the context of the injury.

A less severe injury may result in short-term hypertrophy that can resolve with time [93; 103]. When IOP was transiently elevated for 1 hr through cannulation with saline, ONH astrocytes retracted their processes and the organization of the glial lamina was disrupted within 3 days [103]. The astrocyte processes became thicker and less complex, with hypertrophy of the astrocyte soma. The transient IOP elevation did not result in axonal degeneration, or apoptosis or proliferation of astrocytes. The morphology of the astrocytes appeared to be recovered by 6 weeks after IOP increase and the honeycomb appearance of the glial lamina was restored. A graded response would be beneficial to cells and tissue, especially in the case of eyes, which are subject to daily fluctuations in pressure [105]. Large fluctuations in IOP of glaucoma patients was correlated with increased vision loss, even though the long-term mean IOP was within a normal range [106]. Less severe insults would be manageable without the formation of a glial scar that could cause future impairments.

In an optic nerve crush, which causes direct damage to axons, fibrous astrocytes had a biphasic reaction where they retracted their processes within 3 days, gradually re-extended their processes after 1 week, and formed a glial scar within 2 weeks [102]. The glial tubes that make up the honeycomb appearance of the normal glial lamina were not restored; this may be due to the absence of axons. There was also lost contact between other cells, blood vessels, and the pia. Some contact with blood vessels and the pia were re-established. The reduced interaction with the circulatory system may have long-term effects on the optic nerve.

In contrast to the pronounced retraction of branching of optic nerve astrocytes after crush injury, protoplasmic astrocytes in the cortex have increased branching after a traumatic stab lesion [102], while astrocytes in D2 mice had a modest decrease [107]. Astrocytes in glaucomatous D2 had less complex ramification of their processes and the processes that remained were thickened. These differences reflect the different responses by particular types of astrocytes. Astrocytes in D2 may undergo a biphasic morphological response, but the transition may be transient [107]. Prior to axon loss, transversely-oriented astrocytes appeared to have localized remodeling by the formation of appendages that extended longitudinally into axon bundles [107]. The appendages were not formed from all the processes, suggesting that they may have reacted to early signs of axonal damage.

Overview of microglia

Microglia are the resident phagocytes of the CNS. Microglia can be identified through many of the same markers that label macrophages. This can include expression of CD68, Iba1, and Lgals3. These markers cannot distinguish resident microglia from infiltrating phagocytes. Microglia can become more amoeboid after activation [108], but this morphology might suggest also a resting microglia [109] or an invading phagocyte [110]. It can be difficult to distinguish microglia from macrophages or reactive and non-reactive microglia, so it is important to be aware of the context in which the cells examined.

Microglia have thin, ramified processes that are used to continuously monitor the local neuronal environment [111]. Disruption of the blood-brain barrier through a focal laser-mediated lesion in the brain drew a rapid and localized response of microglia to the site of injury [111]. Microglia with increased ramification appeared to enwrap the lesion in the blood vessel with processes, which had an effect of shielding the lesion from the surrounding tissue. Acute injury or neurodegenerative disease can result in Wallerian degeneration, which is when the axon degenerates away from the cell body, or axonal dieback, which is when the axon degenerates towards the cell body. The removal of the axonal fragments can be performed through the phagocytic activity of phagocytes like microglia or macrophages [112; 113]. The response of microglia to injury or disease includes participation in glial scar formation, phagocytic activity, morphological changes, proliferation, and cytokine release [98; 112; 114].

Microglia are phagocytic and induce oxidative stress

Activated microglia were found to be involved in inflammation within the substantia nigra of patients with Parkinson's disease (PD) [115]. It was hypothesized that dying neurons might release alpha synuclein (Snca) into the extracellular space, which would subsequently be phagocytosed by microglia, and then lead to chronic inflammation due to cytokine release by microglia [116]. Snca, which forms aggregates in the Lewy bodies found in PD and dementia with Lewy bodies, appeared to activate cultured microglia [116]. The internalization of Snca led to the release of reactive oxygen species (ROS) in the culture media. ROS can damage lipids, proteins, and DNA, which can result in degeneration of the cell [117; 118]. The deletion of the enzyme that generates ROS in phagocytes, NADPH oxidase [119], resulted in less ROS production and less toxicity to neurons in response to Snca internalization by microglia [116].

Microglia also cause inflammation after the secretion of cytokines in response to certain types of injuries [112; 120]. In demyelinating diseases like multiple sclerosis, lesions contained microglia, fragments of myelin, and inducible nitric oxide synthase (iNOS) [121]. Nitrogen oxygen species such as nitric oxide are produced by iNOS. The cells that produced iNOS were microglia and, infrequently, the astrocytes surrounding the lesion. Microglia that phagocytosed myelin *in vitro* also expressed iNOS [122]. These cells released TNFα, which is a pro-inflammatory cytokine, and glutamate after myelin internalization. TNFα and glutamate release could result in local inflammation and glutamate toxicity to surrounding glia and neurons. Nitric oxide reacts with superoxide to form a free radical that damages cell membranes of phagocytes and astrocytes [123]. Myelin and axons were also affected by oxidative damage [124].

Studies in the PNS have demonstrated that macrophages express Mac-1, Mac-2/Lgals3, the Fc receptor, and F4/80 during Wallerian degeneration [125]. The expression of Lgals3 appeared to be specifically expressed when macrophages were phagocytosing myelin; Lgals3 was also seen in phagocytic Schwann cells [125]. In cultured microglia, myelin was phagocytosed and each of the phagocytic markers were expressed by microglia [126]. Astrocytes co-cultured with microglia and did not demonstrate any phagocytic activity. However, in optic nerves, the expression of the phagocytic markers was highly variable after axotomy. Microglia did not appear to efficiently remove myelin in the optic nerve even though there was acute damage to the axons.

Microglia in optic neuropathy

The slow removal of myelin after injury was observed after axotomy and enucleation in rodents [126-129]. Indeed, myelin debris persisted for months in the optic nerve despite the presence of phagocytic microglia. Microglia could have early but brief periods of phagocytosis that occurs asynchronously, which might explain the variable expression in injured tissue. The phagocytosis of myelin was proposed to lead to inhibition of further phagocytic activity in microglia and macrophages [130]. This could result in an early deactivation of phagocytosis.

The involvement of cytokines and ROS in glaucoma is unclear. Inflammation is not a typical sign of POAG or PACG. Microglia from glaucomatous human optic nerves were reported to produce cytokines [131], TNFα [132; 133], and nNOS, iNOS, and eNOS [134]. However, increased iNOS was not reproduced in a different study of human optic nerves [135]. There also did not appear an increase in iNOS production in the optic nerves of two rodent models of glaucoma [135; 136]. The technical differences in tissue preparation and small sample size of human tissue may have contributed to difference in the conclusions of iNOS labeling in human tissue [135]. The animal models used may not be similar to human disease in regards to iNOS expression.

In human glaucoma [108] and in the D2 model [104; 137], microglia appeared more abundant using cell markers in the ONH. However, this may have been due to the redistribution or movement of microglia to a site of injury. Microglia were not observed to proliferate, as measured by the incorporation of a synthetic nucleoside used to label replicating deoxyribonucleic acid [138].

Unexpected behavior of glia may be driven by specific local cues

Microglia and astrocytes most likely play important roles in glaucoma, but the roles may not be identical to the roles for those cells elsewhere in the nervous system. The deficiency of myelin internalization, the uncertainty of ROS production, and the possibly non-proliferative nature of microglia in glaucomatous optic nerves suggests that optic nerve microglia have different roles in the optic nerve than they do in the brain.

Astrocytes are capable of a wide variety of functions and may perform functions similar to microglia. The different types of damage that might result in the development of glaucoma might elicit different reactions from the resident glia. This thesis will examine the novel role of phagocytosis by astrocytes in the ONH.

Chapter 2: Phagocytic astrocytes in the optic nerve head internalize gamma synuclein spheroids

Preface

Chapter 2 is based on results from the following publication:

> **Nguyen JV**, Soto I, Kim KY, Bushong EA, Oglesby E, Valiente-Soriano FJ, Yang Z, Davis CH, Bedont JL, Son JL, Wei JO, Buchman VL, Zack DJ, Vidal-Sanz M, Ellisman MH, Marsh-Armstrong N. Myelination transition zone astrocytes are constitutively phagocytic and have synuclein dependent reactivity in glaucoma. Proc Natl Acad Sci U S A. 2011 Jan 18;108(3):1176-81.

This work was a product of the collaborative effort of all co-authors, especially the efforts of Ileana Soto. Experiments were carried out under the supervision of NM-A.

Figures 2.2C, D (IS, NM-A); 2.4B (IS, NM-A); 2.7A, B (NM-A); 2.8A (K-YK, EAB) were data generated by co-authors and previously published.

Figure 2.9A (EO, FJV-S) and Figure 2.9B (CD, ZY) were performed by co-authors and analyzed by JVN.

Figures 2.1; 2.2A, B; 2.6C were experiments of published and unpublished data established by co-authors performed by JVN.

Figures 2.3; 2.4; 2.5; 2.6A, B were original data generated by JVN.

Introduction

The synucleins form a family of genes that are primarily expressed in the nervous system. The first synuclein was identified in the electric ray *Torpedo californica*. *T. californica* have a high density of cholinergic neurons in the electromotor nucleus that synapse onto the electric organ [139]. The synapses are enriched for proteins involved in synaptic transmission and neurotransmitter metabolism, which enable the ray to produce electric shocks. Cholinergic synaptic vesicles were purified from the electric organ in order to produce antisera that would be able to identify vesicle-specific proteins [140]. It was this antisera that was used to identify Synuclein (Syn), so named because of its localization to the presynaptic terminal of the electric organ and to a portion of the nuclear membrane [141]. A homolog of Syn was also found in rat brain (rtSyn) and included two splice variants [141; 142]. In the rat brain, rtSyn was concentrated in the cerebral cortex, hippocampus, and dentate gyrus, but was also expressed in other regions [142].

The synuclein family of genes has expanded to include three members that are conserved among vertebrates: alpha (Snca), beta (Sncb), and gamma (Sncg) synuclein. Further sequencing of synucleins in different animals led to the conclusion that rtSyn was an ortholog of Snca, but Syn isolated from *T. californica* was an ortholog of Sncg [141-144]. While the N-termini of the synuclein genes have high sequence similarity, the C-termini have more sequence variability. This suggests that the synucleins might have similar functions, but their specific roles are regulated by their unique C-terminus. The differences in protein localization may also affect their function. Snca has been widely studied and serves as the framework of how we approached our study of Sncg.

The discoveries that linked Snca with neuropathology were from peptide sequences and proteins identified in amyloids from the brain tissue of Alzheimer's disease patients [145; 146]. Antibodies generated against two peptide sequences, sequences which were later identified to be a tandem sequence, localized to amyloid fibrils [145]. The tandem sequence, named non-A beta component (NAC), was not a known component of the amyloids or neurofibrillary tangles that were typical of AD. A cDNA screen identified a gene sequence that contained NAC as a centrally located, hydrophobic domain. This gene was named non-A beta component of AD amyloid precursor (NACP). In an independent and later study, NAC was shown to play a role in Snca fibrillization [147]. The second independent identification of Snca in AD was through the use of an antibody that recognized hyperphosphorylated tau in neurofibrillary lesions [148]. This antibody identified two additional proteins that were of a lower molecular weight than tau [146]. One protein was matched to Ueda, et al.'s NACP sequence and the other protein was homologous to bovine phosphoneuroprotein 14. The similarity of these genes led to the grouping of the genes as a family. NACP was renamed Snca and the homolog to bovine phosphoneuroprotein 14 was named Sncb [146].

The initial characterizations that demonstrated Snca localization suggested that it would be involved in synaptic transmission [141]. Studies of Snca in *Taeniopygia guttata*, the zebra finch, also showed that the majority of Snca in the molecular layer of the cerebellum colocalized with the synaptic vesicle membrane protein synaptotagmin [149; 150]. The role of Snca in synaptic transmission was confirmed when Snca was discovered to have chaperone activity by binding to synaptobrevin-2 to promote the assembly of soluble N-ethylmaleimide-sensitive factor attachment protein receptors

(SNAREs) [151]. Snca may regulate the pools of recycled synaptic vesicles in the presynaptic cleft by preventing reclustering of recycled vesicles or affecting the trafficking of other presynaptic proteins [152-154]. Reductions in the recycling pool result in less neurotransmitter release and neuronal signaling [152], which can contribute to degeneration of the synapses [155].

The structure of Snca is natively unfolded but Snca can form oligomeric intermediates and then fibrils [156]. Snca fibrils can be found in fibrillary tangles, Lewy bodies, and insoluble inclusions in neurodegenerative diseases. The involvement of Snca in fibrils and proteinase K (PK) insoluble inclusions [157; 158] have suggested that Snca aggregation is pathogenic. However, some studies suggest that the fibrils are protective and that oligomeric intermediates pathogenic [159-162].

The final member of the synuclein family is Sncg. It was identified in a cDNA screen that sought to discover genes that were differentially expressed in breast cancer as compared with normal breast tissue [163]. Sncg overrides the spindle checkpoint in mitosis by inhibiting the kinase BubR1 [164-166]. This allows cells to exit mitosis without appropriate chromosome segregation and enables the proliferation of cancerous cells.

The role of Sncg in the nervous system is less clear. Sncg was identified in an *in silico* screen that was searching for genes that might be involved in Parkinson's disease (PD) due to its similarity to Snca or that might interact with Snca [167]. Sncg was found in various regions of the brain, but was more highly expressed in motor and sensory neurons [168]. Sncg has not yet been found in Lewy bodies or senile plaques [169]. Instead, it has been found as spheroidal inclusions in dementia with Lewy bodies- and

PD-affected hippocampus [169], neurodegeneration with brain iron accumulation, type -1-affected brain [170], and optic neuropathy-affected optic nerve [171; 172]. Sncg can localize to the synapses, cytoplasm, or axons of neurons [168]. This additional localization may be informative of the different roles Sncg might perform.

Sncg is highly expressed in the cell body and axons of retinal ganglion cells (RGCs) [10; 172]. The formation of spheroids in the optic nerve suggests that Sncg might reflect pathology in the retina and optic nerve similar to Snca in the brain. PK-resistance of Snca and Sncg is related to aggregation and fibrillization, both of which typically occurred with the overexpression of the protein [173; 174].

Overexpression of Sncg in neurons (C57Bl/6J-Thy1-mγSN) had a pathological effect on specific types of neurons. Increased Sncg expression in motor neurons was followed by loss of motor neurons, neurological and motor defects, as well as Sncg spheroids [174; 175]. Symptoms were progressively worse with age. Sncg expression was increased in the retina, but there was no degeneration of RGCs or optic nerve axons in 12-mo-old C57Bl/6J-Thy1-mγSN [175].

Deletion of Sncg in mice did not appear to affect the numbers of motor neurons, sensory neurons, or RGCs [11; 176]. Changes in Sncg expression levels have thus far been reported to be overexpressed in metastatic cancer cells [163; 177-180] and decreased in the DBA/2J (D2) mouse and a rat model of IOP elevation [10; 171]. The effects of Sncg overexpression or deletion may be subtle or there may be compensation by Snca or Sncb, and the relevant model to study it in is not clear.

I propose that Sncg spheroids form as a result of axon degeneration and not Sncg overexpression. Therefore, Sncg was used as a marker for RGCs and axons in the following experiments, and not to investigate the function of Sncg. Axon degeneration was studied in the D2 mouse glaucoma model. This is because D2 mice develop many of the same signs found in human glaucoma, including elevated IOP and loss of axons and RGCs in a distinct pattern [9; 24]. Degenerated D2 optic nerves also contained Sncg spheroids, similar to that seen in human optic neuropathy [171; 172]. Sncg spheroids appeared during a period of degeneration where sectorial loss of axons occurred and became more apparent as more axons degenerated. A novel function of optic nerve astrocytes was revealed when we discovered that astrocytes internalized Sncg and axonal spheroids.

Results

Sncg, a marker for RGCs, forms spheroids in glaucomatous optic nerve

We detected different extents of degeneration in 10-mo-old D2 retinas through *in situ* hybridization using Sncg messenger RNA (mRNA) probes and in optic nerves using immunofluorescence. For simplicity, these extents were categorized in three stages here. Retinas without signs of degeneration (No noticeable degeneration, NND) contained RGCs distributed throughout the tissue (**Figure 2.1A, left**). In sectorial degeneration, wedge-shaped regions of RGC death were observed, and in late degeneration, there were few RGCs remaining (**Figure 2.1A, center, right**).

Transverse sections of optic nerve were labeled with an antibody generated against the last 16 amino acids (aa) of the C-terminus of mouse Sncg ($\text{Sncg}^{\text{aa108-123}}$) **(Figure 2.2A)**. This antibody colocalized with an antibody for an axonal cytoskeletal marker, pNF. Both antibodies reported surviving axons in different stages of optic nerve degeneration and can be correlated with RGC degeneration [46]. With NND, axons were distributed throughout the optic nerve. In sectorial degeneration, there were regions of axon loss. In this particular example, axons were lost in a peripheral region of the optic nerve. A second region containing an intermediate density of axons was also observed. These two regions of axon loss were also visible in longitudinal sections of ONH taken from the same optic nerve **(Figure 2.2B)**. As axon loss was observed, Sncg also appeared to form spheroids. Nerves in late degeneration had little axonal labeling by pNF and Sncg, but Sncg continued to label spheroids and also labeled glia.

The glia labeled by Sncg in late degeneration were oriented transversely and longitudinally, and extended multiple fine processes from the cell body **(Figure 2.2A, B)**. This morphology was consistent with published descriptions of optic nerve astrocytes [15; 84; 89; 107]. The glia were identified as astrocytes through colocalization with Vimentin mRNA and association with blood vessels [11]**.**

The Sncg spheroids in sectorial and late degenerated nerves **(Figure 2.2B, D)** varied in size from ~1-4um. Some spheroids appeared to be continuous with axons while others were completely separated from axons **(Figure 2.2D)**. This suggested that the spheroids were axon swellings that separated from the axon. Spheroids were located inside and outside of regions with severe axonal degeneration. Sncg$^+$ astrocytes and Sncg spheroids have been reported in late stages of optic nerve degeneration in humans and a rat model of glaucoma [171], but not in optic nerves taken from eyes with retinoblastoma [172]. The formation of Sncg spheroids may only result in certain types of diseases related to optic neuropathies, but not diseases of the retina. Sncg spheroids were present in D2 as well, suggesting that the presence of Sncg labeling outside of axons may be a pathological phenotype of a disease that affects the optic nerve.

Microglia activation in D2 mice

Microglia are resident phagocytes that can be identified through Iba1 immunoreactivity [181] and appeared to be reactive in glaucomatous D2 optic nerves [182]. Microglia in 10-mo-old control DBA/2J-Gpnmb^{+}/Sj (D2-Gpnmb^{+}) ONH were oriented longitudinally with short ramified processes **(Figure 2.3A).** Microglia were hypertrophic with thickened processes in 10-mo-old D2 ONH **(Figure 2.3C)**. The change in morphology suggests that microglia may be producing an inflammatory response to degeneration [183] or that microglia may also participate in phagocytic clearance of damaged cells or axons [112].

The immunoreactivity of Iba1 was quantified and analyzed using multiple segmentation values (MSV) (Experimental Materials and Methods). With MSV, the immunoreactivity was measured at multiple fluorescence thresholds. The signal intensity from each threshold was averaged using multiple sections per optic nerve and multiple optic nerves per genotype. Two-tailed Student's t-test assuming unequal variances (Welch's correction) identified segmentation values (SV) in which there was a statistically significant difference ($p < 0.005$) in Iba1 expression in 10-mo-old D2 (N = 11; $\bar{x}$ sections quantified = 11) compared to D2-Gpnmb^{+} (N = 13; $\bar{x}$ sections quantified = 13). This method was used to identify a mean fold-change in expression that was more representative of the data.

SV with significant differences are marked by the shaded region in the graph **(Figure 2.3B)**. Iba1 expression within this range increased by a mean fold-change of 2.3

± 0.02 SEM. SV1010 was closest to the mean fold-change. At SV1010 for Iba1, D2-Gpnmb$^+$ = 9.6 ± 1 SEM and D2 = 22.3 ± 3, $p = 0.001$ in a two-tailed, unpaired t-test with Welch's correction.

Protease-resistant Sncg in the optic nerve and retina

In human diseases and mouse models of synucleinopathies, Snca is misfolded, forms fibrils, and becomes protease-resistant [157; 158]. The pre-treatment of cortical tissue containing Lewy bodies with PK diminished the reactivity of an antibody against the N-terminus of Snca, but did not diminish the reactivity of an antibody against the C-terminus [184]. This suggested that the C-terminus of Snca was PK-resistant when incorporated into fibrils. Furthermore, pre-treating tissue from samples affected with progressive supranuclear palsy, corticobasal degeneration, and Pick's disease using PK revealed immunoreactivity by the C-terminal Snca antibody that was not observed prior to PK treatment [185]. It appeared that the C-terminal Snca epitope was revealed after other proteins were proteolyzed. We compared our C-terminal Sncg antibody against a commercial Sncg antibody covering the majority of the human Sncg sequence (Sncg$^{aa21\text{-}127}$) to determine whether glaucomatous retina or optic nerve would also show selective immunoreactivity to a C-terminal Sncg antibody, with or without PK treatment.

The two Sncg antibodies were first tested for specificity in Sncg$^{-/-}$ tissue. There was no specific reactivity in the retinas or optic nerves of knockout mice, but there was reactivity in wildtype mice [11]. Then they were tested for epitope specificity. Cultured cells were transfected with a plasmid to overexpress all 123 aa of mouse Sncg or aa 1-108 (deleting the last 15 aa) of mouse Sncg **(Figure 2.4A)**. The Sncg gene was fused with GFP in order to identify cells that were transfected. Sncg$^{aa21\text{-}127}$ antibody detected all transfected cells. Sncg$^{aa108-123}$ antibody detected full-length Sncg, but not the truncated form.

After the antibodies were validated, sagittal retina sections were labeled with both Sncg antibodies **(Figure 2.4B)**. PK treatment abolished the staining of Sncg$^{aa21-127}$ and Sncg$^{aa108-123}$ antibodies in non-diseased retinas, however PK treatment selectively abolished staining by Sncg$^{aa21-127}$ in diseased retinas. Sncg$^{aa108-123}$ labeled glia in the inner plexiform layer (IPL) that was not specific to GFAP^{+} astrocytes or CD45^{+} microglia [11] in degenerated 10-mo-old D2 retinas. These findings suggest that glaucomatous damage affects the epitope exposure of Sncg. PK treatment in the ONH demonstrated similar labeling of axons, astrocytes, and spheroids by the C-terminal Sncg antibody in diseased tissue **(Figure 2.2B)**. Irregular Sncg labeling in astrocytes and spheroids in glaucomatous retinas and optic nerves were PK-resistant and selectively labeled using an antibody against the C-terminus.

Phagocytic genes expressed by astrocytes in ONH

Microglia in the ONH had increased Iba1 expression and morphological changes with degeneration. The appearance of Sncg spheroids in degeneration might induce microglial activation and also be phagocytosed by microglia to clear the material from the extracellular space. A second marker for microglia, *Lgals3*, was previously shown by our group to express in Iba1^{+} microglia in distal optic nerve during late degeneration in D2 [104]. In the ONH, Lgals3 was immunoreactive in 10-mo-old D2-Gpnmb^{+} and D2 but there was little colocalization with Iba1 signal **(Figure 2.3A, C)**. The identity of the cells that expressed Lgals3 in the optic nerve without Iba1 expression was determined through colocalization of mRNA probes *in situ* for astrocyte markers Vimentin and

Aldh1L1 [11]. Lgals3 was also expressed by GFAP-expressing astrocytes in C57Bl/6J and in GFP$^+$/GFAP$^+$ astrocytes from a transgenic mouse expressing enhanced GFP under the astrocyte promoter GLT-1 **(Figure 2.5A, B)**. Lgals3 expressed in cells that were labeled by different markers for astrocytes and in multiple mouse genotypes.

A transcriptome analysis using microarrays identified several genes involved in the phagocytosis and engulfment of apoptotic cells that were expressed by astrocytes obtained from mouse forebrain [75]. These genes, including Lrp1, Abca1, and Mfge8, were members of two evolutionarily conserved phagocytic pathways initiated by either CED-1/Lrp1 or CED-2/CrkII [186]. Lrp1 and Abca1 are part of the CED-1/Lrp1 engulfment pathway. Mfge8 is a secreted opsonin that can bridge phosphatidylserine on an apoptotic cell to engulfment receptors on a phagocyte's cell membrane [187]. We examined Lgals$^+$ astrocytes for expression of these markers involved in the phagocytic pathways by *in situ* hybridization and found that Lrp1, Abca1, and Mfge8 were indeed expressed by Lgals3$^+$ astrocytes [11]. Astrocytes in the ONH thus express genes associated with phagocytic activity and may also perform phagocytic functions.

Lgals3 expression peaks in the MTZ in the optic nerve

Lgals3 expressed in the optic nerve, but excluded the glial lamina. It was highly expressed in the adjacent myelination transition zone (MTZ), where axons become myelinated **(Figure 2.6A)**. The localization of Lgals3 expression was also examined relative to the position of oligodendrocyte marker Proteolipid protein. This showed that Lgals3 expression began where oligodendrocytes appeared most anteriorly in the nerve [11]. In late degeneration, Lgals3 reactivity was localized throughout most of the longitudinal section **(Figure 2.6C)** and did not appear to correlate with regions of axon loss **(Figure 2.4A, C)**. This variable expression was similar to observed Lgals3 expression in microglia after optic nerve transection [126]. These results suggest that Lgals3 might be reactive to stimuli other than actively degenerating axons.

Lgals3 immunoreactivity was quantified by MSV using multiple cohorts of mice. The mean fold-change ranged from 2-25 times higher in 10-mo-old D2 compared to 3-mo-old D2 [11] or age-matched D2-Gpnmb$^+$ (**Figure 2.6B**). In one quantification of Lgals3 **(Figure 2.6B, top)**, the shaded region contains values where $p < 0.01$ between D2-Gpnmb$^+$ (N = 8, $\bar{x}$ sections quantified = 7) and D2 (N = 6, $\bar{x}$ sections quantified = 4). The calculated mean fold-change was 25 ± 3 SEM. At SV400, D2-Gpnmb$^+$ = 0.7 ± 0.1 SEM and D2 = 18.2 ± 3.8, $p = 0.006$ in a two-tailed, unpaired t-test with Welch's correction.

In a second cohort of 10-mo-old mice D2, the shaded region contains values where $p < 0.005$ between D2-Gpnmb$^+$ (N = 11, $\bar{x}$ sections quantified = 11) and D2 (N = 13, $\bar{x}$ sections quantified = 13) **(Figure 2.6B, bottom)**. The calculated mean fold-change of Lgals3 was 2 ± 0.07 SEM. At SV370 for Lgals3, D2-Gpnmb$^+$ = 42.0 ± 4.8 SEM and D2 = 82.8 ± 10.1, $p = 0.002$ in a two-tailed, unpaired t-test with Welch's correction.

The variability in mean fold-change calculated here may be due to technical differences introduced during the time between each of these analyses was performed. Modifications made to image acquisition and data analysis also could affect the absolute measure of fluorescence intensity. There are also inherent differences in Lgals3 expression, especially with the knowledge that D2 within each of our cohorts have different extents of degeneration. In addition to the immunofluorescence data presented here, western blot of D2 ONH showed variable expression in ONH with degeneration

(Chapter 3 Results). Lgals3 mRNA expression was also increased in microarrays using D2 ONH [188-190]. Despite variability, Lgals3 expression was increased in a population of aged D2 mice in multiple cohorts and in different experimental approaches.

Lgals3$^+$ astrocytes phagocytose Sncg structures

Sncg spheroids were more frequently found in the MTZ, where constitutive Lgals3 expression was highest. Lgals3$^+$ astrocytes in the MTZ were therefore examined for possible interactions with Sncg spheroids. In both 3-mo-old and 9-mo-old D2 optic nerves, Sncg structures were found in close contact with Lgals3-expressing astrocytes **(Figure 2.7A)**. Some structures were also fully enclosed by the cytoplasm, as seen by confocal microscopy **(Figure 2.7B)**. Lgals3$^+$ astrocytes appeared to phagocytose Sncg in both young and old D2 mice.

Astrocytes are phagocytic in normal ONH

To determine whether astrocytes were phagocytic in other mouse strains, we examined the ultrastructure of a 9-mo-old C57Bl/6J mouse optic nerve using serial blockface scanning electron microscopy (SBEM). Astrocytes throughout the ONH showed evidence of axons and debris **(Figure 2.8)**. Granular material and vesicles were accumulated within an axon swelling and formed a protrusion into an astrocyte **(Figure 2.8, left panels)**. Debris with a similar appearance were also completely detached from axons with a membrane containing the debris **(Figure 2.8, center panels)**. It was determined that these evulsions of detached axonal material were completely enclosed within astrocyte cytoplasm after examination of serial sections. Other debris found inside astrocytes did not have a membrane separating the debris. This absence of the membrane suggested that the envelope of axon membrane containing the debris was degraded by the astrocyte **(Figure 2.8, right panels)**.

The quantification of debris in a subvolume within the glial lamina and MTZ resulted in 218 objects counted in the glial lamina and 72 objects in the MTZ [11]. The mean radius of objects within these regions was similar, averaging 1μm, but there was higher variability in the MTZ [11]. However, the glial lamina was narrower in diameter than the MTZ. This difference may influence the number of objects found per unit area and might not be reflective of the region as a whole. SBEM revealed the formation of axonal debris in a 9-mo-old C57Bl/6J ONH that did not have signs of degeneration. There may be increased axonal debris formation in the glial lamina and astrocytes within the glial lamina and MTZ internalized axonal material.

Effect of Sncg on Lgals3 reactivity after laser photocoagulation or optic nerve crush

The phagocytic activity of astrocytes in the ONH, the phagocytosis of Sncg structures by Lgals3^{+} astrocytes, and the particular localization of Sncg spheroids and Lgals3 in the MTZ led us to consider whether Sncg may be involved in the increased Lgals3 expression in diseased tissue. Translimbal laser photocoagulation is a model for glaucoma that uses a laser to cauterize the translimbal and/or episcleral blood vessels of the eye and prevent the outflow of the aqueous humor [45; 47-50; 52; 191]. This leads to elevated IOP and can result in axon degeneration and RGC loss. IOP was unilaterally increased in Sncg$^{+/-}$ (N = 11, $\bar{x}$ sections quantified = 7) and Sncg$^{-/-}$ (N = 11, $\bar{x}$ sections quantified = 4) mice. IOP increased from 15mm Hg to 30mm Hg by 24 hours after surgery in the affected eye [11]. The average IOP remained elevated in treated eyes at day 7 after surgery. Elevated IOP was not observed in untreated eyes [Sncg$^{+/-}$ (N = 7, $\bar{x}$

sections quantified = 8) and Sncg$^{-/-}$ (N = 11, $\bar{x}$ sections quantified = 6] at any time point after surgery. It did not appear that the absence of Sncg influenced IOP elevation. Although there was sustained IOP elevation in treated eyes in this cohort, there were no large regions of RGC loss [11].

Analysis of Lgals3 expression by MSV in the ONH showed that Lgals3 had a slight increase in the Sncg$^{+/-}$ lasered condition, but had a limited increase in Sncg$^{-/-}$ **(Figure 2.9A)**. There were only 2 SV that reached a significant difference by t-test when comparing lasered Sncg$^{+/-}$ and lasered Sncg$^{-/-}$. Analysis by t-tests to estimate mean fold-changes were not implemented at the time this data was published [11].

An axon injury model where the optic nerve was crushed was also used to study Lgals3 expression in Sncg$^{+/-}$ (crushed N = 6, $\bar{x}$ sections quantified = 9; uncrushed N = 6, $\bar{x}$ sections quantified = 5) and Sncg$^{-/-}$ (crushed N = 7, $\bar{x}$ sections quantified = 7; uncrushed N = 6, $\bar{x}$ sections quantified = 6) optic nerves. At the crush site, which was approximately 1-2mm posterior to the eyeball, there were amoeboid cells highly reactive for Lgals3 **(Figure 2.9B)**. The morphology and localization suggested that the amoeboid cells were microglia or infiltrated macrophages.

Because the expression of Lgals3 in astrocytes was of interest, Lgals3 expression was measured in the MTZ astrocytes anterior to the crush site. ONH was labeled with Lgals3 and GFAP^{+} antibodies. A digital mask was created based on GFAP expression. Immunofluorescence from GFAP and Lgals3 were segmented with increasing SV values, as in other MSV analyses. In this experiment, only Lgals3 expression that colocalized with the digital mask was quantified. Lgals3 expression in astrocytes was significantly increased after optic nerve crush in both genotypes **(Figure 2.9C)**. Across all segmentation values measured, $p < 0.005$ in Sncg$^{+/-}$ crushed vs. control and $p < 0.05$ in Sncg$^{-/-}$ crushed vs. control. The mean fold change for Sncg$^{+/-}$ was 2.1 ± 0.02 SEM and the mean fold-change for Sncg$^{-/-}$ was 1.7 ± 0.02 SEM.

These experiments support the idea that Lgals3 might be a general marker of reactive astrocytes after injury or degeneration. Lgals3 expression was not affected by Sncg in optic nerve crush, but it might be affected after IOP elevation. Reproducing the data from lasered Sncg$^{+/-}$ and lasered Sncg$^{-/-}$ with larger sample sizes may show that Lgals3 reactivity in hemizygous or knockout Sncg mice is dependent on the type of injury inflicted to the optic nerve. It may be that Lgals3 can report physiological changes that are specific to glaucomatous degeneration, but the effect is masked during traumatic injury.

Discussion

Sncg is a marker for RGCs, but may not be a causative factor in optic neuropathy

The expression of Sncg in RGCs has made it a useful marker for labeling RGCs. Retrograde labeling can identify RGCs by the injection of tracers directly into the superior colliculus or lateral geniculate nucleus [192]. The disadvantage of this technique is that it relies upon active transport in order to label the RGC soma. Sncg labeled RGCs and axons with similar efficiency as FluoroGold retrograde labeling [10]. It has been reproduced here that Sncg identified RGCs in mouse retinas and axons in optic nerves.

We have only shown Sncg in astrocytes by antibody labeling in optic nerve degeneration, but those astrocytes can also express Sncg mRNA after injury (unpublished observations). The cytoplasmic distribution of Sncg in astrocytes during degeneration appears to be distinct from the discrete, internalized Sncg structures by astrocytes. The widespread, cytoplasmic expression of Sncg in astrocytes was also observed in glaucomatous human, rat, and mouse tissue [11; 171]. Sncg has a role in cell proliferation [179; 193-195] and astrocyte labeling by Vimentin showed an increase in the number of astrocytes in aged D2 [104]. However, the number of astrocytes that expressed Sncg was few. The expression of Sncg in astrocytes does not appear to induce proliferation. It is unclear what role Sncg may play in astrocyte, or RGCs.

The expression of Sncg in astrocytes and the formation of Sncg spheroids occurred after degeneration. Aberrant expression of Sncg is therefore unlikely to be a causative factor in degeneration. But with the new knowledge that astrocytes can internalize Sncg spheroids, it may be possible for Sncg to have a pathological effect on phagocytic astrocytes. We have not performed an analysis to count the number of Sncg$^+$ astrocytes that exist at different stages of degeneration. If Sncg is detrimental to astrocyte health, then that may explain the few number of cells found in late degeneration.

The transfer of synucleins may have a detrimental effect on the receiving cell. Lewy bodies containing Snca were found in neuronal grafts in PD-affected patients [196-198]. Intercellular transfer of Snca was reproduced in cultured neurons, primary neurons, and in neuronal grafts in mice [199; 200]. In cultured cells, endogenous cytoplasmic Snca surrounded exogenous Snca. This suggested a possible disease mechanism where internalized Snca can seed the aggregation of endogenous, cytoplasmic Snca, in a manner that might be similar to prions [199].

Astrocytes can also internalize Snca [201]. *In vivo*, a mouse that overexpressed Snca in neurons had astrocytes with focal Snca accumulation. Interestingly, the authors noted that astrocytes containing Snca were often found alongside myelinated axons. The optic nerve is one long myelinated axon tract and the transfer of synucleins may be influenced by the integrity of the myelinated axons. The internalization of Snca resulted in the increased expression of mRNAs coding for inflammatory cytokines and autoimmune responses. The inhibition of lysosomes using bafilomycin A1 prevented the degradation of Snca and increased the expression of the cytokines TNFα and CXCL1. The internalization of Snca, and by extrapolation Sncg, may result in inflammation that causes damage to astrocytes or the surrounding tissue.

ONH astrocytes are phagocytic in the absence of disease

Sncg structures were phagocytosed by Lgals3$^+$ astrocytes in D2 [11]. EM showed that axonal debris was also phagocytosed by astrocytes throughout a naïve 9-mo-old C57Bl/6J ONH [11]. Several genes involved in phagocytic pathways were identified in postnatal mouse forebrain [75]. We have shown that the mRNA of Lrp1, Abca1, and Mfge8 were expressed in Lgals3$^+$ astrocytes in the optic nerve [11]. Astrocytes appeared capable of having an on-going phagocytic role in the optic nerve *in vivo*.

Astrocytes express genes involved in different and overlapping phagocytosis pathways that are evolutionarily conserved [75; 113]. *Megf10* (ortholog of *ced-1* in *C. elegans*) expression increased in astrocytes that phagocytosed neuronal material in the form of cell corpses [202]. *Megf10* and *Mertk* (a receptor tyrosine kinase that activates the CrkII/*ced-2* pathway) were involved in astrocytes that phagocytosed synapses [203]. Megf10 and Mertk are both receptors that activate pathways that converge onto the Rho-family GTPase Rac1 [204]. Megf10 and Mertk were shown to work in parallel pathways and it is likely that other redundant phagocytic pathways were also involved in synaptic pruning [203].

In the Glaucoma Discovery Platform database, a transcriptome derived from D2 ocular tissue, neither Megf10 nor Mertk increased in the ONH when genes were organized by morphological phenotype [188-190]. Morphological phenotypes were ranked based on severity of optic nerve degeneration, similar to the stages described in Results. When organization of gene expression was based on hierarchical clustering, Mertk expression increased significantly in the ONH during the second of three early stages of disease but decreased by the 3rd stage, and stayed comparable to D2-Gpnmb$^+$ transcript levels for the remaining disease stages. Hierarchical clustering grouped together tissue with similar gene expression and may be a more sensitive measure of the transcriptional changes that occur early in disease. Stages 1-3 were mRNA alterations that occurred before detectable nerve damage. The findings of the transcriptome still need to be validated *in situ*, but the absence of significant and continued Megf10 and Mertk expression in D2 suggests that an alternative phagocytic pathway is used by ONH astrocytes during progressive axon degeneration due to glaucomatous injury.

The Glaucoma Discovery Platform provides a rich source of material to look for new leads or to confirm suspicions of the expression of a particular gene in D2. A search for common genes involved in phagocytic pathways identified Mfge8 as one of the few genes queried that had significant increased expression by both morphological and hierarchical clustering. While morphological clustering is less sensitive at detecting early changes in glaucomatous D2 than hierarchical clustering, a consensus between both methods may make the gene easier to validate *in situ*. This is because the morphological stages reported by the database can be matched with the relative amount of axon loss in optic nerves. The stages grouped by hierarchical clustering are not easily identifiable phenotypically and can lead to uncertainty as to whether the tissue being examined is of the proper disease stage for comparison.

Lgals3 expression provides insight into a novel function of MTZ astrocytes.

Lgals3 is a galectin, which are a group of proteins that contain a carbohydrate-recognition domain and bind to β-galactosides [205]. High expression of Lgals3, coincident with macrophage markers Mac-1, FcγII/III, and F4/80, was associated with active myelin phagocytosis by microglia isolated from C56Bl/6J optic nerve [126]. *In vivo*, microglia in a transected optic nerve had high expression of Mac-1, but variable expression of FcγII/III and F4/80. Lgals3 expression was most variable. It was concluded that the absence of all four markers expressing highly in *in vivo* microglia reflected deficient activation of microglia. In a different model of injury that mimics multiple sclerosis, experimental allergic encephalomyelitis resulted in increased Lgals3 expression in phagocytes in the spinal cord and optic nerve during the phagocytosis of myelin [206; 207]. The differences in Lgals3 expression during demyelination and using two different models suggest that its expression is context-dependent.

The quantification of granular axonal material through SBEM demonstrated that debris was distributed throughout the nerve. Sncg may or may not induce Lgals3 reactivity, but if the internalization of axonal material activated Lgals3 expression then Lgals3 would be expected to express in the glial lamina. We observed little expression of Lgals3 in the glial lamina. The MTZ located between the glial lamina and fully myelinated optic nerve contained the highest relative expression of Lgals3 in each optic nerve [11]. If myelin phagocytosis is a role of Lgals3 that is conserved in astrocytes, this suggests that astrocytes in the MTZ might constitutively phagocytose myelin. This would explain the lack of Lgals3 expression in the glial lamina. An increase in phagocytic activity in the MTZ might also suggest that there is increased debris formation in that region. Further work examining the phagocytosis of myelin by astrocytes will be described in Chapter 3.

Acknowledgements

I would like to thank Masako Terada for her assistance preparing 3View datasets for analysis; Lyudmila Mamedova and Jeff Rothstein for contributing GLT-1-eGFP mice; and John McDonald for allowing access to the confocal microscope. This work was supported by a Catalyst for a Cure Grant from the Melza M. and Frank Theodore Barr Foundation through the Glaucoma Research Foundation (NM-A). Additional support was received from National Eye Institute (NEI) postdoctoral fellowship Grant 5T32 EY07143-12 (IS); Wellcome Trust Grant 075615/Z/04/z (VLB); Fundación Séneca Grant 04446/GERM/07 (MV-S); National Center for Research Resources Grant 5P41RR004050, the Human Brain Project DA016602 from NIDA and 5R01GM82949 from NIGMS (MHE); NEI Grants 5R01EY019305 and 5R21EY019737 and the Guerrieri Family Foundation (DJZ); and the International Retina Research Foundation and Lasker Foundation for 3D EM (MHE and NM-A.).

Figures

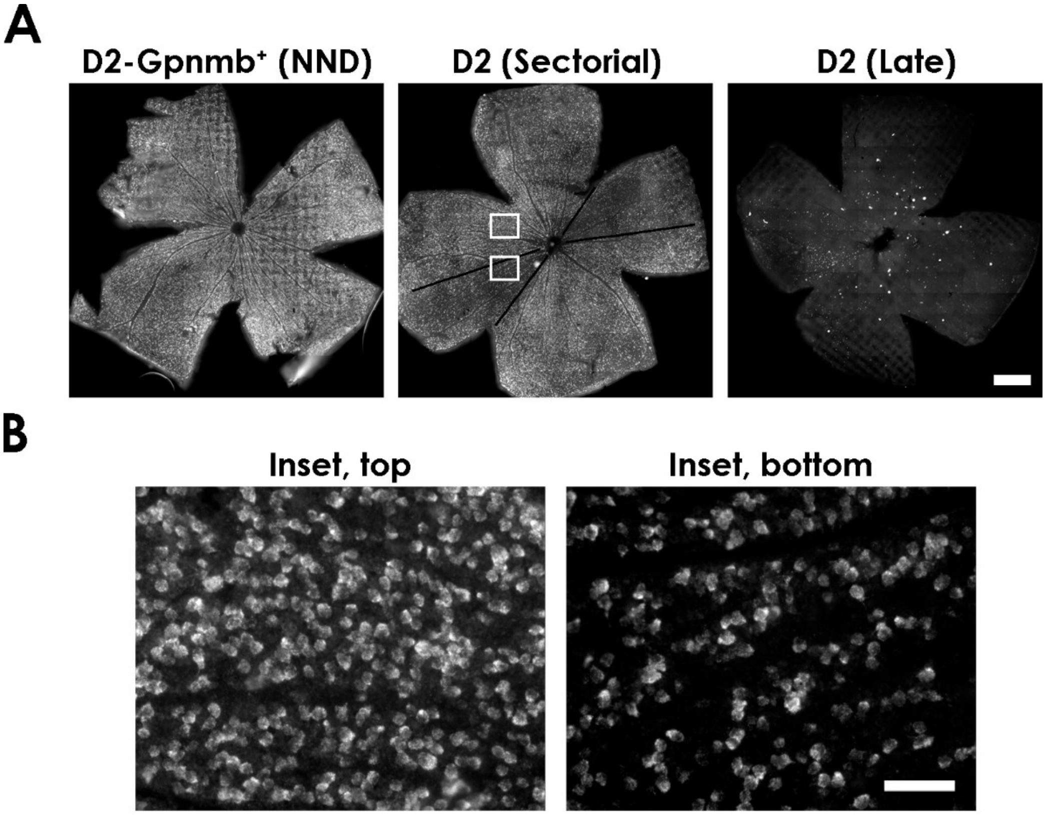

Figure 2.1. Sncg mRNA labeled RGCs in mouse retinas. A. 10-mo-old D2-Gpnmb$^+$ and age-matched D2 retinas at different stages of RGC degeneration. There was no noticeable degeneration in D2-Gpnmb$^+$. There were two sectors of RGC loss (bound by black lines) in an intermediate, sectorial stage of degeneration. Higher resolution images in white boxes shown in B. In late degeneration, few RGCs remained. **B.** Sncg mRNA labeled RGC somas. An enlarged image of a region with little to no RGC loss (Inset, top) and a region within sectorial loss (Inset, bottom) shown. (Scale bars A: 1mm; B: 70µm.)

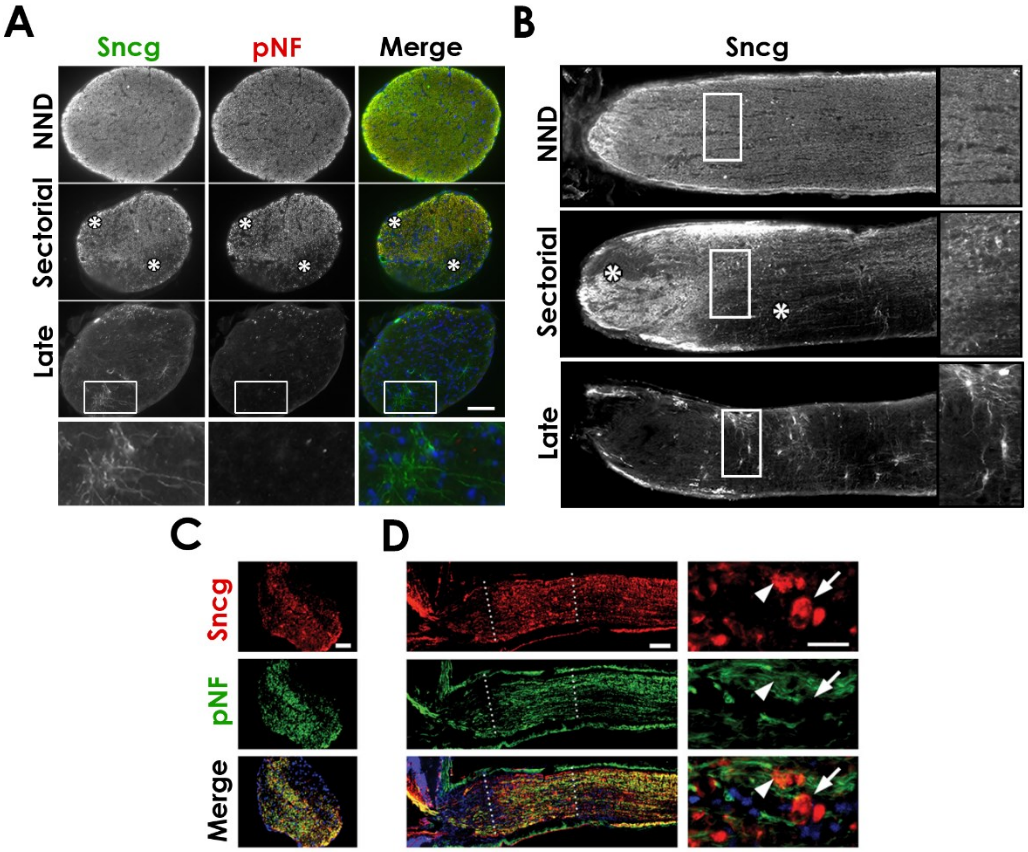

Figure 2.2. Sncg antibody labeled axons, spheroids, and astrocytes in degeneration. A. Transverse sections of 10-mo-old D2 optic nerve in different stages of axon degeneration labeled with antibodies against Sncg (green) and pNF (red). Asterisks indicate regions of axon loss. Bottom panels show enlarged image of glia (white box) labeled by Sncg but not pNF. **B.** Longitudinal ONH sections of same nerves in A, showing only Sncg labeling. Asterisks indicate regions of axon loss. Enlarged image of region within MTZ (white box) shown to the right of corresponding nerve. **C.** Transverse section of 9-mo-old D2 with sectorial degeneration seen by Sncg (red) and pNF (green). **D.** Longitudinal ONH section of same nerves from C. Some Sncg spheroids were contiguous with axons labeled by pNF (arrowhead), while others were detached from axons (arrow). (Scale bars A,B: 70µm; C: 50µm; D: 100µm left, 20µm right.)

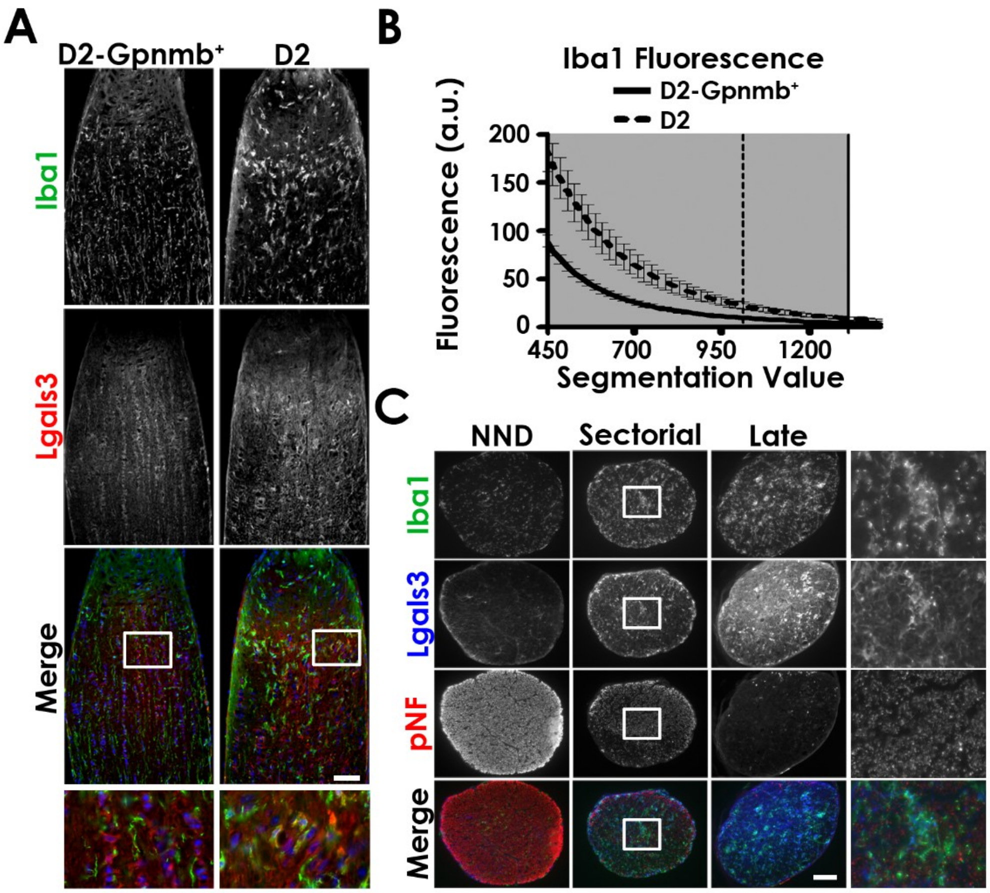

Figure 2.3. Microglial activation in 10-mo-old D2. A. 10-mo-old D2-Gpnmb$^+$ contained resident microglia labeled with Iba1 (green) and astrocytes labeled with Lgals3 (red) in the ONH. Microglia had thickened processes in age-matched D2. Enlarged image of microglia (white box) shown below. **B.** MSV quantification of Iba1 fluorescence in D2-Gpnmb$^+$ (solid line) and D2 (dashed line). Shaded region indicates fluorescence values where $p < 0.005$. SV1010 was the segmentation value closest to the mean fold-change. Errors bars show SEM. **C.** Transverse sections of D2 optic nerves in different stages of disease identified by pNF. Lgals3 and Iba1 colocalized in some cells during sectorial and late degeneration. Enlarged view of cells (arrow) shown to the right. (Scale bars A,C: 70μm.)

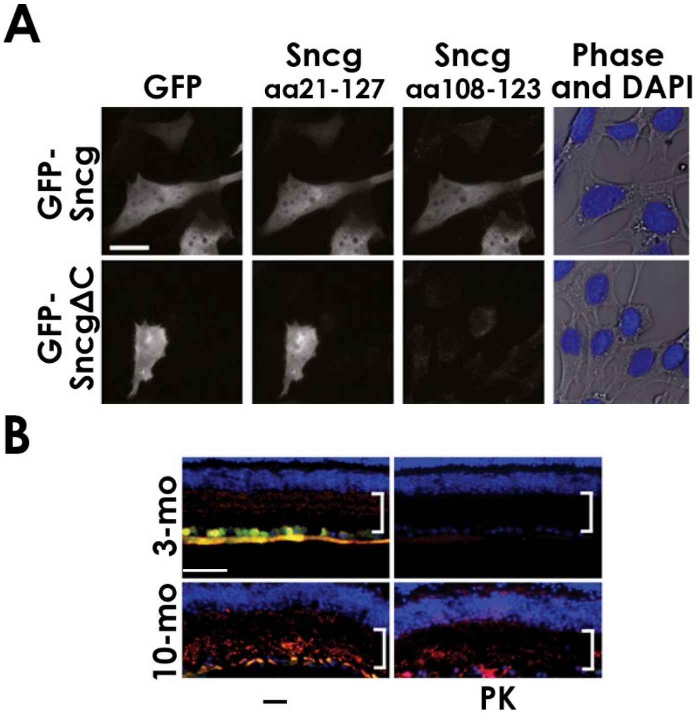

Figure 2.4. Antibody against Sncg$^{aa108-123}$ selectively labeled glia in diseased retina after PK treatment. A. 661W cells transfected with plasmids expressing GFP fused to full-length mouse Sncg (GFP-Sncg) or C-terminal truncated Sncg (GFP-SncgΔC). GFP antibody identified transfected cells. Sncg$^{aa21-127}$ and Sncg$^{aa108-123}$ antibodies labeled cells transfected with full-length Sncg, but Sncg$^{aa108-123}$ antibody did not detect truncated Sncg. **B.** Sncg$^{aa108-123}$ antibody had reactivity in diseased D2 retina after PK treatment. Sncg$^{aa21-127}$ (green) and Sncg$^{aa108-123}$ (red) antibodies both labeled RGCs and axons in the NFL in 3-mo-old D2 before PK. Degeneration in 10-mo-old retina showed absence of RGC and axon labeling, but revealed glial labeling. After PK treatment, there was no specific labeling in young retinas but the glial labeling in the IPL (brackets) by Sncg$^{aa108-123}$ remained. (Scale bars A: 20µm; B: 50µm.)

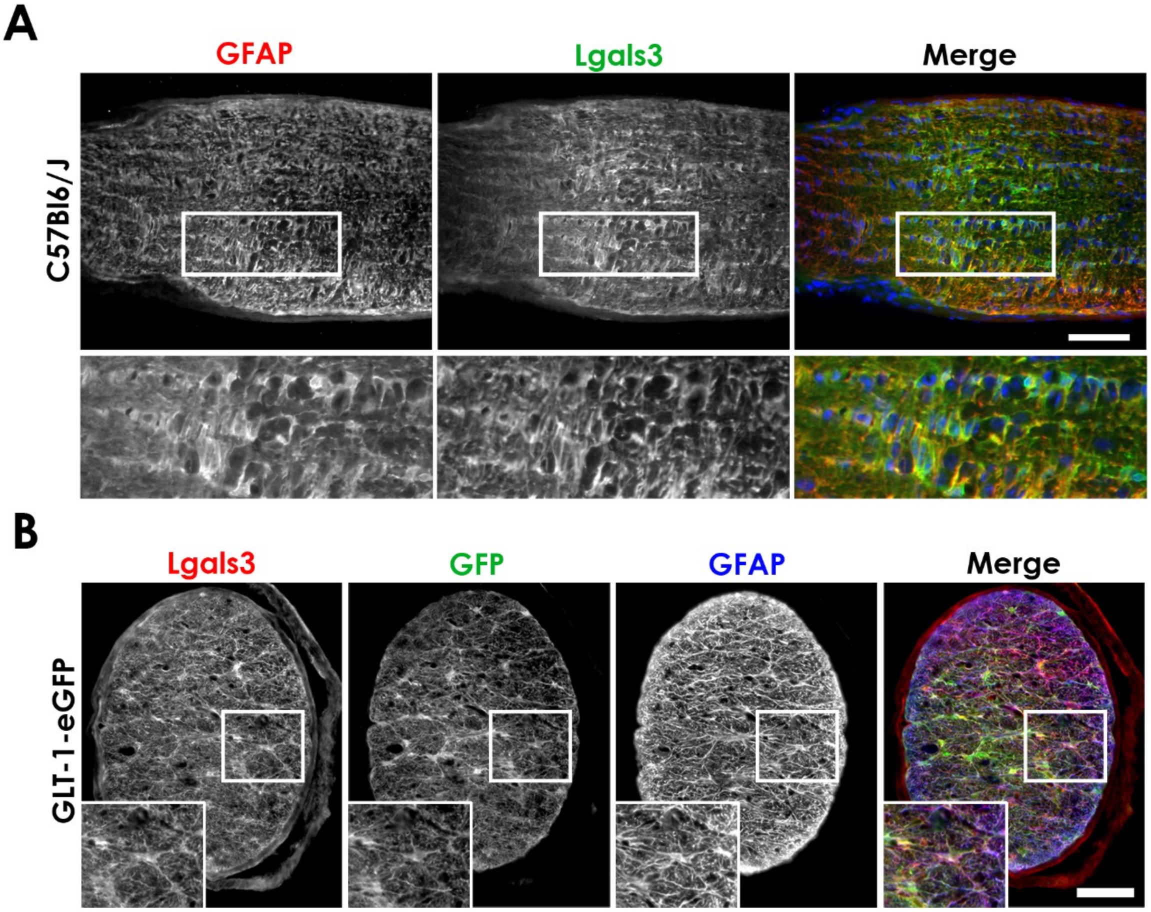

Figure 2.5. Lgals3 expressed in optic nerve astrocytes. A. Lgals3 (green) expressed in astrocytes identified by GFAP (red) in 3-wk-old C57Bl/6J ONH. **B.** Lgals3 (red) labeled astrocytes identified by GFP (green) and GFAP (blue) expression in transverse sections of 1-mo-old mice expressing GFP under the astrocyte promoter GLT1. (Scale bars A,B: 70μm.)

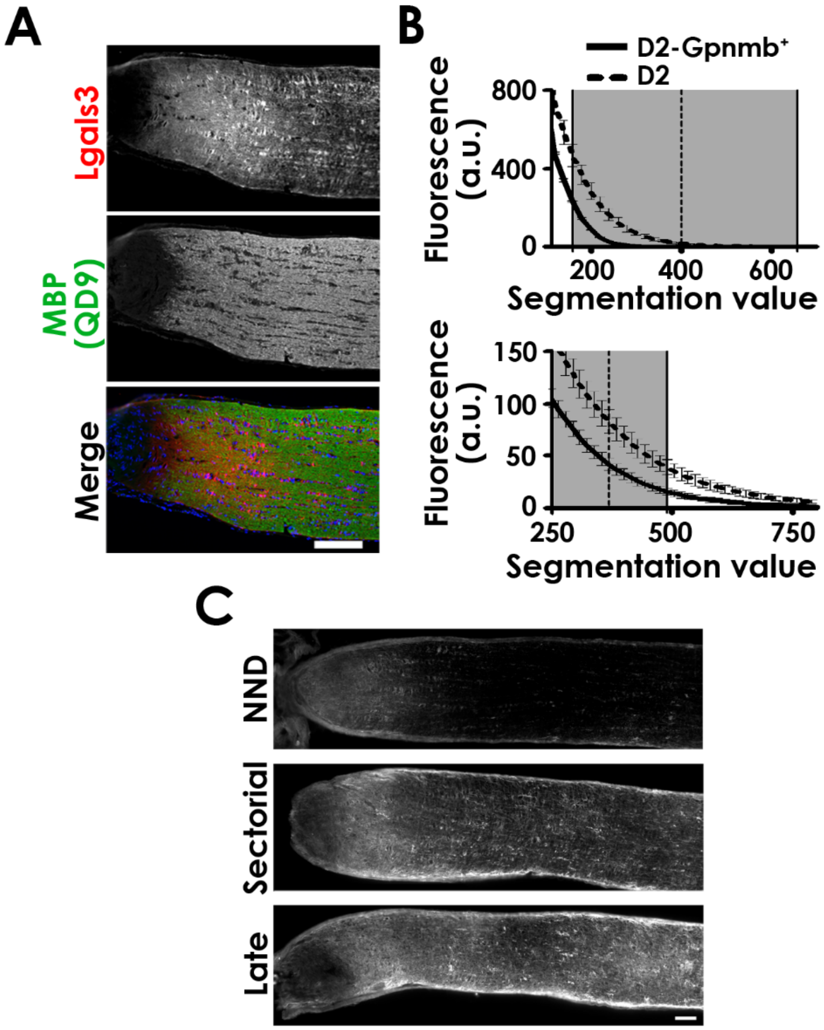

Figure 2.6. Lgals3 expression highest in MTZ within the ONH. A. The peak of Lgals3 (red) expression coincides with the onset of myelination (Myelin basic protein, green). **B.** MSV quantification of Lgals3 expression from two different cohorts of 10-mo-old D2-Gpnmb^{+} (solid line) and D2 (dashed line). Shaded region indicates fluorescence values where $p < 0.005$. SV400 (top graph) and SV370 (bottom graph) were the segmentation values closest to the mean fold-change of each experiment. Errors bars show SEM. **C.** Same ONHs as Figure 2.2.B**.** Lgals3 expression is highest at MTZ within an individual nerve. There was greater overall Lgals3 expression with axonal degeneration. (Scale bars A,C: 70μm.)

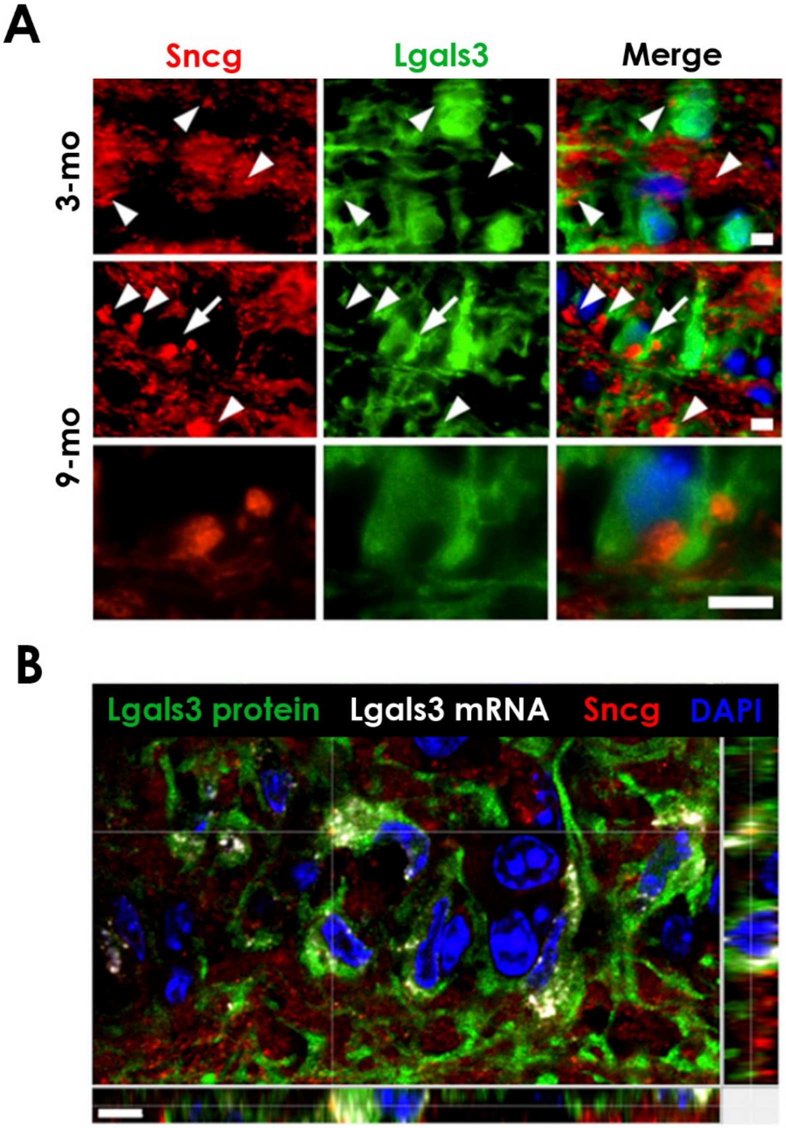

Figure 2.7. Sncg structures were close to and within Lgals3$^+$ astrocytes in mouse glaucoma models. A, B. Confocal microscopy of MTZ astrocytes labeled with Lgals3. **A.** Arrowheads indicate Sncg structures found in young and old D2. Cell labeled by arrow shown in bottom row of images. **B.** Sncg structures were internalized within 1 day of IOP elevation by translimbal laser photocoagulation. MTZ astrocytes express both Lgals3 mRNA (white) and protein (green). Sncg labeled structures (red) were completely surrounded by Lgals3 protein in the cytoplasm. (Scale bars A,B: 5µm.)

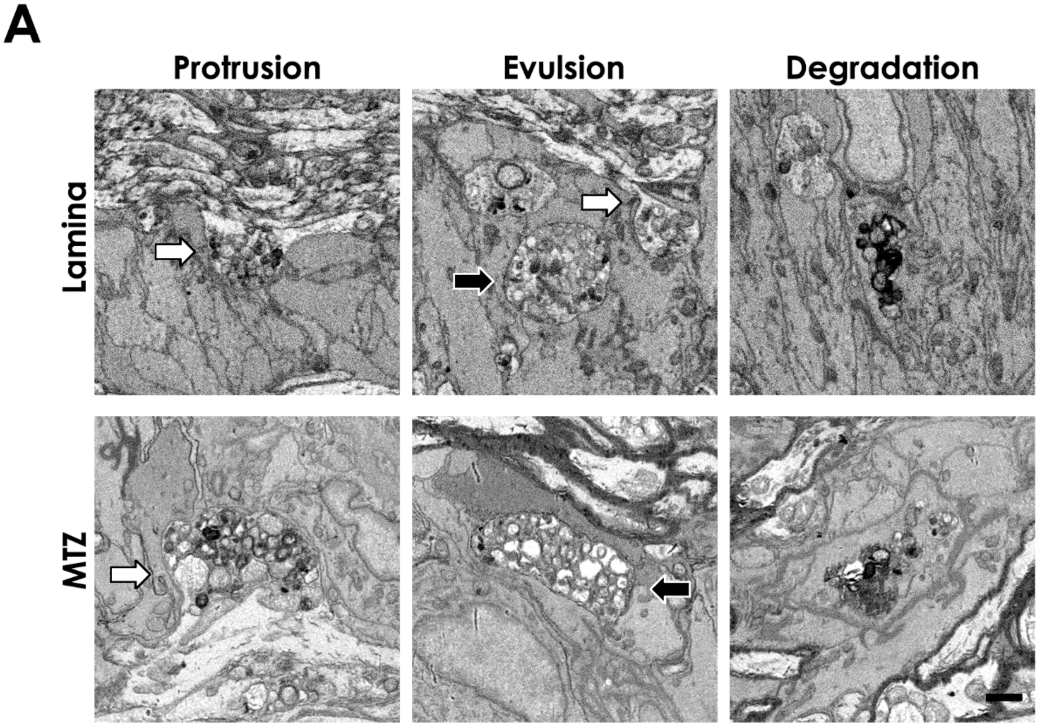

Figure 2.8. Axon debris found in the ONH in the absence of degeneration. A. SBEM of 9-mo-old C57Bl/6J ONH showed granular accumulations in protrusions (white arrows) that were still attached to an axon (left) in the glial lamina and MTZ. Evulsions were debris with a similar appearance to protrusions but disconnected from an axon (center, black arrows). Evulsions were contained by a membrane after being internalized by an astrocyte. Loss of the evulsion membrane and presence of granular material in the astrocyte cytoplasm suggested degradation of the evulsion membrane (right). (Scale bar A: 1μm.)

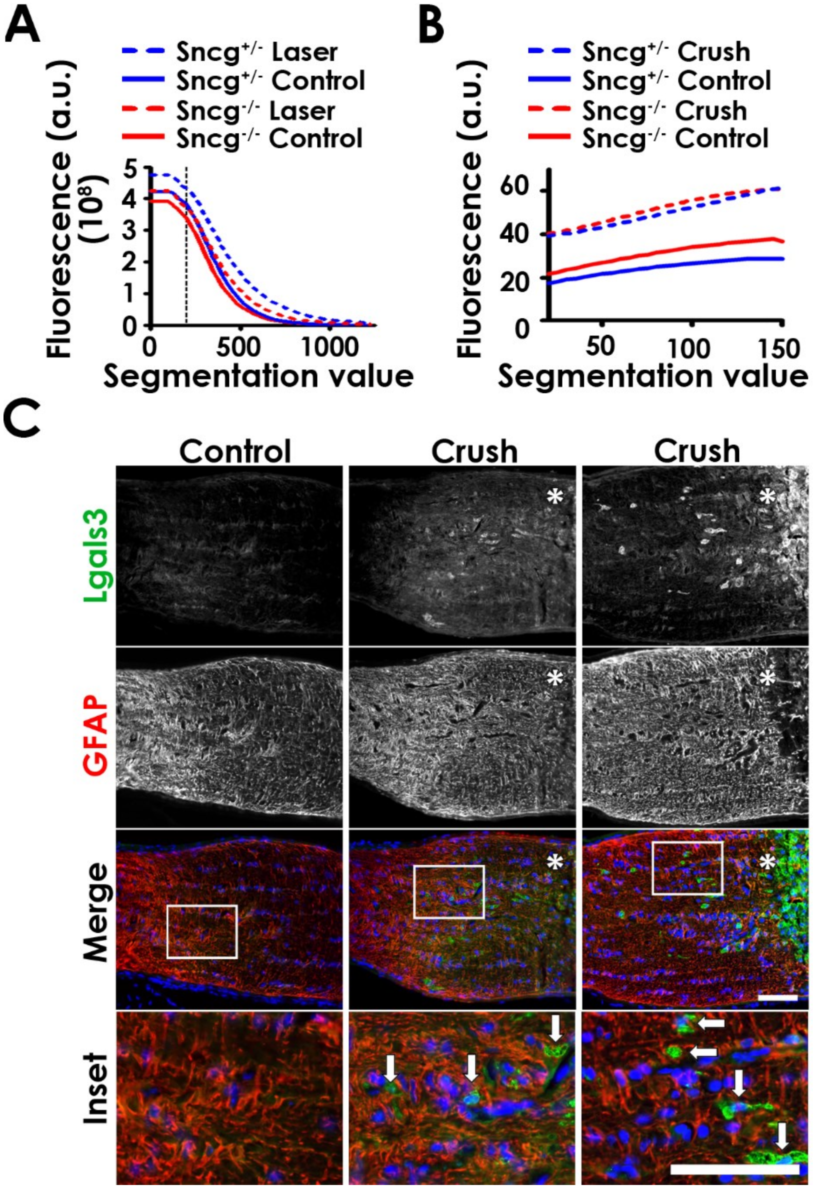

Figure 2.9. Lgals3 expression in Sncg$^{+/-}$ or Sncg$^{-/-}$ mouse ONH after injury models. **A.** MSV quantification showed an increase of Lgals3 in Sncg$^{+/-}$ 7 days after IOP elevation. **B.** Lgals3 increased in GFAP^{+} astrocytes by approximately 2-fold in all segmentation values after optic nerve crush. **C.** Lgals3 (green) and GFAP (red) expression in ONH after optic nerve crush in Sncg$^{+/-}$. Asterisk is anterior to crush site. Enlarged image of amoeboid cells (white box) found near the crush site were GFAP^{-} and Lgals3^{+} (arrows) shown below. (Scale bars C: 70μm.)

Chapter 3: The continued phagocytosis of myelin by astrocytes leads to the formation of lipid droplets

Preface

Chapter 3 contains data regarding the internalization of myelin by astrocytes and the subsequent formation of lipid droplets in astrocytes (manuscript in progress).

Figures 3.2 and 3.3A, B were performed by Keun-young Kim and Eric Bushong.

Figure 3.2D tracing and 3D modeling were generated by Akshay Murthy.

Figure 3.5A was performed by Chung-ha Davis.

All other work was original data generated by JVN under the supervision of Nicholas Marsh-Armstrong.

Introduction

Myelination is important for the rapid conduction of action potentials along the length of an axon. The loss of myelin integrity can result in motor impairments, loss of sensation, and vision loss in demyelinating diseases such as multiple sclerosis. There are many factors involved in maintaining the integrity of action potential transmittance and the stability of the myelin sheaths.

Ion channels, namely sodium channels in the nodes of Ranvier and potassium channels in the juxtaparanode, are important for depolarization and repolarization of the axon membrane potential. In the rat optic nerve, the sodium channel subunit $Na_v1.2$ was expressed on axons during developmental myelination and $Na_v1.6$ was concentrated at the nodes of Ranvier in the myelinated nerve [208]. In a mouse model of experimental allergic encephalomyelitis (EAE), there was a shift in the type of sodium channel expressed, as well as a disruption in the expression of the axonal paranode protein Caspr in optic nerves [209]. $Na_v1.2$ was expressed in the majority of Caspr-labeled nodes instead of $Na_v1.6$. While Caspr and the sodium channels generally localized to the paranode and node properly, expression was diffuse and less sharply defined than in control tissue. The demyelination caused by EAE can affect the neuron by allowing diffuse localization of sodium channels at the nodes of Ranvier which may impair saltatory conduction.

Sodium channels have been proposed as a molecular target in neurodegenerative diseases because of their influence on axon health as well as nerve function [210-213]. Axon degeneration can occur independently of defects in myelination when the dysfunction of sodium channels causes a reversal in the activity of the sodium/calcium exchanger [214-216]. Excess calcium that flows into the neuron causes excitotoxicity and blocking calcium channels can be therapeutic [217]. The utilization of sodium channel blockers is under examination for the treatment of multiple sclerosis [218-220].

The paranodal region of myelinated axons are also of interest in the study of neurodegeneration. Myelin-associated glycoprotein (MAG) is a sialoadhesin protein [221] that is expressed in the periaxonal space and enriched in the paranodal loops of myelin that make contact with an axon at the boundaries of the nodes of Ranvier [222; 223]. MAG can inhibit neurite outgrowth through interactions with gangliosides on axonal membranes [224] and this is proposed to be a factor that inhibits axon regeneration in the central nervous system (CNS) after injury [225; 226]. Defects in MAG or ganglioside expression can destabilize the paranodes, and the loss of both MAG and a key enzyme in glycosphingolipid synthesis, UDP-galactose ceramide galactosyltransferase, led to accelerated breakdown of axo-glial interactions [227-230]. The regions that surround the nodes of Ranvier can impact the health of the axon and myelin.

Multiple astrocyte processes can make direct contact with axons at nodes [89] to influence neuronal health and function. Astrocytes remove ions like potassium [231] or excitatory neurotransmitters like glutamate [90; 232; 233] from the synapse. Axons in the optic nerve were observed to release glutamate as well [234], in the form of ectopic vesicles after laser-induced intraocular pressure (IOP) elevation [59]. Astrocytes also influence the formation of functional synapses through the secretion of cholesterol [235-237].

The myelination transition zone (MTZ) of the ONH was shown to be a region containing a distinct population of astrocytes that express Lgals3 [11]. The onset of myelination results in the presence of heminodes, which are only found at regions where myelination would begin or end. Astrocytes expressing Lgals3 may therefore be reactive against something specific to heminodes. Axons in the glial lamina express $Na_v1.2$ [208], even in adults, and the differences in sodium channel distribution or node biology as the optic nerve transitions from unmyelinated to myelinated might affect Lgals3 reactivity. I propose that the myelin at the MTZ is inherently unstable due to factors that regulate myelination onset and because of this instability, the MTZ is more likely to form myelin debris. Phagocytic astrocytes can remove extraneous myelin without activating inflammatory pathways that might lead to macrophage infiltration and would explain the presence of Lgals3-expressing astrocytes at the MTZ. The work described in this chapter has led to the identification of structural and molecular evidence that astrocytes do indeed perform such a function as clearing myelin.

Results

Myelin alterations in the D2 optic nerve

The MTZ is the focus of our *in vivo* studies due to the identification of a subpopulation of astrocytes that express *Lgals3* [11]. Myelin in the MTZ was examined immunohistochemically for structural features that might suggest instability of myelin sheaths. The QD-9 Myelin Basic Protein (MBP) antibody (hereafter referred to as QD-9) recognizes the conserved epitope QDENPVV and is found at positions amino acids (aa) 108-114 in isoform 1 and isoform 2; aa 82-88 in isoform 3 and 4; aa 215-221 in Golli-

MBP isoform 1; and is absent in Golli-MBP isoform 2. QD-9 had specific reactivity in Multiple Systems Atrophy brain samples, but little reactivity in normal brain [238; 239]. This antibody was also more sensitive than Luxol fast blue staining at reporting myelin damage in a rat ischemic model [240]. The QD-9 epitope may be a significant factor in the autoimmune response in multiple sclerosis [241; 242]. QD-9 may indicate disruptions in the myelin sheath that lead to exposure of the epitope on MBP.

The ONH from a control 3-mo-old Balb/C mouse ONH was labeled with QD-9 and an MBP antibody not known to have any preference for intact or degenerating myelin. There was only weak staining of QD-9 (data not shown). However, there was colocalization of both antibodies in 10-mo-old DBA/2J (D2), a mouse glaucoma model, and DBA/2J-Gpnmb^{+}/Sj (D2-Gpnmb^{+}) ONH, the control strain for D2 (data not shown). It was not tested whether QD-9 would label myelin in other strains of mice that were 10-mos-old or if 3-mo-old D2 would have QD-9 reactivity. There appeared to be specificity towards myelin sheaths because QD-9 labeling always excluded axons within the glial lamina.

The ONHs of 10-mo-old D2 and D2-Gpnmb^{+} ONH were examined with QD-9. The brightest QD-9 signal in D2 came from small objects between myelinated axons (**Figure 3.1A**). These QD-9 reactive objects were found primarily in the MTZ of both genotypes and appeared to be punctate as well as projecting in a direction different from the long axis of the myelin sheaths. The QD-9 puncta and projections were more abundant and more strongly labeled in D2. The fluorescence intensity of QD-9 was quantified using multiple segmentation values (MSV) to estimate fold-change in D2. MSV provide measures of signal intensity across multiple fluorescence thresholds. The

D2 fluorescence intensities differed from the D2-Gpnmb$^+$ values at a significance level of $p \leq 0.005$ (two-tailed, unpaired t-test with Welch's correction) over a range of segmentation values (SV) (**Figure 3.1B**). The mean fold-change was 2.2 (SEM 1.1). SV450 was closest to the mean fold-change and had values of $\bar{x} = 23.4$ (SEM 3.1) in D2-Gpnmb$^+$ mice (N = 8, $\bar{x}$ sections quantified = 5) and $\bar{x} = 53.2$ (SEM 4.6) in D2 mice (N = 6, $\bar{x}$ sections quantified = 5). The quantified increase in fluorescence intensity of QD-9 was consistent with the observation of increased fluorescence, but is paradoxical in light of the known loss of both axons and downregulation of oligodendrocyte markers that occur in this animal model [104]. Therefore, an alternate method of quantifying myelin was used. Individual 3mm long segments of ONH from 12-mo-old D2-Gpnmb$^+$ and D2 mice were analyzed by western blot. There was half as much protein detected using MBP antibody in D2 than in D2-Gpnmb$^+$ (D2-Gpnmb$^+$ $\bar{x} = 0.6$, SEM 0.1, N = 5; D2 $\bar{x} = 1.2$, SEM 0.1, N = 9) (**Figure 3.1C, D**).

D2 are known to have asynchronous disease development with RGC degeneration occurring focally before spreading in a sectorial fashion, followed by widespread loss [9; 10; 12; 24; 27]. The severity of disease was examined for each of the D2 cohorts to determine whether a difference in disease severity might account for the increase of QD-9 immunoreactivity and decrease of MBP protein by western blot. The degree of degeneration was determined by axon labeling of transverse sections. Nerves without axon loss had axons that were evenly distributed and of a dense concentration. These were scored as no noticeable degeneration (NND). Regional loss of axons up to 60% were scored as sectorial. The loss of more than 60% of axons was scored as degenerated. The D2 cohort used for immunofluorescence contained 1 nerve with NND, 5 nerves with sectorial degeneration, and 1 nerve that was degenerated. The D2 cohort used for western blot contained 1 nerve with NND, 1 nerve with sectorial degeneration, and 7 nerves that were degenerated. All D2-Gpnmb$^+$ had NND. Because the cohorts were mismatched in terms of disease severity, it is unclear whether increased QD-9 antigenicity accompanied loss of MBP. The QD-9 reactivity may be reporting myelin undergoing degeneration with the QD-9 epitope exposed or nascent myelin sheaths that were not fully compacted and thus had the QD-9 epitope exposed.

Myelin debris in the MTZ by SBEM

The bright puncta labeled by QD-9 were found in both D2 and D2-Gpnmb$^+$, indicating that the cause for this reactivity occurred in non-diseased and diseased conditions. The appearance of the QD-9 puncta and protrusions indicated that the myelin sheaths may have irregular morphology. A non-degenerated C57BL/6J ONH that was a previously reported [11] was re-examined for myelin irregularities. The most osmiophilic material in the optic nerve is typically myelin, due to the abundance of lipids within the membranes. Normal myelin sheaths are compact, and the concentric sheaths are often visible by the appearance of major dense lines and intraperiod lines. Myelinating sheaths are found tightly surrounding electron-lucent axons. Other structures visible by electron microscopy include organelles and vesicles that are present within the axons or in the surrounding glia. In these micrographs obtained from serial block-face scanning electron microscopy (SBEM), there were multiple myelin bodies found.

The myelin irregularities observed in the C57Bl/6J ONH included a large granular structure within a glial cell that contained components that appeared similar to detached myelin (**Figure 3.2A**). These detached myelin figures had concentric rings of osmiophilic material. A second irregularity was a myelinated axon that folded back upon itself (**Figure 3.2B**). An oblique cutting plane resulted in the appearance of two separate axons. A third irregular myelin structure was a myelin protrusion detached from an otherwise intact myelin segment (**Figure 3.2C**). The myelin protrusion was traced through serial sections and found to stretch over a distance of 6 μm. There was little axonal cytoplasm in this myelin structure as it terminated inside a glial process. A three-dimensional (3D) reconstruction of this myelin sheath, as well as other nearby myelin sheaths, revealed multiple myelin protrusions from three different myelin segments (**Figure 3.2D**). Two long protrusions were inside of the same glial process. This cell was provisionally identified as an astrocyte through the radial arrangement of its processes and contact with a blood vessel. There were many myelin irregularities found in a 9-mo-old C57Bl/6J ONH and some of those irregularities were closely associated with astrocytes.

Based on the similarity of size and localization within the MTZ, it seemed that the bright puncta and protrusions detected by QD-9 in the MTZ represented some combination of the large irregular myelin bodies that were completely detached from axons and the thin, long myelin protrusions that were continuous with existing myelin segments. The combination of immunofluorescence, western blotting, and SBEM data suggests that myelin debris forms in naïve ONH and that astrocytes in the MTZ actively internalize and degrade myelin.

Electron-dense spherical structures are likely lipid droplets in the D2 ONH

Because D2 optic nerves were shown to have increased QD-9 puncta and protrusions and overall decreased myelination, D2 optic nerves were expected to show increased signs of myelin instability. SBEM data was then collected from 9-mo-old

ONHs of D2-Gpnmb$^+$, D2 without obvious signs of axon loss (mild), and D2 with severe degeneration (severe). Subvolumes selected from regions of the glial lamina and MTZ were extracted and examined for signs of myelin irregularities. As previously seen in C57Bl/6J [11], there were granule accumulations and osmiophilic structures throughout each ONH (**Figure 3.3A**). The absence of identifiable markings, such as the cristae of mitochondria or period lines of myelin, suggested that many osmiophilic structures were membranous debris. Compact myelin was also observed as a myelin body that did not contain an axon within the sheath. The myelin irregularities identified in D2 and D2-Gpnmb$^+$ were consistent with what was observed in C57Bl/6 ONH.

The MTZ of D2 (mild) nerve had a unique feature not seen in D2-Gpnmb$^+$ or D2 (severe). There were gradients of electron density throughout the volume of data that corresponded to glial processes but did not spread to the cell body. These cells appeared unremarkable in other aspects of cell morphology. The significance of these electron-dense processes is undetermined.

Numerous electron-dense spherical objects were also present in the nerves, most visibly in the mildly diseased D2 MTZ. These spherical objects varied in size from approximately 10nm to 15μm in diameter and were located primarily within glial cell bodies. These structures had high electron density around its perimeter, which allowed the use of minimum intensity projections to display their distribution and frequency (**Figure 3.3B**). An automated quantification of these spherical objects (Experimental Materials and Methods) revealed that the mildly diseased D2 indeed contained more objects in the MTZ than in the lamina (**Figure 3.3C**). The volumes of the objects were similar across all subvolumes and the only statistically significant comparison was between the MTZ of D2-Gpnmb$^+$ and MTZ of D2 (mild) (1-way ANOVA with Tukey's comparison, $p < 0.05$) (**Figure 3.3D**). The largest objects were found in D2 (mild) MTZ.

The regular, spherical morphology of the electron-dense structures suggested that they might be lysosomes, peroxisomes, or lipid droplets. Preliminary studies examined the lysosomal proteins cathepsin K, cathepsin D, LAMP1, and LAMP2 by immunofluorescence in D2 ONH to look for specific expression in the MTZ. There was little labeling of the cathepsins and some labeling by LAMPs (data not shown). LAMP1 was found throughout the ONH. LAMP2 appeared to have a slight specificity for the MTZ compared to the glial lamina or distally in the nerve, but did not appear to be specific to a particular cell type. Peroxisomal proteins were also examined (data not shown). Antibodies against PMP70 and Pex14 were screened in D2 ONH and showed no specific reactivity, and catalase appeared diffuse and punctate throughout the ONH (data not shown).

Lipid droplets form after traumatic injury in microglia and macrophages, and were infrequently observed in astrocytes of the rat optic nerve [243]. Lipid droplets store excess lipids, and these may be derived from the membranes of axons and myelin. Early in neurodegeneration, there may be increasing amounts of myelin debris that is phagocytosed by astrocytes without macrophage infiltration. Increasing amounts of myelin internalization may explain the abundance of putative lipid droplets quantified in the MTZs of ONHs.

Cultured astrocytes phagocytose myelin

We next set out to establish a model system to study the phagocytosis of myelin by astrocytes and address the formation of lipid droplets as a result of myelin internalization. A model system was formed by isolating primary astrocytes from mouse cerebral cortex and feeding the cells myelin extracted from bovine optic nerves. An MBP antibody was applied to fixed cells before membrane permeabilization in order to identify myelin that was not internalized. MBP antibody was applied again after treatment with detergent and labeled with a different fluorescent secondary antibody to label the remaining myelin. MBP antibody detected large and small myelin structures, some of which were only labeled after membrane permeabilization (**Figure 3.4A**). MBP was localized to astrocytes that expressed GFAP and Lgals3 (data not shown), but Lgals3 expression was not predictive of MBP internalization. Astrocytes expressed varying intensities of GFAP, and not all cells that expressed GFAP also expressed Lgals3 (data not shown).

Astrocytes were exposed to myelin for 1 hour (hr) to determine whether astrocytes could degrade acute loads of myelin. Samples of astrocytes were collected before myelin addition, at wash out (1 hr post feed, p.f.), and at 24 hrs p.f. By 24 hrs, internalized myelin signal decreased by approximately 68% and external myelin was not detected (**Figure 3.4B**). These results suggested that astrocytes were able to internalize and degrade myelin.

The time of myelin exposure to astrocytes was increased to 24 hrs to determine whether extended myelin internalization would have an effect on degradation. Under these conditions, the amount of myelin within astrocytes remained constant even after 2 days with no additional myelin feeding (**Figure 3.4C**). MBP outside the cells was significantly decreased, suggesting some degradation occurred. To see whether other myelin markers would report the same results, we repeated the experiments and analyzed a second myelin marker, Galactocerebroside (GalC). The findings with GalC were similar to those with MBP. Astrocytes internalized myelin, but were unable to efficiently degrade it. The prolonged period of myelin internalization may have saturated the mechanisms used to internalize and degrade myelin.

Surprisingly, the amount of GalC outside the cell decreased more slowly over the course of 2 days than MBP. The amount of GalC outside of astrocytes by the 3rd day was 49% of what it had at the end of the feeding period. This was in contrast to MBP, which had 15% left at Day 3. Astrocytes might be able to internalize proteins like MBP more effectively than complex lipids like GalC or there may be extracellular proteases, but not lipases, that were secreted by astrocytes. These factors might explain the preferential reduction of MBP signal.

The internalization of myelin may have had a toxic effect on the astrocytes. To examine astrocyte viability, 3-(4,5-Dimethylthiazol-2-yl)-2,5-Diphenyltetrazolium Bromide (MTT) assay was performed. Three different concentrations of myelin feeding (0.5X, 1X, and 2X proportional amounts of myelin used in immunofluorescence) were fed to astrocytes for 24 hours and time points were taken over the next 5 days. There was no effect on astrocyte viability as determined by the reduction MTT (data not shown).

Cultured astrocytes repeatedly fed myelin develop lipid droplets

After cultured astrocytes were determined to be able to internalize and degrade myelin, we tested whether cultured astrocytes would develop lipid droplets similar to those observed by SBEM in early glaucomatous degeneration. Transmission electron microscopy (TEM) revealed electron-dense, irregularly-shaped structures, presumably myelin debris, inside cultured astrocytes after 24 hrs of myelin feeding (**Figure 3.5A**).

Oleic acid is known to induce lipid droplet formation in various cell types, though this has not been studied in astrocytes specifically [244; 245]. Cultured astrocytes were incubated in 300μM oleic acid for 3 days. This regimen induced the formation of large spherical structures with electron-lucent cores and an irregular electron-density around its perimeter. There were also small spherical, irregularly-dense objects. The abundance of large lipid droplets after oleic acid exposure suggested that these are more comparable to prototypical lipid droplets, while the smaller lipid droplets may represent a nascent or intermediate lipid droplet form.

There were few lipid droplet-like structures in astrocytes fed myelin for 1 day, so an additional regimen of continuous and repeated myelin feeding was developed. Myelin was fed once a day for 3 days, with fresh myelin replacing old myelin. Astrocytes under these conditions formed the larger spherical structures with electron-lucent cores and the smaller spherical, electron-dense structures that were also seen after oleic acid incubation. These results of these experiments demonstrate that repeated and prolonged myelin exposure can lead to the formation of lipid droplets in cultured astrocytes.

ORO and Plin2 label lipid droplets in myelin-fed astrocytes

To quantify the lipid droplet response by astrocytes after myelin feeding, cultured astrocytes were labeled with Oil Red O (ORO). ORO is a lipophilic dye commonly used to label neutral lipids such as triacylglycerols and cholesteryl esters [246]. These lipids constitute the hydrophobic core of lipid droplets. The intrinsic red fluorescence of ORO was quantified in astrocytes that were continuously and repeatedly fed myelin once a day for 3 days. This regimen of myelin feeding produced an increase in ORO staining, which was comparable to the amount induced when cells were incubated with 100µM oleic acid (**Figure 3.6A**).

Myelin-fed astrocytes were also examined for the expression of a lipid droplet protein to further validate the appearance of lipid droplets after myelin feeding. Plin2 associates with the membranes of lipid droplets and is expressed in more diverse cell types than other proteins in the perilipin family [247; 248]. Plin2 is rapidly degraded in the absence of lipid droplets [249] and therefore may be a reliable marker for lipid droplet presence. In cultured astrocytes, Plin2 immunofluorescence was near background levels of fluorescence (personal observations). Myelin-fed and 100µM oleic acid-fed cells both showed comparable induction of ring-shaped Plin2 structures at the end of the 3 day feeding schedule (**Figure 3.6B**).

With Plin2 as a protein reporter for lipid droplet formation in cultured astrocytes, western blotting was used to re-examine the conditions of myelin feeding that could lead to lipid droplet formation. The first condition considered was whether there was a dose-dependent increase in Plin2 with myelin feeding. Similar to the experiment by TEM where lipid droplets were induced by myelin feeding, astrocytes were continuously and repeatedly fed myelin every day for 3 days. In this experiment, cells were lysed daily to monitor the progression of lipid droplet formation. Plin2 increased after each day of myelin feeding, but only reached a statistically significant increase after the 3rd day of feeding (**Figure 3.7A**). In the same western blot membranes, total MBP increased with repeated feedings. Plin2 and MBP both increased over the course of the feedings and may indicate that the astrocytes form lipid droplets when MBP is not efficiently degraded.

The feeding regimen of 24 hrs of myelin exposure was re-examined and time points were taken every day following myelin wash out. Plin2 expression was unchanged and MBP showed a progressive decrease over the 3 day time course (**Figure 3.7B)**. The lack of Plin2 induction was mostly likely because the myelin was efficiently degraded and not accumulated. Cultured astrocytes were fed myelin for 1 hr and time points were taken within the next 24 hrs. Plin2 expression did not change in the time points measured subsequent to washout (**Figure 3.7C**). To consider the impact of brief but repeated myelin feeding, cultured astrocytes were fed for 1 hr per day for 3 days. Plin2 showed no significant increase at the end of 3 days (unfed cells $\bar{x} = 0.1$ (SD 1.1); fed cells $\bar{x} = 0.3$ (SD 1.1); N = 3, unpaired two-tailed t-test, $p = 0.2$). In these conditions where MBP was reduced by the end of the time course, there was no significant increase in Plin2 expression.

Myelin was degraded by astrocytes, but the efficiency was reduced when the exposure to myelin was extended from 1 hr to 24 hrs. When myelin was accumulated after repeated and continuous myelin feeding, the astrocytes formed lipid droplets. Lipid droplet formation was seen by TEM, ORO staining, Plin2 immunofluorescence, and Plin2 immunoreactivity by western blotting. Plin2 expression was consistent with the formation of lipid droplets in astrocytes. The break down or liberation of lipids is a prerequisite for the formation of lipid droplets, suggesting that myelin degradation still occurred even if overall MBP levels did not decrease. The cellular machinery used to break down myelin appeared to be overwhelmed by the increased myelin load. Lipid droplets formed when the astrocytes could not efficiently degrade myelin.

Plin2 increases in ONH astrocytes in mouse glaucoma models

Because Plin2 appeared to report lipid droplet formation, we quantified Plin2 expression in D2 ONHs to corroborate the putative lipid droplets identified in D2 ONH by SBEM. Western blotting was used first to determine whether there was increased Plin2 expression in 10-mo-old D2 and D2-Gpnmb$^+$ ONHs. Plin2 increased by 3.8-fold in the ONH of D2 mice ($\bar{x}$ = 4.1, SEM 0.6, N = 9) compared to control ONH (D2-Gpnmb$^+$ $\bar{x}$ = 1.1 SEM 0.1, N = 5) (**Figure 3.8A top, B left**).

The expression of Lgals3 was also examined because we hypothesized that Lgals3 was reactive in response to phagocytic activity by the astrocytes. Lgals3 increased by 3.6-fold (D2-Gpnmb$^+$ $\bar{x}$ = 1.0, SEM 0.1, N = 5; D2 $\bar{x}$ = 3.7, SEM 0.8, N = 9) (**Figure 3.8A bottom, B right**). Previous quantifications of Lgals3 by immunofluorescence using MSV provided a wide range of fold-change in D2 [11]. Quantification of Lgals3 protein in western blot here provided an additional measure of expression. Most measures of Lgals3 in D2 [11; 188-190] calculated a 2 to 4-fold increase in D2 over D2-Gpnmb$^+$ by immunofluorescence and messenger RNA (mRNA) microarray. One MSV quantification out of 3 resulted in a 25-fold increase in Lgals3 (Chapter 2). That quantification may be an overestimate due to anomalies in quantification of that dataset or insufficient sample of D2 phenotypes.

It was necessary to return to imaging methods to determine what cell type expressed Plin2. First we determined whether Plin2 was increased in the D2 cohort to be used for analysis. A significant Plin2 increase was seen over a range of segmentation values ($p < 0.001$ using unpaired t-test with Welch's correction), with the mean fold-change of 5.8 (SEM 0.2) (**Figure 3.8C)**. SV410 contains values closest to this mean where D2-Gpnmb$^+$ $\bar{x}$ = 0.17 (SEM 0.03, N = 11) and D2 $\bar{x}$ = 0.99 (SEM 0.17, N = 13).

Plin2 was also quantified in a second mouse model of glaucoma using MSV. This model induced elevated IOP after translimbal laser photocoagulation in an experiment that was previously reported [11]. There was a 10.3 (SEM 0.8) mean fold-change of Plin2 in ONH from lasered eyes versus unlasered eyes (**Figure 3.8D**). At SV350, the mean of untreated eyes was 0.2 (SEM 0.1, N = 7) and of lasered eyes was 2.4 (SEM 0.6, N = 11).

Then, we were able to determine in which cell type Plin2 upregulation occurred. Plin2 immunoreactivity was analyzed with respect to markers that identify the MTZ astrocytes (Lgals3) and microglia (Iba1) using images taken from the D2 nerves quantified in Figure 3.8D. Although Lgals3 also expressed in some microglia, the majority of Lgals3 signal in the MTZ was in GFAP$^+$ astrocytes [11]. An image mask of either Lgals3 or Iba1 expression was created and the Plin2 expression within each mask was quantified. MSV were used for each gene, with Plin2 signal normalized by each progressively smaller mask area (**Figure 3.9B**). Higher segmentation of Plin2 represents more stringent conditions for the detection of Plin2 signal and a positive slope indicates co-localization. Plin2 after translimbal laser photocoagulation was also increased in Lgals3-expressing astrocytes (data not shown). The quantifications were in agreement with the images obtained from the dataset that qualitatively showed the majority of Plin2 signal within Lgals3 expression (**Figure 3.9A**). The results show that astrocytes form lipid droplets during glaucomatous degeneration.

Discussion

Myelin instability in the MTZ

The MTZ had myelin irregularities seen by reactivity to QD-9 and ultrastructurally by SBEM. These observations suggest that myelin in the MTZ inherently forms more myelin protrusions and myelin bodies as compared with regions more distal to the ONH. This could be interpreted as increased myelin turnover and may be due to damage from daily stress or age, but appeared to be a normal biological process. Myelin turnover mostly likely does not result in a net loss of myelin because new myelin segments can be generated by adult-born oligodendrocytes that intercalate with existing sheaths [250]. EM of adult rat MTZ, or the retina-optic nerve junction as it was called, observed both axon and myelin protrusions at heminodes [18]. Heminodes contain one paranode and juxtaparanode region, as compared to paired regions in a full node of Ranvier. Node length and internode length were of varying lengths in the MTZ and some paranodal loops were only partially attached or faced in the opposite direction of its axon. It was suggested that the axo-glial interactions appeared to be immature or to have prematurely arrested development. The results described here would support the idea that myelin or heminode architecture in the MTZ may appear immature, but I propose that it is not due to arrested development, but is instead due to constant remodeling through the phagocytic activity of astrocytes.

In multiple sclerosis, optic neuritis causes demyelination but does not necessary lead directly to axon loss. Treating the inflammation caused by optic neuritis with steroids can improve vision temporarily, but vision is unlikely to be completely restored without full remyelination [251; 252]. Animal models that induce focal demyelination in the optic nerve do not typically show remyelination [253; 254]. One study examined the effects of irradiated food on cats and found extensive demyelination with accompanying motor defects [255]. After the irradiated food was withdrawn, axons in the spinal cord and optic nerve had thin myelin sheaths which indicated that remyelination had occurred. This work demonstrated that remyelination was possible, but the mechanism or circumstances required are unknown. If there is constant myelin turnover and remyelination in the MTZ, then it may be a novel model to study the stability of myelination, dysmyelination, and integrity of nodes of Ranvier without added complications from using a disease model.

Phagocytic activity of astrocytes

We previously reported microglial and astrocyte expression of Lgals3 in the myelinated optic nerve [11; 104] but expression was especially strong in astrocytes of the MTZ [11]. There was also a reported increase in transcriptional expression of *Lgals3* in all stages of D2 disease examined [188-190]. Cultured astrocytes that did not express Lgals3 still had internalized myelin. This may be due to the activation of a phagocytic pathway that is independent of Lgals3 or because the culture system permitted activity that would not be typically seen *in vivo*.

We observed cultured astrocytes fed myelin containing no MPB immunoreactivity and other cells that had numerous bodies of MBP immunoreactivity. The variance in phagocytic activity of cultured astrocytes was also observed in a model where astrocytes phagocytosed apoptotic neurons [202]. These results suggest that the phagocytic ability of astrocytes may be limited to a subpopulation of astrocytes. This is consistent with the idea that MTZ astrocytes expressing Lgals3 are involved in myelin phagocytosis. Cultured astrocytes that do not express Lgals3 but still internalize myelin may reflect an inherent ability of astrocytes. The difference in *in vitro* versus *in vivo* context may explain the variable expression of Lgals3 in culture.

It was also reported that an acidic pH-sensitive fluorescent marker was not activated in astrocytes with internalized nuclei within 3 days, yet macrophages contained fluorescence within 5 hrs [202]. This result indicated that macrophages use lysosomes to degrade neuronal nuclei, but astrocytes did not use lysosomes nor did they degrade nuclei within the time frame observed. My own experiments with lysosomal proteins LAMP1, LAMP2, and cathepsin D showed no reproducible colocalization with internalized myelin.

Immunofluorescence demonstrated that myelin was stored in the astrocyte cytoplasm when the exposure to myelin was extended from 1 hr to 24 hrs. However, MBP was decreased by western blot using the same time course. MBP by immunofluorescence was normalized by Day 1 values while MBP in western blotting was normalized to actin. The amount of internalized myelin may have been small compared to the total amount of myelin added to the culture. Western blot may not be sensitive enough to detect this amount. Imaging techniques are useful for studying subtle changes or to localize genes of interest within a certain cellular compartment or region, but analysis is limited to the area imaged. Western blots require larger changes in protein expression to be detectable, but may better reflect the tissue as a whole. The complementary nature of these two methods should be considered when examining subtle biology.

Myelin was accumulated by western blot in the continuous and repeated myelin feeding experiment and this was the only condition to produce Plin2 expression. Shorter exposures did not lead to Plin2 expression. We reasoned that the cellular machinery used to metabolize myelin proteins and lipids became overwhelmed with the increased myelin load. The inability to degrade internalized material may eventually result in negative consequences to the astrocyte. MTT assay did not show differences in the viability of astrocytes fed myelin but the long-term consequences on viability or cell biology were not examined.

Optic nerve astrocytes are not the only non-professional phagocyte in the visual system. Retinal pigmented epithelial (RPE) cells actively phagocytose the outer segments of photoreceptors in the retina [256]. In age-related macular degeneration, RPE cells accumulate non-degradable remnants called lipofuscin [257; 258]. The accumulation of lipofuscin in cultured retinal pigment epithelial cells was observed to inhibit further phagocytosis [259] and could possibly have other negative effects on the health of the outer retina [260; 261]. In the absence of dysfunction, RPE cells form retinyl-ester containing lipid droplets called retinosomes. Lipofuscin is distinct from retinosomes [262; 263]. Retinosomes have a place in the normal biology of RPE cells by facilitating the recycling of 11-*cis*-retinal, which is a chromophore used by photoreceptors to capture photons [263]. Similar to RPE cells and retinosome formation, astrocytes in the ONH were also shown to be phagocytic and form lipid droplets.

Significance of lipid droplets in the ONH

Cells containing excess lipids typically esterify and store them in lipid droplets [264; 265]. There are a wide variety of functions that lipid droplets are proposed to do, but the standard view is that they are lipid storage organelles. It is unclear whether astrocytic lipid droplets might have a function beyond lipid storage, but the evidence observed thus far supports this simple view of excess lipid storage. Astrocytes that do not accumulate lipid droplets after myelin internalization may have recycled the lipids for energy or membrane remodeling [266].

Lipid droplets quantified in SBEM volumes of the MTZ of D2 (mild) showed an increase in lipid droplet formation before the laminar region, and there were equally high numbers of lipid droplets in the glial lamina and MTZ of D2 (severe). This suggests MTZ astrocytes respond to a stimulus prior to or faster than glial laminar astrocytes, or that the MTZ was the site for the stimulus inducing lipid droplet formation before the glial lamina. The lack of biological replicates prevents strong conclusions from being made from this particular dataset, but other results shown here suggest that the MTZ is a dynamic region with increased myelin irregularities and astrocytes that might be more sensitized for phagocytic activity. As suggested by our ultrastructural and *in vitro* myelin feeding experiments, we propose that lipid droplet accumulation is due to repeated myelin internalization by astrocytes.

Lipid droplets observed in myelin- and oleic acid-fed cultured astrocyte were primarily of 2 different forms, with the larger lipid droplet containing an electron-lucent core and the smaller lipid droplet being primarily electron-dense. The osmiophilic appearance may reflect the bulk incorporation of different myelin lipid species and the electron-lucent core may represent diffusion of lipids within the droplet [267; 268]. To test this hypothesis, cultured astrocytes should be collected at time points after lipid stimulation and examined by TEM. A fully matured lipid droplet should appear electron-lucent using our method of EM processing.

Lipid droplet formation in astrocytes might be interpreted as a sign of pathology. If the astrocytes excessively phagocytose myelin, this may secondarily affect some of their other normal functions, similar to how lipofuscin accumulation affects RPE cells. A gradual disabling of phagocytic astrocytes through decreased myelin internalization and accumulation of myelin or lipid droplets could be a contributor to slowly progressing diseases like glaucoma.

Acknowledgements

I would like to thank Abbot Clark for providing bovine optic nerve tissue used in pilot studies of myelin phagocytosis by cultured astrocytes; Lynette Foo and Ben Barres for providing astrocyte culturing advice; Carole Sztalryd Woodle for providing perilipin antibodies; and Paul Watkins for providing peroxisome antibodies and lipid droplet dyes, as well as helpful discussions about lipid droplets. This work was supported by a Catalyst for the Cure grant from the Glaucoma Research Foundation and 1RO1EY019960 (NM-A). I thank the Johns Hopkins University Department of Neuroscience Imaging & Physiology Core funded by the National Institute of Neurological Disorders and Stroke (Grant number NS050274) and the Wilmer Eye Institute at Johns Hopkins Microscopy and Imaging Core Facility for access to equipment.

Figures

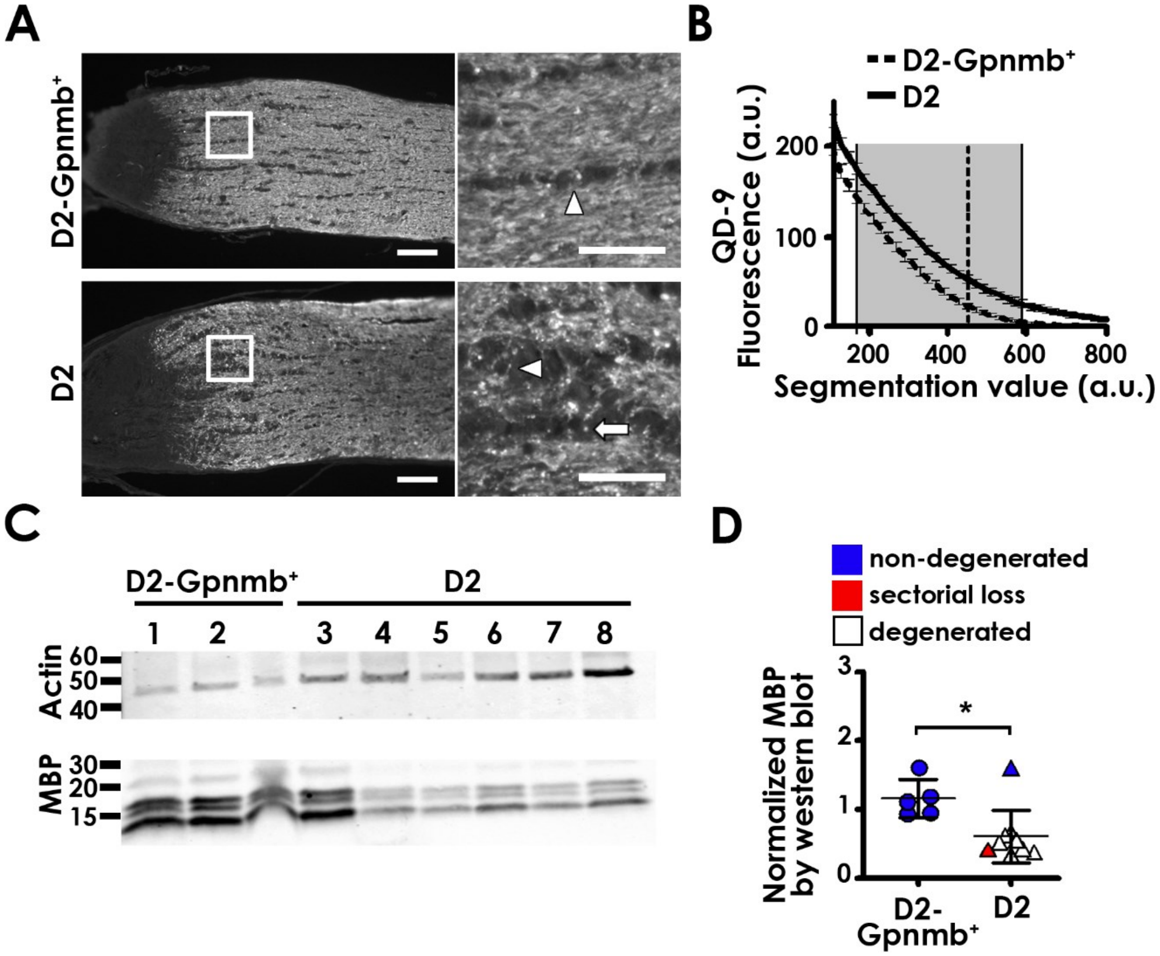

Figure 3.1. QD-9 reactivity and myelin loss in D2. A. Immunofluorescence labeling of QD-9 in ONH of D2 and D2-Gpnmb$^+$. Region in white box magnified at right. Some small, highly immunofluorescent QD-9 objects appeared detached (arrow) from myelin sheaths and other QD-9 objects appeared to have a thin protrusion extending away from the myelin sheaths (arrowheads). **B.** MSV quantification of ONH labeled with QD-9. Shaded region contains SV where values in the two groups are different at a Student's unpaired t-test with Welch's correction significance level of $p < 0.005$. Vertical dotted

line is SV closest to mean fold-change within shaded region; error bars are SEM. **C, D.** Western blot and quantification from individual optic nerves for MBP and actin (MW = 42 kDa) for as a loading control. Three isoforms of MBP (MW = 18, 17, 14 kDa) were cumulatively quantified from each nerve and normalized by mean signal in D2-Gpnmb^{+}. Nerves were classified as non-degenerated (Lanes 1, 2, 3; blue), sectorial degeneration (Lane 5; red), or late degenerated (Lanes 6, 7, 8; white). Additional western blot of ONH not shown. *p* = 0.01 in two-tailed, unpaired t-test with Welch's correction; error bars are SD. (Scale bars, A: 70μm left, 20μm right.)

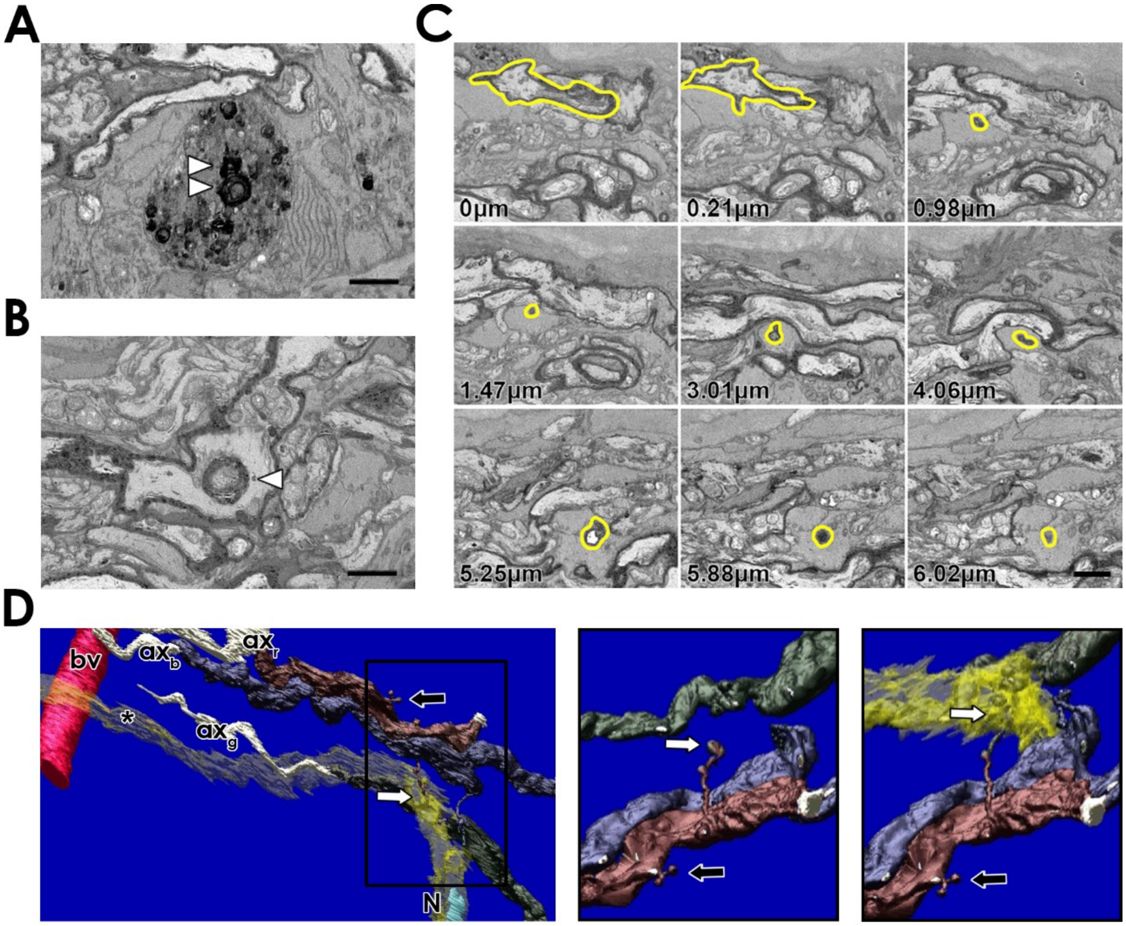

Figure 3.2. Myelin irregularities in C57Bl/6J MTZ. A, B, C. SBEM of irregular myelin in a non-degenerated ONH. **A.** Debris contained concentric rings of electron density (arrowheads) similar to the period lines of compact myelin. **B.** An oblique cutting plane of a myelinated axon that was folded back onto itself (arrowhead). **C.** A series of Z-sections of a myelin protrusion. Panel showing distance at 0µm highlighted a typical myelinated axon (yellow). Advancing through the Z plane revealed a myelin protrusion projecting away from the myelin sheath. **D.** A 3D reconstruction of the myelin protrusion in C (dark red, ax_r). Nearby myelin sheaths (green, ax_g and blue, ax_b) were also traced. Black box highlights region of myelin protrusions (enlarged images shown to the right) inside of an astrocyte process (yellow) that also associated with a blood vessel (bv).

Center and right images are rotated views of myelin protrusions with and without the overlay of the astrocyte process. A long protrusion was inside the astrocyte process (white arrow) and smaller protrusions were observed nearby on the same axon (black arrow). N = nucleus. (Scale bars, A, B, C: 2µm.)

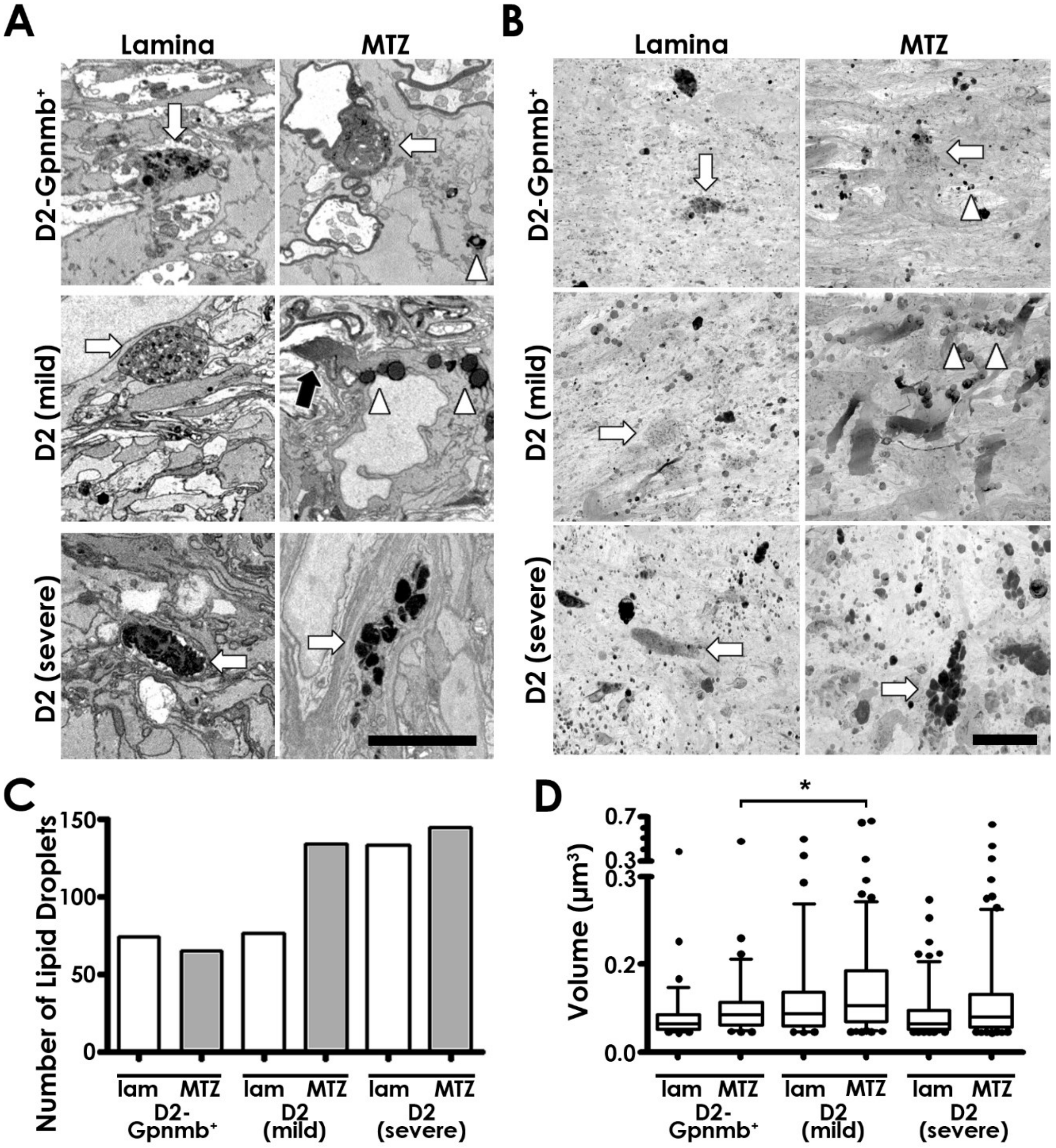

Figure 3.3. Osmiophilic irregularities in SBEM from D2 and D2-Gpnmb$^+$ ONH. A. Irregular structures from the glial lamina and MTZ containing granular debris or myelin bodies (arrows) and spherical structures putatively called lipid droplets (arrowheads). Gradient of electron density in a glial process in MTZ of a mildly diseased optic nerve (black arrow). **B.** Reduced field of view using minimum intensity projections of

subvolumes with white arrows and arrowheads pointing to same structures in A. **C, D.** Automated quantification of SBEM electron-dense spherical lipid droplets. **C**, Total number of lipid droplets counted from minimum intensity projections. The mildly diseased D2 showed a difference between the number of lipid droplets in the glial lamina and MTZ. **D**, Box-and whiskers-plot (5-95 percentiles) of lipid droplet volumes. 1-way ANOVA ($p < 0.001$) with Tukey's comparison, pair-wise significance only considered between lamina and MTZ within each nerve, all laminas, or all MTZs (* = $p < 0.05$). Error bars are SD. (Scale bars, A, B: 5μm.)

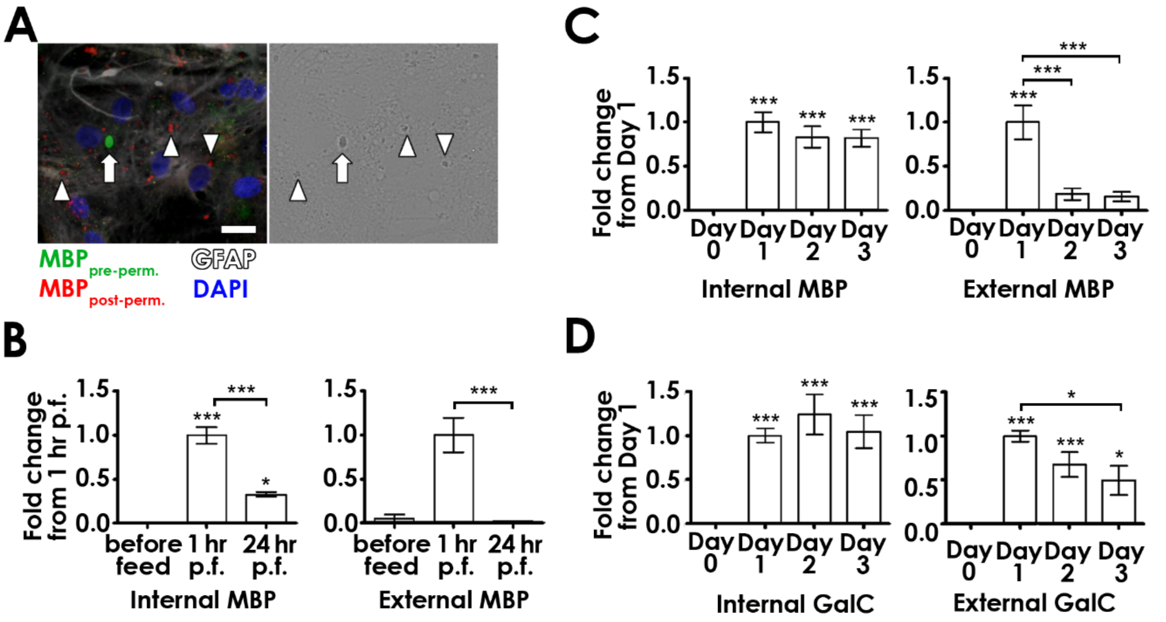

Figure 3.4. Immunofluorescence of myelin internalization by cultured astrocytes. A. Antibody localization of MBP before (green) and after (red) membrane permeabilization (left). External MBP (arrows) and internalized MBP (arrowheads) were on top of or inside of, respectively, astrocytes labeled by GFAP (white). Myelin debris was visible by differential interference contrast (right). **B, C, D.** Quantification of immunofluorescence in cultured astrocytes after myelin feeding. Calculated Internal values and External values were normalized to the mean fluorescence in 1 hr or Day 1 fluorescence. Error bars show SEM. **B.** Myelin was fed to astrocytes for 1 hr before washout. MBP decreased after washout; 1-way ANOVA for Internal and External $p < 0.001$. **C, D.** MBP (C) and GalC (D) after myelin was fed continuously for 1 day before wash out. Internal MBP and GalC levels were unchanged after washout. 1-way ANOVA for Internal and External in C is $p < 0.001$. 1-way ANOVA for D, Internal is $p < 0.001$ and D, External is $p = 0.002$. Post-hoc pair-wise Tukey analysis performed against Day 0 or as indicated, * = $0.01 < p < 0.05$; *** = $p < 0.001$. (Scale bar, A: 20µm.)

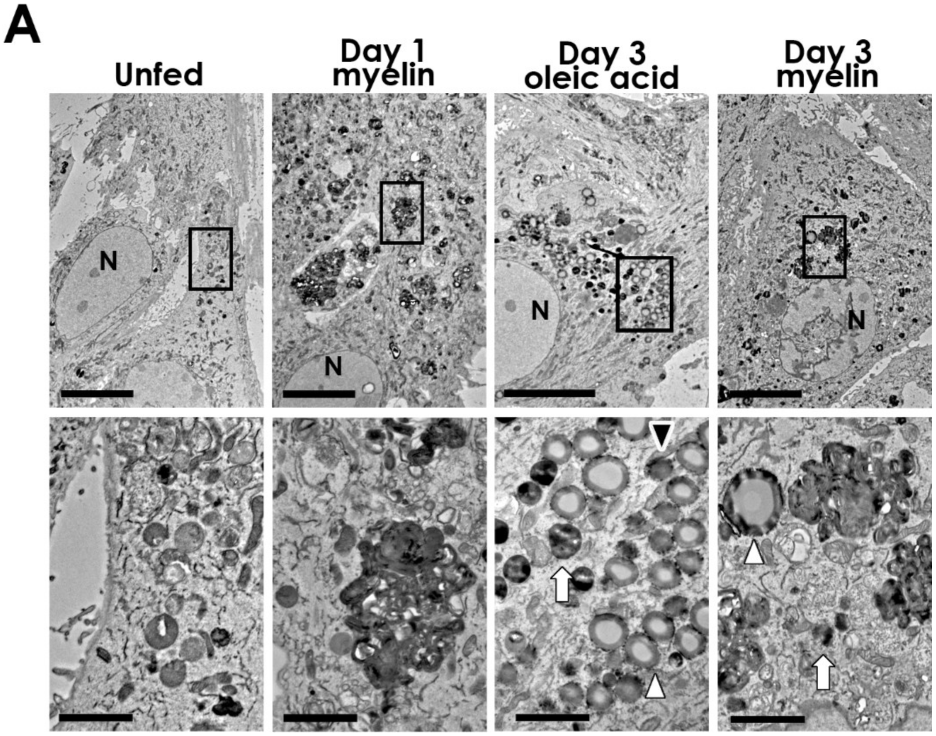

Figure 3.5. TEM of myelin debris and lipid droplets in cultured astrocytes. A. TEM of myelin- or oleic acid-fed astrocytes. Myelin debris was visible as large, irregularly shaped electron-dense structures (Day 1 myelin). Oleic acid incubation resulted in numerous large, spherical structures with an electron-lucent core (white arrowhead), smaller osmiophilic structures with irregular electron-density (white arrow), as well as a spherical structure that appeared to be an intermediate form of the two (black arrowhead). Repeated and continuous myelin feeding (Day 3 myelin) contained myelin debris and structures similar to those found after oleic acid incubation. N = nucleus. (Scale bars, A: 20µm; D, left: 10 µm, right: 2 µm.)

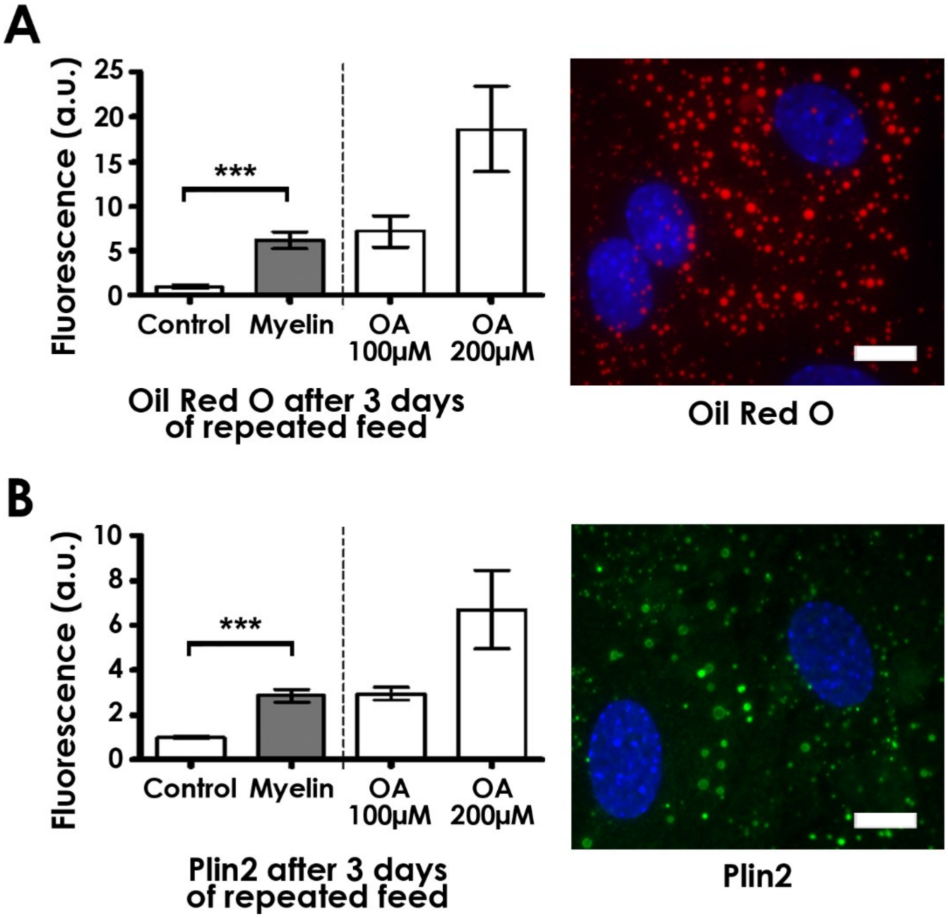

Figure 3.6. ORO and Plin2 fluorescence increased after myelin or oleic acid feeding. **A, B.** Quantification of Oil Red O fluorescence (A) or Plin2 immunofluorescence (B) by microscopy after 3 days of repeated and continuous feeding. Error bars show SEM. Two-tailed, unpaired t-test $p < 0.001$ between control and myelin-fed for ORO and Plin2. Images of ORO in lipid droplet core after oleic acid (OA) feeding (A, right) and Plin2 surrounding lipid droplet membrane after myelin feeding (B, right). Shaded bars indicate samples with myelin added. (Scale bar, 10μm.)

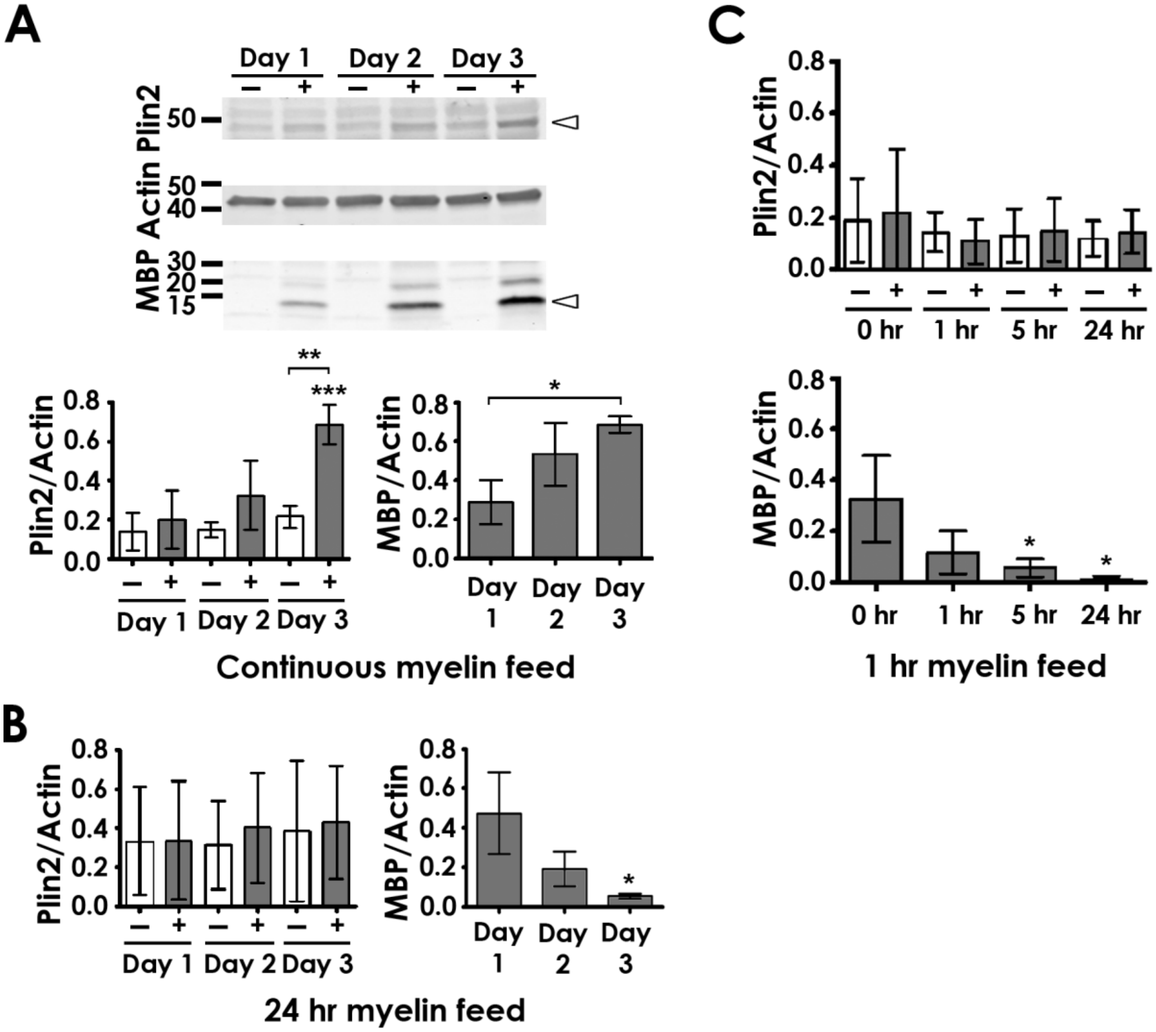

Figure 3.7. Plin2 response after myelin feeding regimens. A. Continuous and repeated myelin feeding induced progressive Plin2 and MBP accumulation. Western blot of Plin2 (MW = 47 kDa) and MBP (only 14 kDa band quantified, arrow) normalized against actin loading control showing errors bars with SD. 1-way ANOVA Plin2 $p < 0.001$; MBP $p = 0.02$. **B, C.** Myelin fed for 24 hrs (B) or 1 hr (C) had no change in Plin2. B, 1-way ANOVA Plin2 $p = 1.0$; MBP $p = 0.02$. C, 1-way ANOVA Plin2 $p = 0.98$; MBP $p = 0.02$. Pair-wise comparisons using post-hoc Tukey test against Day 1-, 0 hr-, or as indicated, * = $0.01 < p < 0.05$. Shaded bars indicate samples with myelin added.

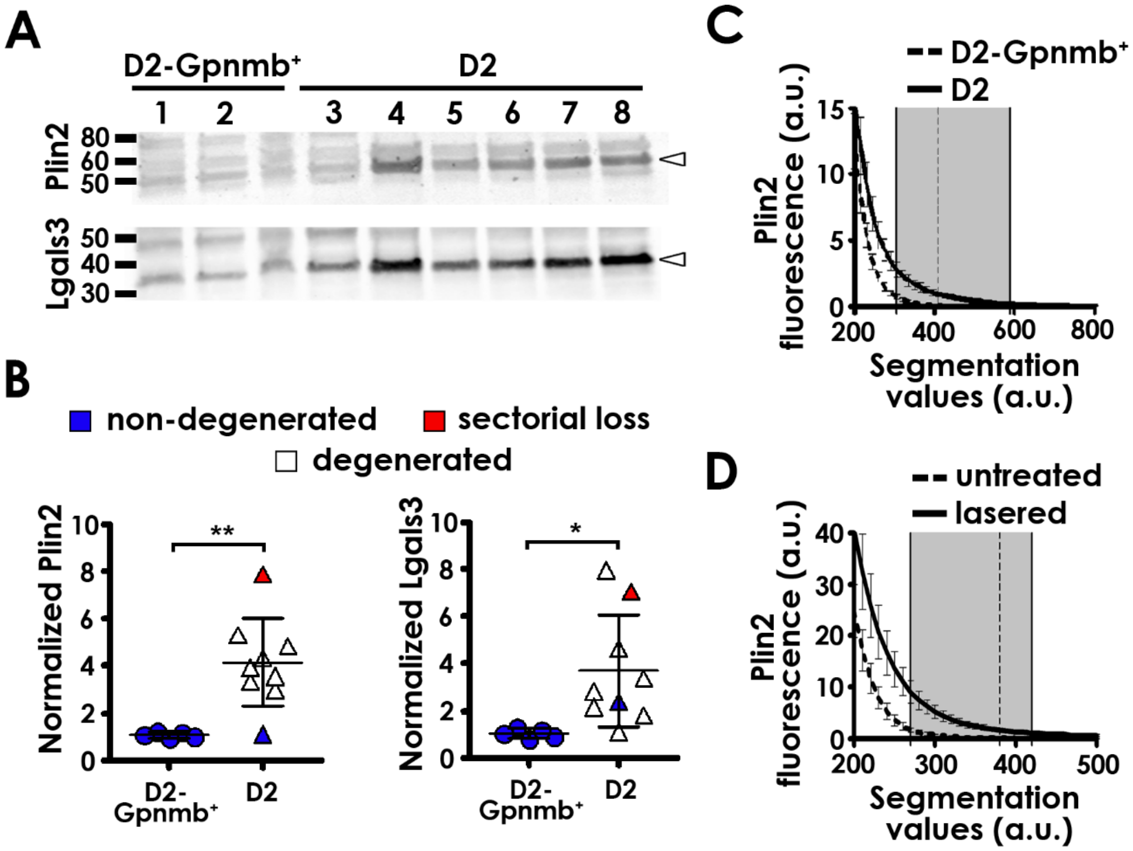

Figure 3.8. Plin2 increased in mouse glaucoma models. A, B. Western blot of Plin2 and Lgals3 (MW = 32 kDa) normalized to actin in same ONH from Figure 3.1C. D2 with axon loss all contained higher Plin2 and Lgals3 expression than D2-Gpnmb$^+$ or D2 with NND. As before, Lanes 1, 2, 3 = non-degenerated, Lane 5 = sectorial degeneration, and Lanes 6, 7, 8 = late degeneration. Two-tailed unpaired t-test with Welch's correction, Plin2 $p = 0.001$; Lgals3 $p = 0.01$, error bars with SD. **C, D.** MSV of Plin2 fluorescence increased in D2 (C) and translimbal laser photocoagulation model (D). Vertical dotted line indicates segmentation value closest to mean fold-change of SV under shaded region. D, shaded region contains $p < 0.001$, using unpaired t-test with Welch's correction; error bars with SEM. E, shaded region contains $p < 0.01$, using unpaired t-test with Welch's correction; error bars with SEM.

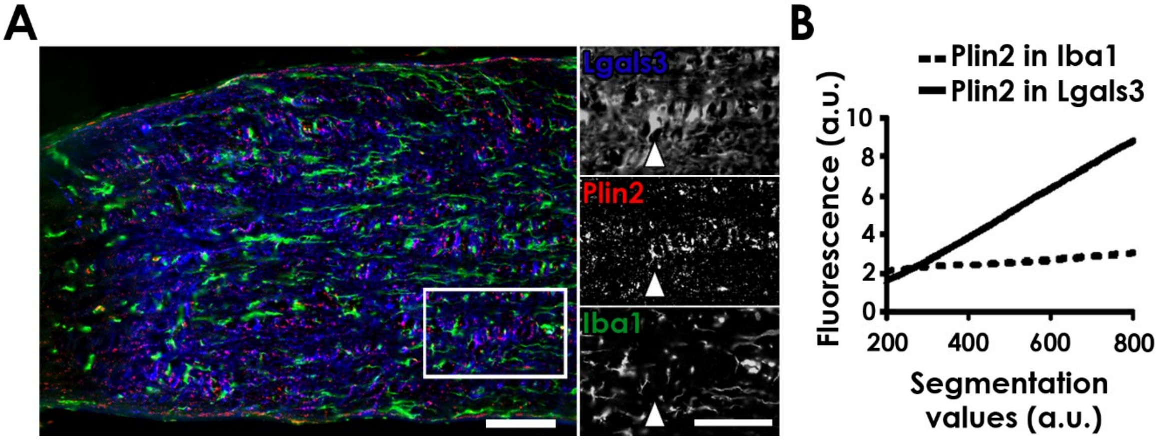

Figure 3.9. Plin2 localized to Lgals3$^+$ astrocytes in D2 and D2-Gpnmb$^+$ ONH.

A. Immunofluorescence labeling of astrocytes (Lgals3, blue), microglia (Iba1, green), and lipid droplets (Plin2, red). Plin2 signal was predominantly localized to Lgals3-expressing astrocytes and not Iba1-expressing microglia (arrowhead). **B.** Colocalization measured by Plin2 signal segmented within a mask layer of astrocytes (solid line) or microglia (dashed line). A neutral slope indicated no specificity of Plin2 within the microglia mask and a positive slope indicated co-localization of Plin2 within the astrocyte mask. (Scale bars, A: 70µm.)

Appendix A: The appearance of protease-resistant Sncg on lipid droplets in cultured cells and in axonal swellings Plin2$^{\Delta 2\text{-}3}$ mouse ONH

Preface

Appendix B contains unpublished data regarding proteinase K-resistance of Sncg on lipid droplets and in optic nerves.

Transmission electron microscopy of cells in Figure AppA7.1 was performed by Chung-ha Davis.

All other work was original data generated by JVN under the supervision of Nicholas Marsh-Armstrong.

Introduction

Lipid droplets are ubiquitous organelles that contain a neutral lipid core, made up of primarily triacylglycerols (TAGs) and sterol esters enclosed within a single membrane consisting of mostly phospholipids. The neutral lipid composition can be diverse [269] and TAGs in storage may be metabolized for energy [270]. Lipids from lipid droplets have also been suggested to be used in cellular membrane remodeling [265; 266]. In the retina, lipid droplets formed by retinal pigment epithelial (RPE) cells are called retinyl ester storage particles, or retinosomes [263; 271]. This unique name reflects the storage of retinyl esters as opposed to TAGs or sterol esters. RPE cells must constantly supply photoreceptors with 11-*cis*-retinal, the chromophore used in light capture. After photoisomerization of the chromophore, the photoreceptor will shed its outer segments containing the chromophore. RPE cells phagocytose the shed material. The internalized chromophore is then esterified and stored in the retinosome. Subsequent isomerization and oxidation of the retinyl ester results in a regenerated 11-*cis*-retinal chromophore [263]. Retinosomes have been associated with Plin2 [262] and are distinct from lipofuscin [262; 263], which are autofluorescent, non-degradable lipids and proteins that aggregate in the RPE. Lipofuscin accumulation is associated with age-related macular degeneration [258; 260; 261]. The function of lipid droplets in RPE cells in recycling 11-*cis*-retinal demonstrates that lipid droplets play an important role in the visual system.

The lipid droplet membrane can associate with many different proteins but the main lipid droplet proteins come from the PAT family of genes [272; 273]. The PAT family was recognized through structural similarities and functional association with lipid droplets. The original members of the family include *Plin1 (Perilipin-1), Plin2 (Adipose* *differentiation-related protein/Adipophilin),* and *Plin3 (Tail interacting protein of 47 kDa/Mannose-6-phosphate receptor binding protein 1)* [273]. *Plin4 (S3-12)* and *Plin5 (Lipid storage droplet protein 5/Oxidative PAT)* were subsequently added to the family.

Perilipins are expressed at high levels in adipocytes and steroidogenic cells [247; 274]. Cells in different tissues may express different combinations of PAT proteins and even lipid droplets within an individual cell can express a different assortment of PAT proteins [247; 270]. *Plin2* and *Plin3* may be of greater relevance to study lipid droplets in the central nervous system (CNS) because the expression of both genes are found in more cell types than other PAT proteins [247; 248]. However, Plin3 expression is stable in the cytosol without association with lipid droplets [275]. Plin3 may identify nascent lipid droplets [275] that serve other functions besides storing accumulated lipids. Plin2 is only stable when associated with lipid droplets [249]. The stabilization of Plin2 by lipid droplets may make it a better marker to identify putative lipid droplets in cells.

Plin2 was first identified through an increase in mRNA expression during adipocyte differentiation of the 1246 cell line derived from C3H mouse teratoma [276]. Plin2 expression may have a role in the differentiation of adipocytes, but can also perform functions in other cell types [247]. Plin2 had a slight preference for TAG-rich lipid droplets in multiple cell lines [277] and is believed to have a role in preventing lipolytic activity, specifically by inhibiting the access of ATGL to TAGs [278; 279].

There may be a novel role for Plin2 in regulating the localization of SNAP-23, a SNARE protein, to lipid droplets [280]. The overexpression of Plin2 in cultured cells segregated SNAP-23 away from glucose transporter vesicles and over to lipid droplets. This is an interesting concept because gamma synuclein (Sncg), a gene highly expressed in retinal ganglion cells (RGCs), was also suggested to protect TAGs from ATGL-mediated lipolysis and interact with SNAP-23 [281]. Knockdown of Sncg in 3T3-L1 adipocytes increased the associate of ATGL with lipid droplets. Sncg was proposed to act as a chaperone for SNAP-23 by regulating its assembly with the SNARE complex that forms on the surface of lipid droplets. The formation of the SNARE complex is proposed to mediate lipid droplet fusion, which would be akin to synaptic vesicle fusion. Plin2 was also proposed to have a role in mediating milk lipid globule (MLG) secretion in mammary glands [282; 283]. Plin2 was found to be a constituent of MLGs and was proposed to act as an adaptor molecule that assists in the association of the MLG to the plasma membrane, butyrophilins, and/or xanthine oxidoreductase. Butyrophilins and xanthine oxidoreducatase are proteins involved in MLG secretion that is distinct from a classical secretory pathway that uses exocytosis [283; 284]. The intersection of lipid droplet biology and synaptic vesicle biogenesis may provide the insight needed to understand the role Sncg may have outside the CNS and the role Plin2 may have within the CNS.

Lipid droplets were typically regarded as sites to store excess lipids, but increasing research suggests that the presence of neutral lipids and the lipid droplet membrane can have additional roles in cell biology [264; 265; 268; 285-287]. We found that Sncg localized to lipid droplets in 661W cells, a transformed mouse photoreceptor line that was thought to be a rat RGC line [288; 289]. At the time of the initial experiments described here, 661W were called RGC-5 cells and our confirmation of its mouse origin restricted our further use of the cells. The unexpected localization of Sncg to lipid droplets in 661W cells led us to discover lipid droplets in the optic nerve (Chapter

3). Here I report experiments performed to understand whether there was a relationship among Sncg, lipid droplets, and Plin2.

Results

Sncg localized to lipid droplets in 661W cells are PK-resistant

Cultured 661W cells formed lipid droplets in culture media containing 10% fetal bovine serum that naturally contains a mixture of fatty acids and cholesterol. The addition of oleic acid increased the number and size of lipid droplets (personal observations). 661W cells were cultured in media supplemented with 30µM oleic acid for 24 hours to increase lipid droplet formation. After fixation, lipid droplets were labeled with the fluorescent neutral lipid dye BODIPY **(Figure AppA.1A)** or an antibody against Plin2 **(Figure AppA.1B)**, and an antibody against the C-terminal domain of Sncg, $\text{Sncg}^{\text{aa108-123}}$. BODIPY dye formed spherical structures in the cytoplasm and Sncg localized around the perimeter of BODIPY^{+} lipid droplets. Plin2 also labeled the perimeter of lipid droplets and colocalized with Sncg. Sncg appeared as small puncta decorating the surface of the lipid droplet, but had a smoother, more membranous appearance on larger lipid droplets. Plin2 typically appeared membranous, but not continuous, around the lipid droplet membrane. BODIPY and Plin2 are two common lipid droplet markers that labeled lipid droplets in 661W cells. Sncg was a third marker not previously associated with lipid droplets.

Because alpha synuclein (Snca) displayed proteinase K (PK) -resistant qualities in certain types of pathology [184; 185] and Sncg shared structural similarities to Snca [290; 291], we also examined whether Sncg was PK-resistant in cultured cells. The antibody against Sncg$^{aa21-127}$ was PK-sensitive and had diffuse, nuclear localization before PK treatment. After PK treatment, Sncg$^{aa21-127}$ labeling was abolished. The diffuse, cytosolic population of Sncg$^{aa108-123}$ labeling was reduced after PK treatment, but the Sncg$^{aa108-123}$ immunofluorescence that localized to lipid droplets remained robust after PK treatment. These experiments have shown that not only does Sncg associate with lipid droplets, but also that the C-terminus specifically associated with lipid droplets and was PK-resistant.

PK-resistant Sncg structures in Plin2$^{\Delta2-3}$ optic nerves specifically reactive against Sncg$^{aa108-123}$ antibody

Sncg was also PK-resistance in diseased optic nerve [11]. We hypothesized that Sncg might be found on lipid droplets in the CNS. Sncg was unreliably detected on lipid droplets in the optic nerve head (ONH), although some Sncg^{+} astrocytes and Lgals3^{+} astrocytes contained ring-shaped structures that were labeled with two antibodies for Sncg and with Plin2 antibody (data not shown).

The function of Plin2 may be redundant with other lipid droplet proteins. The knockdown of Plin2 expression in cultured cells resulted in other proteins and perilipins localizing to lipid droplets [247; 278], and Plin3 can functionally compensate for Plin2 [292]. To determine whether Sncg would localize to lipid droplets in the ONH if Plin2 were absent, the ONHs of Plin2-deficient mice (Plin2$^{\Delta2-3}$) were examined. The extensive labeling of Sncg in the optic nerve axons made it difficult to resolve whether Sncg formed structures that appeared to be lipid droplets (data not shown).

Although it was unclear whether there was a lipid droplet-associated phenotype of Sncg, two Sncg antibodies labeled unusual structures that were ranged from ~15µm-30µm along its long axis **(Figure AppA.3A, top row)**. ONHs were then treated with PK to determine whether the structures might be similar to pathological PK-resistant Snca structures. After treatment with PK, structures were only detected by Sncg$^{aa108\text{-}123}$ labeling **(Figure AppA.3A, bottom row)**. These structures appeared in Plin2$^{\Delta 2\text{-}3}$ ONH starting approximately at 6-7 months (mos) of age, and were typically larger and more numerous with increasing age. The Sncg structures may be indicative of an age-related disease.

We attempted to determine whether Sncg structures formed as a result of optic neuropathy. A glaucoma model using acute intraocular pressure increase (IOP) via translimbal laser photocoagulation was performed on two cohorts of Plin2$^{\Delta 2\text{-}3}$ mice and Balb/C mice, the background strain. One cohort included 3 to 5-mo-old mice (Balb/C N = 13; Plin2$^{\Delta 2\text{-}3}$ N = 16) and a second cohort included 7-mo-old mice (Balb/C N = 14; Plin2$^{\Delta 2\text{-}3}$ N = 10). Preliminary experiments indicated that Sncg structures did not form in young Plin2$^{\Delta 2\text{-}3}$ mice with optic nerve degeneration after IOP elevation. Thus, the Sncg structures appeared to be related to age, and not degeneration. Plin2 deficiency also did not appear to affect susceptibility to axon degeneration because the number of optic nerves with degeneration was similar to the number with degeneration in the control strain. However, the majority of these mice did not have axon loss and so our sample size for estimating susceptibility was small.

Sncg structures are intact, swollen axons

It was then considered that the Sncg structure might be a large axonal swelling. The only known marker that was reactive with the structure was Sncg$^{aa108\text{-}123}$. That antibody was unsuitable to use because Sncg$^{aa108\text{-}123}$ labeled all axons in the optic nerve and it was difficult to trace a single axon to the Sncg structure. To properly localize Sncg to the structure and also exclude the detection of endogenous mouse Sncg, a chimeric Sncg gene consisting of the first 1-110 amino acids (aa) of mouse Sncg was fused to the last 13 aa in the C-terminus of frog (*Xenopus tropicalis*) Sncg (xSncg). The retention of the mouse N-terminal sequence should prevent the disruption of lipid interactions by the protein. The frog C-terminal sequence can be selectively labeled using an antibody that does not cross react with mouse Sncg. A mini Singlet Oxygen Generator (miniSOG) tag [293] was also added to the C-terminal end of the chimeric Sncg gene. The transgene was packaged into an adeno-associated virus, serotype 2 (AAV2) and injected intravitreally. RCGs would be infected and express the transgene in the cell body and axons.

Cultured cells infected with the virus confirmed transgene expression and verified the specificity of the xSncg antibody **(Figure AppA.4A)**. Transgene expression was examined *in vivo* by injecting the virus into the eye of a Balb/C mouse. After 3 days of infection, few RGCs were labeled with xSncg antibody and miniSOG fluorescence **(Figure AppA.4B)**.

AAV2-mSncgX-miniSOG was unilaterally infected into the eyes of 10 to 12-mo-old Balb/C and Plin2$^{\Delta 2\text{-}3}$ mice. Tissue was harvested after 1 mo. PK treatment was applied to ONHs in order to reduce background labeling and enhance the reactivity of the transgene to the antibodies. The antibody against Sncg$^{aa108\text{-}123}$ labeled all axons in the nerve, as expected **(Figure AppA.5A)**. A fraction of axons were labeled using antibodies against xSncg **(Figure AppA.5B)** or miniSOG **(Figure AppA.5C)**. In Plin2$^{\Delta 2\text{-}3}$ ONH, Sncg structures were present and some structures appeared to be continuous with axons. It was inferred that all labeled structures were still connected to the proximal axon within the one month of infectivity because it was labeled by the transgene. The conclusion was that the Sncg structures were axon swellings that were likely forming in degenerating axons.

We previously observed that axon swellings may eventually be phagocytosed by astrocytes [11]. ONHs of 12-mo-old Plin2$^{\Delta 2\text{-}3}$ were labeled with Lgals3 to determine whether there would be Lgals3 reactivity surrounding the axon swelling. Lgals3 did not appear to have any particular reactivity with the Sncg structure (personal observations).

Swollen axons contain vesicular and granular material

Imaging by confocal microscopy showed that an axon swelling had irregular morphology **(Figure AppA.6A)**. One swelling initially appeared balloon-like, and then it gradually elongated into a tubular structure **(Figure AppA.6B)**. Individual Z-stacks resolved additional morphological detail inside the axon swellings. There was diffuse labeling in the axoplasm and also some spherical structure made up of puncta, which was reminiscent of Sncg decorating the membrane of lipid droplets.

Transmission electron microscopy (TEM) was used to examine the ultrastructure of the swellings and also determine the identity of the structures within the swellings. Axon swellings were frequently myelinated and interspersed among other myelinated axons that were typical in appearance **(Figure AppA.7A)**. Myelin sheaths appeared compact with period lines with no indications of abnormal myelin. The amount of material inside each swelling did not appear to determine the area of the swelling. Some swollen axons contained a relatively low density of granular and vesicular material, while other swollen axons had a high density of materials **(Figure AppA.7B)**. Some of the structures were identifiable as mitochondria.

Confocal imaging suggested that Sncg formed ring-like structures within the swelling. We previously observed Sncg on the periphery of lipid droplets, but none of the vesicles within the swellings had an appearance consistent with a lipid droplet. It is unclear which of the vesicles might contain Sncg.

One of the axon swellings identified did not appear myelinated **(Figure AppA.7B)**. Instead, it was enclosed on one side with a thin membrane. On the opposite side of the swelling, a membrane was not apparent and the granular contents appeared open to the glial cytoplasm. There were no other obvious signs of gliosis or degeneration in these nerves. The axon swellings were observed in aged transgenic mice with a Plin2 deficiency, in the absence of degeneration, by fluorescence imaging and TEM.

Discussion

I have reported here that Sncg localized to lipid droplets in the immortalized 661W cone photoreceptor cell line. There are conserved structural characteristics among the synuclein family that indicates that the N-terminal domain binds lipids while the C-terminal domain has relatively unrestricted movement [290; 291; 294-296]. Snca interacted with synthetic lipid vesicles *in vitro*, as well as to lipid droplets in Hela cells and primary hippocampal neurons [297]. Sncb also localized to lipid droplets in immortalized Hela cells. Sncg did not localize to lipid droplets in Hela cells [297] or adipocytes differentiated from mouse embryonic fibroblasts [281]. Therefore, the interaction of Sncg with lipid droplets appears context and cell-dependent. The characterization of the biology in which this interaction occurs may be informative of the function of Sncg.

There were two populations of Sncg that was labeled by antibodies directed against the N- or C- Sncg domains. It is unclear why the antibodies label distinct populations of Sncg. Sncg may have additional roles in gene regulation, in addition to cytoplasmic functions that regulate synaptic vesicles or lipid droplets.

We were interested in the possibility that Sncg may be sequestered on lipid droplets. Lipid droplets might serve as a binding domain that prevents Sncg from interacting with its target protein or membrane [264; 265; 287]. It may be one mechanism by which the cytoplasmic concentration of Sncg may be regulated. The morphology of the Sncg puncta around lipid droplets suggested discrete domains that bound Sncg. It also appeared that larger lipid droplets had more continuous labeling of Sncg. We did not perform any experiments that might address whether Sncg influenced the size of the lipid droplet by protecting the TAGs from lipolysis or whether the lipid droplet recruited Sncg to its surface. There did not appear to be any effects on cell viability when cells were fed with oleic acid to increase lipid droplet formation (personal observations). Sncg did not seem to have a pathogenic effect on 661W cells, but perhaps any effect of Sncg overexpression was neutralized by lipid droplet binding.

Axon swellings in Plin2$^{\Delta 2\text{-}3}$ were a dramatic phenotype that occurred with age. Axon swellings were primarily found in the myelinated portion of the optic nerve. The number of swellings in each nerve varied, but was generally limited to less than 10 for any given nerve examined. Axonal debris was removed from axons via similar swellings and protrusions in a C57Bl/6J mouse [11], but the protrusions in these control mice were not observed to be as large as those in aged Plin2$^{\Delta 2\text{-}3}$ mice. It is unclear why a Plin2 deficiency would cause this phenotype or whether the defect was due to a defect in the axon or glia.

I was unable to identify reagents to assess whether there was an impact on lipid droplet formation in Plin2$^{\Delta 2\text{-}3}$ optic nerve. Antibodies against Plin1, Plin2, Plin3, Plin5 were all tested in optic nerve tissue. Plin2 was the only antibody that had reproducible and detectable reactivity, and that was only in degenerated optic nerve tissue (Chapter 3). Other PAT proteins may not be expressed in the ONH or have even lower endogenous expression than Plin2. It is also possible that the other perilipin antibodies tested were not compatible with the protocols used for preparing and immunolabeling of frozen optic nerve sections. The lipid dyes BODIPY, Oil red O, and Nile Red were also ineffective at labeling lipid droplets in the ONH, perhaps due to the abundance of myelin. Those dyes clearly labeled lipid droplets in liver tissue. Oil red O may have labeled lipid droplets in the optic nerve but the labeling was not clear enough for quantitative purposes. Due to these limitations, I was not able to examine whether lipid droplet formation could be affected in Plin2$^{\Delta 2\text{-}3}$ mice. By TEM, Plin2$^{\Delta 2\text{-}3}$ mice (N = 2) did not show lipid droplet accumulation in astrocytes that was observed in degenerated DBA/2J optic nerve (Chapter 3). It is unclear whether the axonal dystrophies in Plin2$^{\Delta 2\text{-}3}$ mice were related to lipid droplet biology.

Plin2, and lipid droplet proteins in general, are not frequently observed or studied in the CNS. The Plin2$^{\Delta 2\text{-}3}$ mouse was shown to have a delayed dark adaptation response that affected photoreceptors and RPE cells [298]. RPEs also had reduced retinyl ester accumulation. This phenotype, and the swollen axons described here, may be the only described neurological phenotypes for Plin2$^{\Delta 2\text{-}3}$ mice. These experiments have generated more questions and provided little answers to the function of Sncg and the role of Plin2 in the CNS. It has suggested a possible effect of Plin2 expression in the CNS. It remains to be seen whether Sncg has a function in mediating lipid droplet fusion or vesicle formation in the optic nerve and whether Plin2 has a role in independent of lipid droplet association.

Acknowledgements

I would like to thank Paul Watkins for contributing of lipid droplet dyes and guidance; Carole Sztalyryd-Woodle for contributing perilipin antibodies; Krzysztof Palczewski for contributing Plin2$^{\Delta 2\text{-}3}$ mouse; John McDonald for access to the confocal microscope; Chung-ha Davis and Faizan Ali for performing translimbal laser photocoagulation surgeries; and Elizabeth Mills for generation of the chimeric Sncg fusion construct.

Figures

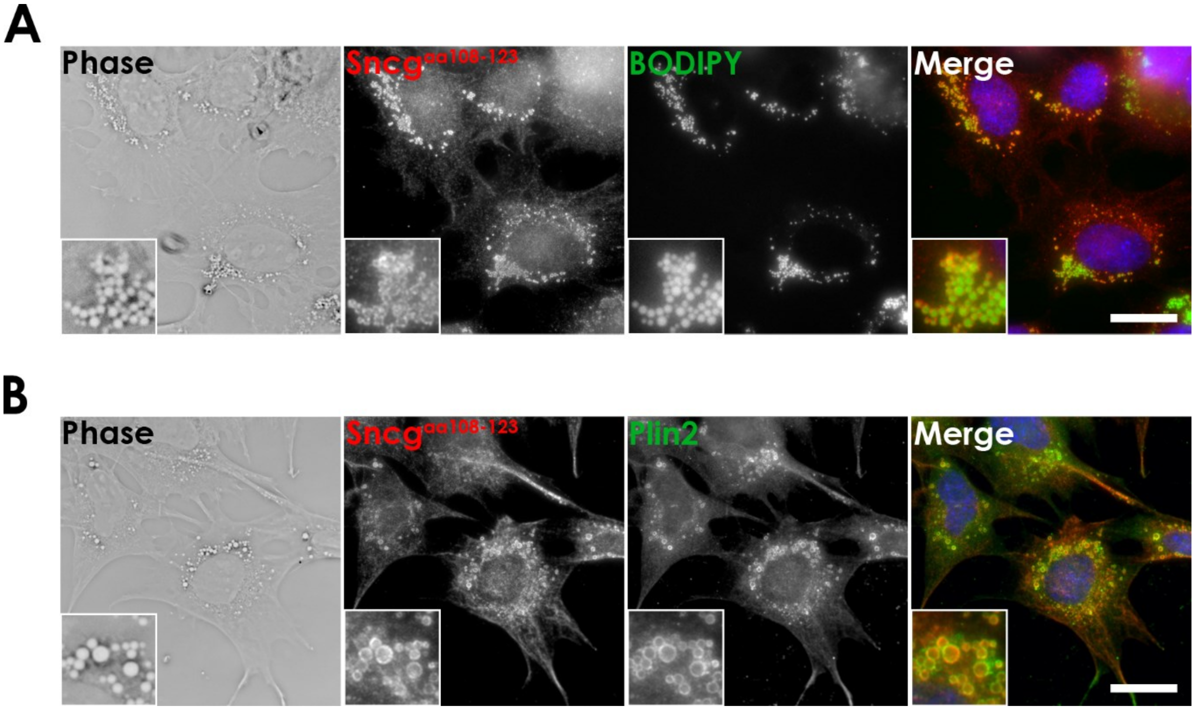

Figure AppA.1. Sncg localized to lipid droplets in 661W cells. A. Sncg$^{aa108-123}$ antibody (red) labeled phase-dense (inverted image) and Bodipy-positive (green) lipid droplets. Sncg appeared punctate on the surface of lipid droplets. **B.** Sncg (red) colocalized with Plin2 (green) on lipid droplets. Larger lipid droplets had smoother Sncg labeling than the smaller lipid droplets in A. (Scale bar: A, B: 70µm.)

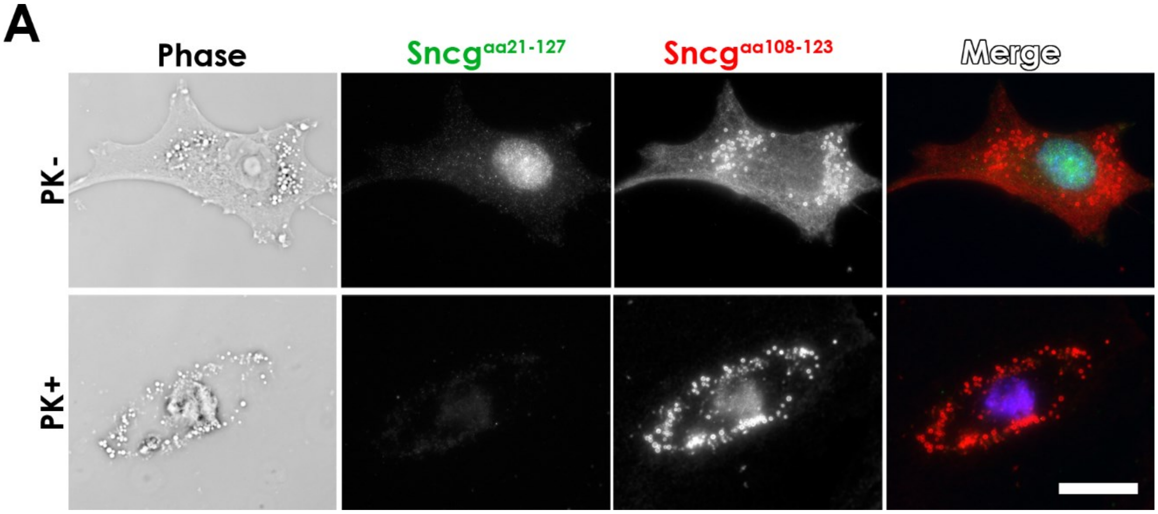

Figure AppA.2. Epitope reactive against Sncg$^{aa108-123}$ antibody is PK-resistant and lipid droplet-specific in 661W cells. A. Cells labeled with antibodies against different regions of Sncg. Sncg$^{aa21-127}$ (green) localized to the nucleus and had diffuse cytosolic labeling. After treatment with PK, Sncg$^{aa21-127}$ labeling was abolished. Sncg$^{aa108-123}$ (red) had diffuse cytosolic labeling and labeled lipid droplets. Diffuse cytosolic labeling was less apparent after PK treatment, but lipid droplet-associated labeling remained strong. (Scale bar: 70μm.)

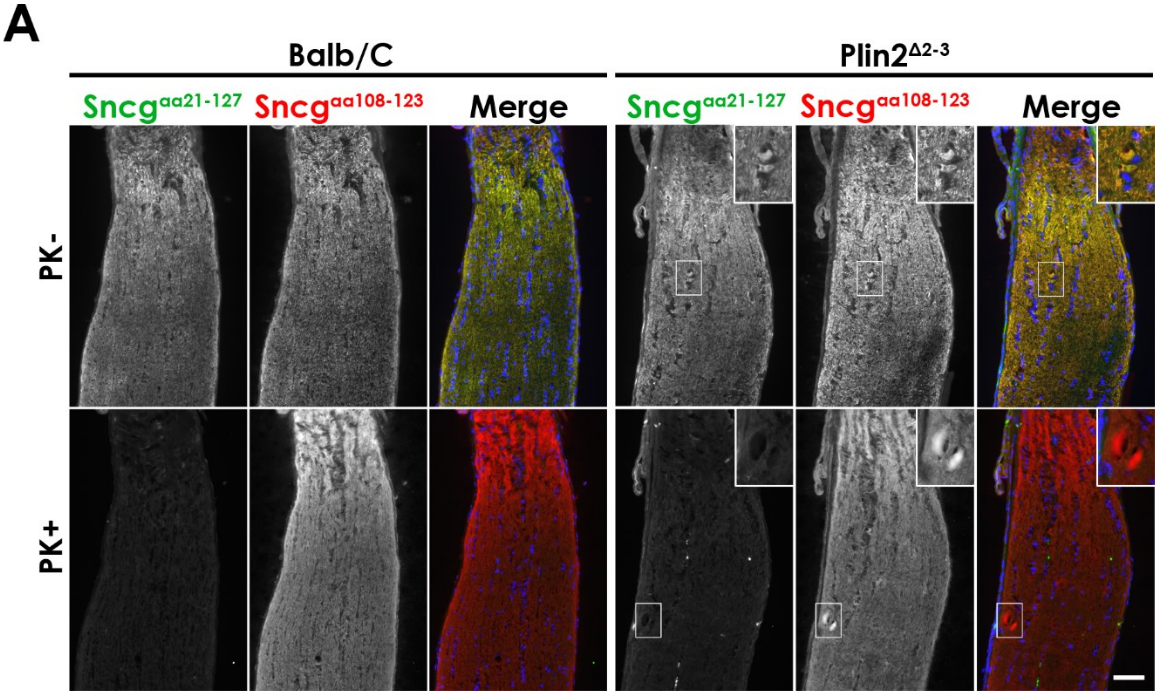

Figure AppA.3. PK-resistant Sncg structures in 12-mo-old Plin2$^{\Delta 2\text{-}3}$ ONH. A. Both Sncg antibodies labeled axons in the ONH. In aged Plin2$^{\Delta 2\text{-}3}$ ONH after PK treatment, Sncg structures were selectively detected by Sncg$^{aa108\text{-}123}$ (red). (Scale bar: 70µm.)

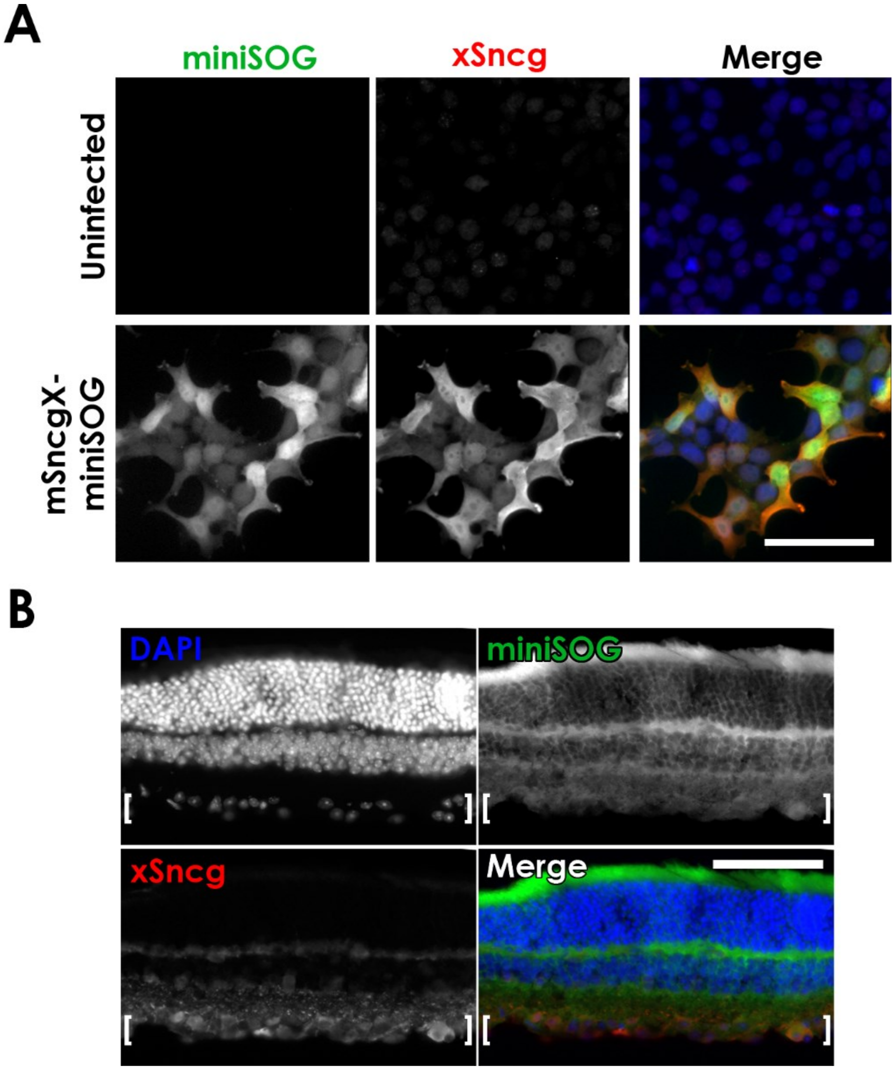

Figure AppA.4. Viral expression of mSncgx-miniSOG in 293 cells and mouse retina. **A.** Intrinsic fluorescence of miniSOG (green) colocalized with antibody directed against C-terminus of xSncg (red) in infected cells. **B.** Intravitreal injection of virus into 3-mo-old Balb/C. Expression of miniSOG (green) and xSncg (red) in RGCs (brackets) 3 days post injection. Labeling of miniSOG outside the RGC layer was most likely autofluorescence. (Scale bars: A, B: 70µm.)

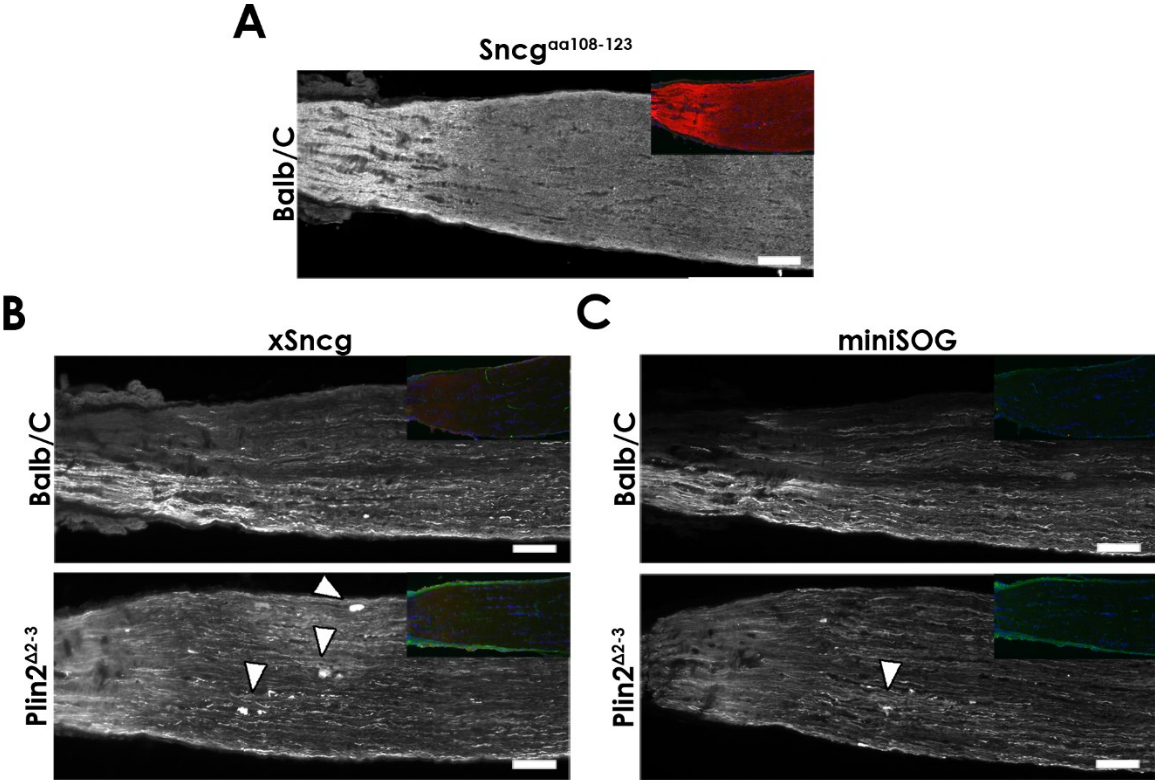

Figure AppA.5. Sncg structures in the optic nerve are axon swellings. A, B, C. PK-treated optic nerve from Balb/C or Plin2$^{\Delta 2\text{-}3}$. **A.** Sncg$^{aa108\text{-}123}$ labeled axons in the optic nerve. **B, C.** Viral expression labeled by antibodies against xSncg (B) or miniSOG (C). Structures were labeled in Plin2$^{\Delta 2\text{-}3}$ mice (white arrowheads), demonstrating that Sncg structures were axons continuous with RGCs at the time of infection. *Insets*, merged color files of uninfected optic nerves labeled with Sncg$^{aa108\text{-}123}$ (A), xSncg (B), or miniSOG (C) (all in red); PK-sensitive Sncg$^{aa21\text{-}127}$ (green); and DAPI (blue). (Scale bars: A, B, C: 70µm.)

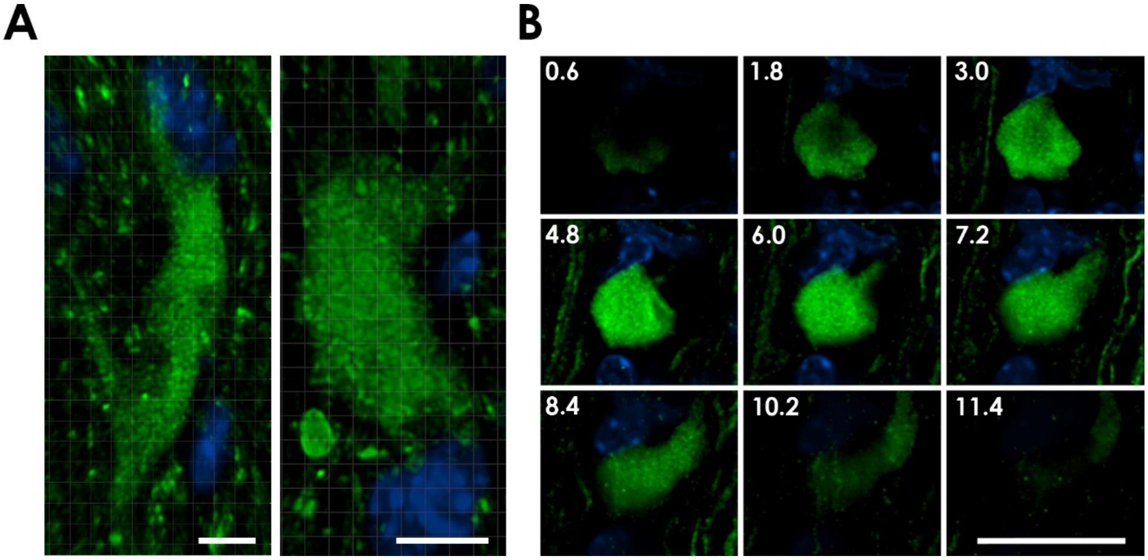

Figure AppA.6. Sncg has granular appearance within axon swellings. A. Two axon swellings from same optic nerve labeled with endogenous Sncg ($\text{Sncg}^{\text{aa108-123}}$). Sncg appeared punctate throughout the cytoplasm. **B.** AAV-mSncgx-miniSOG infected axons and axon swelling labeled with an antibody against the xSncg epitope. Punctate, round, and ovoid-shaped structures were in the cytoplasm. Numbers refer to position in microns of Z-stack. (Scale bars: A: 5µm; B: 7µm, C: 20µm.)

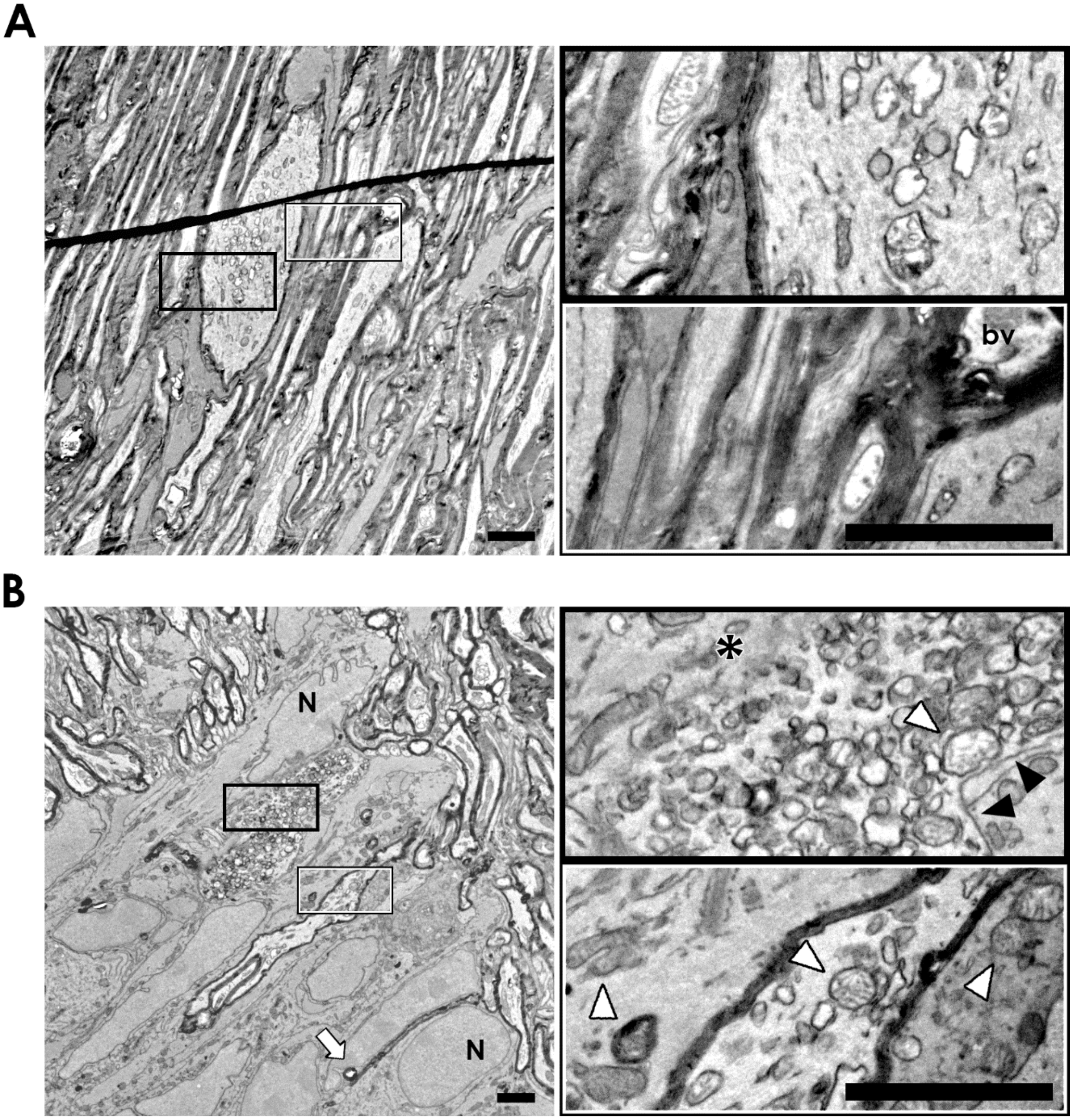

Figure AppA.7. Granular and vesicular materials in axon swellings seen by TEM. A, B. Osmiophilic myelin sheaths had regular periodicity around axons. Most axon swellings were myelinated, and contained low (A) and high (B) densities of granular material and organelles. **B.** Region of ONH closer to MTZ. A swelling with a high density of material (thick black border) had a thin membrane (black arrowheads) along one side of swelling. There did not appear to be a membrane separating the axon from the adjacent astrocyte on the other side of the swelling (asterisk). A myelinated axon was oriented in an orthogonal direction to the remaining axons (thin black box). This axon was not as swollen as other axons, but contents of axoplasm were suggestive of an axon swelling. Arrow points to a thin myelinated axon protrusion with a round, myelinated figure at the tip. White arrowheads = mitochondria; N = nucleus; bv = blood vessel. (Scale bars: A, B: 2µm)

Experimental Materials and Methods

Portions of this methods section were taken verbatim from the previously published methods section in Nguyen et al., 2011 [11].

Animals. C57Bl/6J, Balb/C, DBA/2J (D2), and DBA/2J-Gpnmb^{+}/Sj (D2-Gpnmb^{+}) [30] (Jackson Laboratory); CD-1 (Charles River); C57Bl/6J Sncg$^{-/-}$ from V.L. Buchman, [176]; C57Bl/6J-Sncg$^{+/-}$ were bred from C57Bl/6J Sncg$^{-/-}$; GLT-1-eGFP from J.D. Rothstein [299]; Balb/C-Plin2$^{\Delta 2\text{-}3}$ from K. Palczewski [298]. Mice were bred and maintained at the Johns Hopkins University Research Animal Resources facility on a 14hr/10hr light/dark cycle and fed *ad libitum.* Experiments used a combination of male and female mice, age-matched and sex-matched to control strains excluding SBEM studies. In SBEM studies, D2 mice were female and D2-Gpnmb^{+} was male. All experiments were in accordance with the Association for Research in Vision and Ophthalmology statement for use of animals in research with protocols approved by the Institute for Animal Care and Use Committee at the Johns Hopkins University School of Medicine.

Translimbal laser photocoagulation. IOP was elevated unilaterally [45; 49] in 5- to 9-mo-old C57Bl/6J Sncg$^{-/-}$ and Sncg$^{+/-}$ mice in groups matched for sex and age (7.6 and 7.5 mos, respectively) and in 3- to 7-mo-old Balb/C and Adrp$^{\Delta 2\text{-}3}$ mice in groups matched for sex and age. Burns were delivered directly behind the perilimbal plexus vessels and along the episcleral veins all around the limbus. IOP was measured with a rebound tonometer (TonoLab; Colonial Medical Supply).

Only mice with peak pressures greater than 25mm Hg were included in the study of $Sncg^{-/-}$ and $Sncg^{+/-}$ mice.

Optic nerve crush. Intraorbital crush to the optic nerve were delivered approximately 2 mm posterior to the globe for approximately 2 seconds using curved cross-action forceps (no. 7; Dumont), essentially as described [300].

Tissue preparation. Mice were asphyxiated with CO_2, transcardially perfused with phosphate-buffered saline, pH 7.4 (PBS), followed by 4% paraformaldehyde (PFA). Ocular tissues were fixed overnight in 4% PFA. Wholemount retinas were stored in 100% methanol. Optic nerves were saturated overnight with 30% sucrose in PBS, then set into blocks using Optimal Cutting Temperature (Tissue-Tek), and frozen.

***In situ* hybridization.** Wholemount retinas were processed for *in situ* hybridization using digoxigenin-labeled riboprobes for Sncg transcribed from cDNA (IMAGE clone 1448798; OpenBiosystems). Probes were hydrolyzed and detected using Cy3 tyramides (Perkin-Elmer), as previously described [10].

Immunochemistry. Antibodies used were $Sncg^{aa108\text{-}123}$ (Covance); $Sncg^{aa21\text{-}127}$ (Genetex); GFAP (Sigma-Aldrich, Dako, and Synaptic Systems); QD-9 and β-actin (Abcam); pNF (SMI31, Covance); Plin2 (Progen Biotechnik); MBP, GalC, cathepsin D (Millipore); Lgals3 (ATCC); Iba1 (Wako); LAMP1 and LAMP2 (Developmental Studies Hybridoma Bank); cathepsin K (Santa Cruz Biotechnology, Inc.); catalase (Binding Site); PMP70 and Pex14 (from Stephen Gould, Johns Hopkins University School of Medicine, Baltimore, MD via Paul

Watkins, Hugo W. Moser Research Institute at Kennedy Krieger, Baltimore, MD).

Secondary antibodies used were anti- mouse AlexaFluor 488, mouse Cy3, rabbit AlexaFluor 488, rat Cy5, rat AlexaFluor 488, and guinea pig AlexaFluor 488 (Invitrogen); anti- mouse Cy5, rabbit Cy3, rabbit Cy5, rat Cy3, guinea pig Cy3, and guinea pig Cy5 (Jackson ImmunoResearch Laboratories).

The standard labeling protocol of cells or tissue was permeabilization with 0.1% Triton-X 100 in PBS (PBS-T) for 10min, blocked with 10% normal goat serum (NGS) diluted in PBT for a minimum of 30min, incubation with primary antibody diluted in 5% NGS/PBT for 1hr to overnight, washed 3 times with PBT for a minimum of 5min each, incubation with secondary antibody in 5% NGS/PBT for 45min, washed 3 times with PBT for a minimum of 5min each, counterstained with DAPI diluted in PBS for 10min, washed 3 times with PBS for a minimum of 5min each, then mounted using Aqua-Poly/Mount (PolySciences, Inc.).

PK-resistant Sncg was detected by treating sections or cells with 25 μg/mL PK for 5 min before incubation with the primary antibody. Nuclei were detected by 4',6-diamidino-2-phenylindole (DAPI) in Tris-EDTA, pH 8 used at 20μg/μL.

Lipid dyes. ORO was prepared as 1% solution dissolved in propylene glycol using a protocol modified from a previous study [246]. Cells were washed with 100% propylene glycol, incubated with 1% ORO for 1 hr, then washed with 85% and 50% propylene glycol for 2 min each. ORO and Plin2 labeled samples were mounted in 90% glycerol containing 100mM Tris, pH8.7 and 1mg/mL pphenylenediamine. BODIPY 493/503 (Molecular Probes) was prepared in PBS and used at 0.1mg/mL for 10 min.

Cell culture. 661W cells were obtained from N. Agarwal (University of North Texas Health Science Center, Fort Worth, TX). Sequencing of the Thy1 gene confirmed that they were of mouse origin, as reported [288; 289]. Cells were cultured in high glucose Dulbecco's Modified Eagle Medium (DMEM-HG) containing 10% fetal bovine serum, 100U/mL penicillin and 100ug/mL streptomycin, and 2mM glutamine.

Cells were transfected with GFP fusion constructs containing the full-length mouse Sncg (pCS2-GFP-Sncg) or mouse Sncg lacking the last 15 aa in the C-terminus (pCS2-GFP-SncgΔC) using Lipofectamine 2000 (Invitrogen) and fixed with 4% paraformaldehyde (PFA) before immunostaining.

Primary astrocytes were cultured using a protocol modified from a published protocol [301], with guidance from L. Foo and B. Barres (personal communication). Cerebral cortices from neonatal p0-p3 CD-1 and Balb/C mice were dissociated using papain and 625U DNase (both Worthington Biochemicals), washed and triturated using a solution containing 1.5mg/mL ovomucoid trypsin inhibitor (Worthington Biochemicals), 1.5mg/mL bovine serum albumin (Sigma-Aldrich), and 1250U DNase (Ovo-BSA). After pelleting, cells were resuspended in 2X Ovo-BSA with 437U DNase and centrifuged again. Cells were passed through 40µm cell strainer and plated at approximately 260,000 cells/cm^2 on poly-L-lysine-coated flasks in DMEM-HG containing 10% fetal bovine serum, 100U/mL pencillin and 100µg/mL streptomycin, 2mM glutamine, 5µg/mL insulin, 10µM hydrocortisone, and 5µg/mL N-acetyl-L-cysteine (ACM). After cells reached confluency, they were washed with Dulbecco's PBS (D-PBS) and shaken vigorously by hand to remove overlying oligodendrocytes. Cells were allowed to recover for two days before adding 10µM Cytosine β-D-arabinofuranoside (AraC) to remove microglia. Cells were fed regularly with ACM + AraC until visual homogeneity. Purity was assessed by estimating the percent of GFAP^{+} (≥ 75%) and Iba1^{+} (≤ 1%) cells.

Myelin and oleic acid feeding. Myelin was prepared from frozen bovine optic nerves with procedures modified from a previous protocol [302]. Nerves were de-sheathed and minced before homogenization in 8 volumes of 0.33M sucrose on ice. Homogenates were layered over cold 0.66M sucrose, and myelin was recovered at the sucrose interface after 1 hr at 68,400 x g. After dilution with 1 volume distilled water and repeat ultracentrifugation, myelin was washed three times by dilution with 2.6 volumes distilled water and pelleted at 68,400 x g before it was finally resuspended at 2-5mg/mL in distilled water, aliquoted, and stored at -20°C.

For astrocyte feeding experiments, cells were seeded at 20,000 cells per Matrigel-coated (1:500 dilution in D-PBS) 8mm glass coverslips placed in a 48-well plate. After a minimum of 30hrs in culture, 3µg of myelin diluted in 20mM HEPES-supplemented ACM (ACM-HEPES) was added to each well and the plate was centrifuged at 500 x g for 3 min. Bovine serum albumin-conjugated oleic acid (Sigma-Aldrich) was used at varying concentrations diluted in ACM-HEPES.

To differentiate myelin on the surface of cells from myelin that was internalized, myelin antibodies were used before and after membrane permeabilization using a 0.5% Triton-X 100 for 10min. For quantification, the area of the signal obtained from myelin debris outside of cell membranes was subtracted from post-permeabilized myelin signal. The remaining signal intensity was quantified (referred to as Internal myelin).

To prepare samples for western blot, 200,000 cells were seeded onto Matrigel-coated 6-well plates or 35mm dishes. Thirty micrograms of myelin was added to each well and centrifuged at 500 x g for 5 min. At the appropriate time point, astrocytes were washed 3-5 times with D-PBS and then fixed with 4% PFA or lysed with RIPA buffer supplemented with EDTA-free protease inhibitor cocktail (Roche) (RIPA+PI), depending on experiment; otherwise cells were re-incubated with HEPES-ACM.

Image acquisition and analysis. Immunofluorescence, phase, and differential interference contrast images were acquired using Zeiss 200 M inverted fluorescent microscope and CoolSnap camera. IPlab imaging software (Becton Dickinson) was used for acquisitions and analyses.

Optic nerve tissue. Multiple sections were quantified for each optic nerve. Instead of selecting one segmentation (threshold) level for quantifications, fifty fluorescent measures were obtained, as previously done [303]. The fluorescence at each segment was averaged for each optic nerve. The mean fluorescence of optic nerves were then averaged for each genotype or experimental condition. A two-tailed, Student's t-test was calculated between 2 groups across SV. The SV that met a particular statistical significance level was then analyzed to determine fold-changes between the groups. The mean of the fold-changes was identified and reported. Analysis of data performed using Excel (Microsoft) and GraphPad Prism (GraphPad Software).

To measure fluorescence of a marker (Lgals3 or Plin2) within a particular cell type (GFAP- or Lgals3-expressing astrocytes or Iba1-expressing microglia), an image mask was created from the astrocyte or microglia image according to SV. The segmented fluorescence of Lgals3 or Plin2 was measured within each new image mask made from increasing SV of the astrocyte or microglia.

Cultured astrocytes. Data collected from all astrocyte immunofluorescence experiments were obtained by imaging 9 fields of view from each of quadruplicate samples. Each field was individually curated for autofluorescence and other artifacts, with a minimum of 3 images used to quantify each experimental condition. Each experiment was performed in triplicate and the data presented are the means of those replicates.

A 5µm (in cultured astrocytes) or 10µm (for optic nerves) rolling-ball background subtraction (IPlab) was used to enhance lipid droplet images before automated quantification.

Western blotting. Lysates were briefly sonicated before protein quantification using Pierce 660nm Protein Assay (Thermo-Scientific). Fifty micrograms of protein were denatured using sodium dodecyl sulfate (SDS) sample buffer (50mM Tris-HCl, pH6.8, 2% SDS, 10% glycerol, 100mM β-mercaptoethanol, 0.1% bromophenol blue) and heat before loading onto precast 4-15% polyacrylamide

Mini Protean TGX Tris-glycine gels (Bio-Rad). Electrophoresis was performed at 75-100V in Towbin buffer (25mM Tris, 192mM glycine) with 0.1% SDS. Proteins were transferred onto nitrocellulose membranes (0.45µm pore, Whatman) at 100V for 1 hr in Towbin buffer with 10% methanol, then incubated for a minimum of 30min in Odyssey blocking buffer (LI-COR), primary antibodies overnight in Tris-buffered saline containing 0.1% Tween-20 (TBT), then infrared secondary antibodies (anti-guinea pig IRDye800CW, anti-rabbit IRDye800CW (LI-COR); anti-mouse AlexaFluor 680 (Invitrogen); anti-rat DyLight 800 (Thermo-Fisher)) in TBT for 1hr after washes in TBT. Membranes were imaged using a Licor scanner. Membranes were reprobed for additional secondary antibodies, or stripped using 0.1M glycine, pH 2 or OneMinute Plus Western Blot stripping buffer (GM Biosciences) before additional labeling with primary and secondary antibodies. Protein bands quantified using ImageJ by selecting each lane using the Rectangular tool and plotting the selection [304]. The area under the relevant peak was selected by drawing a straight line from valley to valley flanking the peak and then quantified. All experiments were performed in triplicate. Normalization performed with actin. Protein-to-actin ratio reported for cell culture experiments. The mean protein-to-actin ratio of D2-Gpnmb$^+$ ONH was calculated and each protein-to-actin ratio was then normalized to that mean.

MTT assay. Astrocytes were plated in a 96-well plate at 5000 cells/well. Myelin was added as described above. After 24 hrs, myelin was washed out and cells incubated for 4 days. MTT was added to cells for 1 hr. Acidified 20% SDS was added and left overnight to solubilize MTT. Absorbance was read at 570nm.

Electron microscopy. *Serial block-face scanning electron microscopy.* SBEM employs a microtome inside of a scanning EM as originally described by Leighton [305] and refined by Denk and Horstmann [306]. Optic nerves from 9-mo-old D2 were pre-screened for axonal degeneration using distal cross-sections labeled with Sncg and/or pNF to enable us to sample different disease stages. These mice, along with 9-mo-old D2-Gpnmb$^+$ and C57Bl/6J optic nerves were anesthetized with pentobarbital and transcardially perfused with Ringer solution followed by 2.5% glutaraldehyde/2% PFA in cacodylate buffer (Ted Pella) containing 2 mM $CaCl_2$ (CAC+Ca buffer). An eye was removed and the ONH carefully dissected and postfixed in the same fixative agent for 2 hrs at 4°C. The nerve was washed in CAC+Ca buffer for 30 min at 4°C. The nerve was placed in CAC+Ca buffer containing 2% OsO_4 and 1.5% potassium ferrocyanide for 3 hrs at room temperature (RT). The nerve was washed with ddH_2O 3 times for 5 min and then placed in 1% aqueous thiocarbohydrazide (Sigma-Aldrich) for 20 min at RT. The nerve was washed 3 times for 5 min in ddH_2O and then placed in 2% aqueous OsO_4 for 1 hr at RT. The nerve was washed three times for 5 min and placed in 1% aqueous uranyl acetate at 4 °C overnight. The nerve was washed three times for 5 min in ddH_2O and incubated in lead aspartate solution in a 60°C oven for 30 min, as described previously [307]. The nerve was washed 3 times for 5 min in ddH_2O and then dehydrated in a series of ice-cold ethanol solutions (20%, 50%, 70%, 90%, 100%, 100%) followed by ice-cold anhydrous acetone for 10 min. The nerve was placed in acetone at RT for 10 min and then infiltrated with an ascending series of Durcupan:acetone solutions. The nerve was infiltrated with 100% Durcupan and then cured at 60°C for 2 days. The nerve was trimmed to remove excess plastic and attached to an aluminum pin, grounded with silver paint, and sputter coated with gold–palladium before imaging.

Specimens were imaged on a Quanta SEM (FEI) equipped with a 3View serial block-face system (Gatan). Specimens imaged at high vacuum with 2.5-kV beam current and 70-nm sectioning thickness. A 2D montage was collected at each Z plane to increase field of view. Volumes were stitched and analyzed by using IMOD (http://bio3d.colorado.edu/imod/) [308].

Estimates of spherical electron-dense structures (i.e., lipid droplets) within astrocytes were obtained using Imaris (BitPlane). For this, 25.4mm^3 subvolumes were extracted from larger volumes using IMOD and then imported into Imaris software for thresholding-based identification and quantification. Images were inverted and the Surfaces tool was applied to select objects. After local background subtraction of 500nm, object filters for intensity (within 75% of maximum), voxel size (excluding objects smaller than 30nm diameter), and sphericity (excluding sphericity lower than 0.75) thresholds were set. These parameters were selected based on a smaller subvolume in the D2 (mild) MTZ and then applied uniformly to all other samples. The creation of a mask made from the Surfaces objects allowed manual review of the data which showed that D2 nerves were undercounted more severely than D2-Gpnmb$^+$ due to many objects being in close proximity to each other.

Transmission electron microscopy. Astrocytes that were fed myelin were analyzed by TEM with procedures modified from a previous study [309]. Astrocytes were fixed for 1 hr in 2.5% glutaraldehyde/2% PFA in 0.1M sodium cacodylate buffer, pH 7.4 (all from Electron Microscopy Sciences) with 2mM calcium chloride (Sigma-Aldrich) on ice. Cells were post-fixed with ferrocyanide-reduced osmium tetroxide (1.5% potassium ferrocyanide (Sigma-Aldrich)/2% osmium tetroxide (Electron Microscopy Sciences) in H_2O), stained with 1% thiocarbohydrazide (Polysciences, Inc.) followed by 2% osmium tetroxide. Cells were subsequently stained with 1% uranyl acetate (Electron Microscopy Sciences) before progressive dehydration into ethanol. Durcupan-embedded cells were hardened for 36-48 hrs at 60-65°C. 60nm-thick sections were imaged using H7600 transmission electron microscope (Hitachi).

Generation of and infection with AAV2-mSncgXt-mS. Chimera of mouse aa 1-110 and *Xenopus tropicalis* aa 117-130 with a C-terminal miniSOG tag was cloned into a AAV2.CB7. CI vector. Virus was generated by University of Pennsylvania Vector Core. Mice were anesthetized with Avertin and unilaterally injected intravitreally with 2μL of 1.78 x 10^{12} genome copies/mL per eye.

References

1. Quigley HA & Broman AT. 2006. The number of people with glaucoma worldwide in 2010 and 2020. Br. J. Ophthalmol. 90: 262-267.

2. Comparison of glaucomatous progression between untreated patients with normal-tension glaucoma and patients with therapeutically reduced intraocular pressures. Collaborative Normal-Tension Glaucoma Study Group. 1998. Am. J. Ophthalmol. 126: 487-497.

3. Fujita Y, Imagawa T & Uehara M. 2000. Comparative study of the lamina cribrosa and the pial septa in the vertebrate optic nerve and their relationship to the myelinated axons. Tissue Cell. 32: 293-301.

4. Wirtschafter JD. 1983. Optic nerve axons and acquired alterations in the appearance of the optic disc. Trans. Am. Ophthalmol. Soc. 81: 1034-1091.

5. Quigley HA & Addicks EM. 1981. Regional differences in the structure of the lamina cribrosa and their relation to glaucomatous optic nerve damage. Arch. Ophthalmol. 99: 137-143.

6. Quigley HA, Addicks EM & Green WR. 1982. Optic nerve damage in human glaucoma. III. Quantitative correlation of nerve fiber loss and visual field defect in glaucoma, ischemic neuropathy, papilledema, and toxic neuropathy. Arch. Ophthalmol. 100: 135-146.

7. Quigley HA & Green WR. 1979. The histology of human glaucoma cupping and optic nerve damage: clinicopathologic correlation in 21 eyes. Ophthalmology. 86: 1803-1830.

8. Schlamp CL, Li Y, Dietz JA, Janssen KT & Nickells RW. 2006. Progressive ganglion cell loss and optic nerve degeneration in DBA/2J mice is variable and asymmetric. BMC Neurosci. 7: 66.

9. Jakobs TC, Libby RT, Ben Y, John SWM & Masland RH. 2005. Retinal ganglion cell degeneration is topological but not cell type specific in DBA/2J mice. The Journal of Cell Biology. 171: 313-325.

10. Soto I, Oglesby E, Buckingham BP, Son JL, Roberson ED, Steele MR, Inman DM, Vetter ML, Horner PJ & Marsh-Armstrong N. 2008. Retinal ganglion cells downregulate gene expression and lose their axons within the optic nerve head in a mouse glaucoma model. J. Neurosci. 28: 548-561.

11. Nguyen JV, Soto I, Kim K, Bushong EA, Oglesby E, Valiente-Soriano FJ, Yang Z, Davis CO, Bedont JL, Son JL, Wei JO, Buchman VL, Zack DJ, Vidal-Sanz M, Ellisman

MH & Marsh-Armstrong N. 2011. Myelination transition zone astrocytes are constitutively phagocytic and have synuclein dependent reactivity in glaucoma. Proc. Natl. Acad. Sci. U. S. A. 108: 1176.

12. Howell GR, Libby RT, Jakobs TC, Smith RS, Phalan FC, Barter JW, Barbay JM, Marchant JK, Mahesh N, Porciatti V, Whitmore AV, Masland RH & John SW. 2007. Axons of retinal ganglion cells are insulted in the optic nerve early in DBA/2J glaucoma. J. Cell Biol. 179: 1523-1537.

13. Minckler DS. 1980. The organization of nerve fiber bundles in the primate optic nerve head. Arch. Ophthalmol. 98: 1630-1636.

14. Radius RL & Anderson DR. 1979. The course of axons through the retina and optic nerve head. Arch. Ophthalmol. 97: 1154-1158.

15. Sun D, Lye-Barthel M, Masland RH & Jakobs TC. 2009. The morphology and spatial arrangement of astrocytes in the optic nerve head of the mouse. J. Comp. Neurol. 516: 1-19.

16. May CA & Lutjen-Drecoll E. 2002. Morphology of the murine optic nerve. Invest. Ophthalmol. Vis. Sci. 43: 2206-2212.

17. Magoon EH & Robb RM. 1981. Development of myelin in human optic nerve and tract. A light and electron microscopic study. Arch. Ophthalmol. 99: 655-659.

18. Hildebrand C, Remahl S & Waxman SG. 1985. Axo-glial relations in the retina-optic nerve junction of the adult rat: electron-microscopic observations. J. Neurocytol. 14: 597-617.

19. Black JA, Waxman SG & Hildebrand C. 1985. Axo-glial relations in the retina-optic nerve junction of the adult rat: freeze-fracture observations on axon membrane structure. J. Neurocytol. 14: 887-907.

20. Bouhenni RA, Dunmire J, Sewell A & Edward DP. 2012. Animal models of glaucoma. J. Biomed. Biotechnol. 2012: 692609.

21. Aihara M, Lindsey JD & Weinreb RN. 2003. Aqueous humor dynamics in mice. Invest. Ophthalmol. Vis. Sci. 44: 5168-5173.

22. Smith RS, Zabaleta A, Savinova OV & John SW. 2001. The mouse anterior chamber angle and trabecular meshwork develop without cell death. BMC Dev. Biol. 1: 3.

23. Johansson JO. 1987. The lamina cribrosa in the eyes of rats, hamsters, gerbils and guinea pigs. Acta Anat. (Basel). 128: 55-62.

24. John SW, Smith RS, Savinova OV, Hawes NL, Chang B, Turnbull D, Davisson M, Roderick TH & Heckenlively JR. 1998. Essential iris atrophy, pigment dispersion, and glaucoma in DBA/2J mice. Invest. Ophthalmol. Vis. Sci. 39: 951-962.

25. Chang B, Smith RS, Hawes NL, Anderson MG, Zabaleta A, Savinova O, Roderick TH, Heckenlively JR, Davisson MT & John SW. 1999. Interacting loci cause severe iris atrophy and glaucoma in DBA/2J mice. Nat. Genet. 21: 405-409.

26. Anderson MG, Smith RS, Hawes NL, Zabaleta A, Chang B, Wiggs JL & John SW. 2002. Mutations in genes encoding melanosomal proteins cause pigmentary glaucoma in DBA/2J mice. Nat. Genet. 30: 81-85.

27. Libby RT, Anderson MG, Pang IH, Robinson ZH, Savinova OV, Cosma IM, Snow A, Wilson LA, Smith RS, Clark AF & John SW. 2005. Inherited glaucoma in DBA/2J mice: pertinent disease features for studying the neurodegeneration. Vis. Neurosci. 22: 637-648.

28. Johnson R & Jackson IJ. 1992. Light is a dominant mouse mutation resulting in premature cell death. Nat. Genet. 1: 226-229.

29. Anderson MG, Smith RS, Hawes NL, Zabaleta A, Chang B, Wiggs JL & John SW. 2002. Mutations in genes encoding melanosomal proteins cause pigmentary glaucoma in DBA/2J mice. Nat. Genet. 30: 81-85.

30. Howell GR, Libby RT, Marchant JK, Wilson LA, Cosma IM, Smith RS, Anderson MG & John SW. 2007. Absence of glaucoma in DBA/2J mice homozygous for wild-type versions of Gpnmb and Tyrp1. BMC Genet. 8: 45.

31. Kerrigan LA, Zack DJ, Quigley HA, Smith SD & Pease ME. 1997. TUNEL-positive ganglion cells in human primary open-angle glaucoma. Arch. Ophthalmol. 115: 1031-1035.

32. Tatton NA, Tezel G, Insolia SA, Nandor SA, Edward PD & Wax MB. 2001. In situ detection of apoptosis in normal pressure glaucoma. a preliminary examination. Surv. Ophthalmol. 45 Suppl 3: S268-72; discussion S273-6.

33. Osborne NN, Wood JP, Chidlow G, Bae JH, Melena J & Nash MS. 1999. Ganglion cell death in glaucoma: what do we really know? Br. J. Ophthalmol. 83: 980-986.

34. Elmore S. 2007. Apoptosis: a review of programmed cell death. Toxicol. Pathol. 35: 495-516.

35. Finucane DM, Bossy-Wetzel E, Waterhouse NJ, Cotter TG & Green DR. 1999. Bax-induced caspase activation and apoptosis via cytochrome c release from mitochondria is inhibitable by Bcl-xL. J. Biol. Chem. 274: 2225-2233.

36. Jurgensmeier JM, Xie Z, Deveraux Q, Ellerby L, Bredesen D & Reed JC. 1998. Bax directly induces release of cytochrome c from isolated mitochondria. Proc. Natl. Acad. Sci. U. S. A. 95: 4997-5002.

37. Libby RT, Li Y, Savinova OV, Barter J, Smith RS, Nickells RW & John SW. 2005. Susceptibility to neurodegeneration in a glaucoma is modified by Bax gene dosage. PLoS Genet. 1: 17-26.

38. Li Y, Schlamp CL, Poulsen KP & Nickells RW. 2000. Bax-dependent and independent pathways of retinal ganglion cell death induced by different damaging stimuli. Exp. Eye Res. 71: 209-213.

39. Isenmann S, Engel S, Gillardon F & Bahr M. 1999. Bax antisense oligonucleotides reduce axotomy-induced retinal ganglion cell death in vivo by reduction of Bax protein expression. Cell Death Differ. 6: 673-682.

40. Qin Q, Patil K & Sharma SC. 2004. The role of Bax-inhibiting peptide in retinal ganglion cell apoptosis after optic nerve transection. Neurosci. Lett. 372: 17-21.

41. Stoll G, Jander S & Myers RR. 2002. Degeneration and regeneration of the peripheral nervous system: from Augustus Waller's observations to neuroinflammation. J. Peripher. Nerv. Syst. 7: 13-27.

42. Coleman MP & Freeman MR. 2010. Wallerian degeneration, wld(s), and nmnat. Annu. Rev. Neurosci. 33: 245-267.

43. McKinnon SJ, Schlamp CL & Nickells RW. 2009. Mouse models of retinal ganglion cell death and glaucoma. Exp. Eye Res. 88: 816-824.

44. Quigley HA & Hohman RM. 1983. Laser energy levels for trabecular meshwork damage in the primate eye. Invest. Ophthalmol. Vis. Sci. 24: 1305-1307.

45. Levkovitch-Verbin H, Quigley HA, Martin KR, Valenta D, Baumrind LA & Pease ME. 2002. Translimbal laser photocoagulation to the trabecular meshwork as a model of glaucoma in rats. Invest. Ophthalmol. Vis. Sci. 43: 402-410.

46. Soto I, Pease ME, Son JL, Shi X, Quigley HA & Marsh-Armstrong N. 2011. Retinal Ganglion Cell Loss in a Rat Ocular Hypertension Model Is Sectorial and Involves Early Optic Nerve Axon Loss. Investigative Ophthalmology & Visual Science. 52: 434-441.

47. Fu CT & Sretavan D. 2010. Laser-induced ocular hypertension in albino CD-1 mice. Invest. Ophthalmol. Vis. Sci. 51: 980-990.

48. Aihara M, Lindsey JD & Weinreb RN. 2003. Experimental mouse ocular hypertension: establishment of the model. Invest. Ophthalmol. Vis. Sci. 44: 4314-4320.

49. Salinas-Navarro M, Alarcon-Martinez L, Valiente-Soriano FJ, Ortin-Martinez A, Jimenez-Lopez M, Aviles-Trigueros M, Villegas-Perez MP, de la Villa P & Vidal-Sanz M. 2009. Functional and morphological effects of laser-induced ocular hypertension in retinas of adult albino Swiss mice. Mol. Vis. 15: 2578-2598.

50. Gross RL, Ji J, Chang P, Pennesi ME, Yang Z, Zhang J & Wu SM. 2003. A mouse model of elevated intraocular pressure: retina and optic nerve findings. Trans. Am. Ophthalmol. Soc. 101: 163-9; discussion 169-71.

51. Grozdanic SD, Betts DM, Sakaguchi DS, Allbaugh RA, Kwon YH & Kardon RH. 2003. Laser-induced mouse model of chronic ocular hypertension. Invest. Ophthalmol. Vis. Sci. 44: 4337-4346.

52. Ji J, Chang P, Pennesi ME, Yang Z, Zhang J, Li D, Wu SM & Gross RL. 2005. Effects of elevated intraocular pressure on mouse retinal ganglion cells. Vision Res. 45: 169-179.

53. Salinas-Navarro M, Alarcon-Martinez L, Valiente-Soriano FJ, Jimenez-Lopez M, Mayor-Torroglosa S, Aviles-Trigueros M, Villegas-Perez MP & Vidal-Sanz M. 2010. Ocular hypertension impairs optic nerve axonal transport leading to progressive retinal ganglion cell degeneration. Exp. Eye Res. 90: 168-183.

54. Johnson TV & Tomarev SI. 2010. Rodent models of glaucoma. Brain Res. Bull. 81: 349-358.

55. Templeton JP & Geisert EE. 2012. A practical approach to optic nerve crush in the mouse. Mol. Vis. 18: 2147-2152.

56. Levkovitch-Verbin H, Quigley HA, Martin KR, Zack DJ, Pease ME & Valenta DF. 2003. A model to study differences between primary and secondary degeneration of retinal ganglion cells in rats by partial optic nerve transection. Invest. Ophthalmol. Vis. Sci. 44: 3388-3393.

57. Lotery AJ. 2005. Glutamate excitotoxicity in glaucoma: truth or fiction? Eye (Lond). 19: 369-370.

58. Salt TE & Cordeiro MF. 2006. Glutamate excitotoxicity in glaucoma: throwing the baby out with the bathwater? Eye (Lond). 20: 730-1; author reply 731-2.

59. Fu CT & Sretavan DW. 2012. Ectopic vesicular glutamate release at the optic nerve head and axon loss in mouse experimental glaucoma. J. Neurosci. 32: 15859-15876.

60. Zhang Y & Barres BA. 2010. Astrocyte heterogeneity: an underappreciated topic in neurobiology. Curr. Opin. Neurobiol. 20: 588-594.

61. Molofsky AV, Krencik R, Ullian EM, Tsai HH, Deneen B, Richardson WD, Barres BA & Rowitch DH. 2012. Astrocytes and disease: a neurodevelopmental perspective. Genes Dev. 26: 891-907.

62. Hernandez MR, Miao H & Lukas T. 2008. Astrocytes in glaucomatous optic neuropathy. Prog. Brain Res. 173: 353-373.

63. Sofroniew MV & Vinters HV. 2010. Astrocytes: biology and pathology. Acta Neuropathol. 119: 7-35.

64. Clarke LE & Barres BA. 2013. Emerging roles of astrocytes in neural circuit development. Nat. Rev. Neurosci. 14: 311-321.

65. Butt AM, Pugh M, Hubbard P & James G. 2004. Functions of optic nerve glia: axoglial signalling in physiology and pathology. Eye (Lond). 18: 1110-1121.

66. Oberheim NA, Goldman SA & Nedergaard M. 2012. Heterogeneity of astrocytic form and function. Methods Mol. Biol. 814: 23-45.

67. Slezak M & Pfrieger FW. 2003. New roles for astrocytes: regulation of CNS synaptogenesis. Trends Neurosci. 26: 531-535.

68. Hernandez MR. 2000. The optic nerve head in glaucoma: role of astrocytes in tissue remodeling. Prog. Retin. Eye Res. 19: 297-321.

69. Ridet JL, Malhotra SK, Privat A & Gage FH. 1997. Reactive astrocytes: cellular and molecular cues to biological function. Trends Neurosci. 20: 570-577.

70. Morgan JE. 2000. Optic nerve head structure in glaucoma: astrocytes as mediators of axonal damage. Eye (Lond). 14 (Pt 3B): 437-444.

71. Eliasson C, Sahlgren C, Berthold CH, Stakeberg J, Celis JE, Betsholtz C, Eriksson JE & Pekny M. 1999. Intermediate filament protein partnership in astrocytes. J. Biol. Chem. 274: 23996-24006.

72. Schnitzer J, Franke WW & Schachner M. 1981. Immunocytochemical demonstration of vimentin in astrocytes and ependymal cells of developing and adult mouse nervous system. J. Cell Biol. 90: 435-447.

73. Janeczko K. 1993. Co-expression of GFAP and vimentin in astrocytes proliferating in response to injury in the mouse cerebral hemisphere. A combined autoradiographic and double immunocytochemical study. Int. J. Dev. Neurosci. 11: 139-147.

74. Perego C, Vanoni C, Bossi M, Massari S, Basudev H, Longhi R & Pietrini G. 2000. The GLT-1 and GLAST glutamate transporters are expressed on morphologically distinct

astrocytes and regulated by neuronal activity in primary hippocampal cocultures. J. Neurochem. 75: 1076-1084.

75. Cahoy JD, Emery B, Kaushal A, Foo LC, Zamanian JL, Christopherson KS, Xing Y, Lubischer JL, Krieg PA, Krupenko SA, Thompson WJ & Barres BA. 2008. A transcriptome database for astrocytes, neurons, and oligodendrocytes: a new resource for understanding brain development and function. J. Neurosci. 28: 264-278.

76. Cammer W. 1990. Glutamine synthetase in the central nervous system is not confined to astrocytes. J. Neuroimmunol. 26: 173-178.

77. Norenberg MD & Martinez-Hernandez A. 1979. Fine structural localization of glutamine synthetase in astrocytes of rat brain. Brain Res. 161: 303-310.

78. Ogata K & Kosaka T. 2002. Structural and quantitative analysis of astrocytes in the mouse hippocampus. Neuroscience. 113: 221-233.

79. Ghandour MS, Langley OK, Labourdette G, Vincendon G & Gombos G. 1981. Specific and artefactual cellular localizations of S 100 protein: an astrocyte marker in rat cerebellum. Dev. Neurosci. 4: 66-78.

80. Peters A, Palay SL & de F Webster H. 1976. The Fine Structure of the Nervous System: The Neurons and Supporting Cells. W. B. Saunders Co. Philadelphia.

81. Miller RH & Raff MC. 1984. Fibrous and protoplasmic astrocytes are biochemically and developmentally distinct. J. Neurosci. 4: 585-592.

82. Raff MC, Abney ER, Cohen J, Lindsay R & Noble M. 1983. Two types of astrocytes in cultures of developing rat white matter: differences in morphology, surface gangliosides, and growth characteristics. J. Neurosci. 3: 1289-1300.

83. Bushong EA, Martone ME, Jones YZ & Ellisman MH. 2002. Protoplasmic astrocytes in CA1 stratum radiatum occupy separate anatomical domains. J. Neurosci. 22: 183-192.

84. Butt AM, Colquhoun K, Tutton M & Berry M. 1994. Three-dimensional morphology of astrocytes and oligodendrocytes in the intact mouse optic nerve. J. Neurocytol. 23: 469-485.

85. Trivino A, Ramirez JM, Salazar JJ, Ramirez AI & Garcia-Sanchez J. 1996. Immunohistochemical study of human optic nerve head astroglia. Vision Res. 36: 2015-2028.

86. Quigley HA. 1977. Gap junctions between optic nerve head astrocytes. Invest. Ophthalmol. Vis. Sci. 16: 582-585.

87. Lee SH, Kim WT, Cornell-Bell AH & Sontheimer H. 1994. Astrocytes exhibit regional specificity in gap-junction coupling. Glia. 11: 315-325.

88. Giaume C & McCarthy KD. 1996. Control of gap-junctional communication in astrocytic networks. Trends Neurosci. 19: 319-325.

89. Butt AM, Duncan A & Berry M. 1994. Astrocyte associations with nodes of Ranvier: ultrastructural analysis of HRP-filled astrocytes in the mouse optic nerve. J. Neurocytol. 23: 486-499.

90. Rothstein JD, Dykes-Hoberg M, Pardo CA, Bristol LA, Jin L, Kuncl RW, Kanai Y, Hediger MA, Wang Y, Schielke JP & Welty DF. 1996. Knockout of glutamate transporters reveals a major role for astroglial transport in excitotoxicity and clearance of glutamate. Neuron. 16: 675-686.

91. Abbott NJ, Ronnback L & Hansson E. 2006. Astrocyte-endothelial interactions at the blood-brain barrier. Nat. Rev. Neurosci. 7: 41-53.

92. Eddleston M & Mucke L. 1993. Molecular profile of reactive astrocytes--implications for their role in neurologic disease. Neuroscience. 54: 15-36.

93. Sofroniew MV. 2009. Molecular dissection of reactive astrogliosis and glial scar formation. Trends Neurosci. 32: 638-647.

94. Rolls A, Shechter R & Schwartz M. 2009. The bright side of the glial scar in CNS repair. Nat. Rev. Neurosci. 10: 235-241.

95. Tan AM, Zhang W & Levine JM. 2005. NG2: a component of the glial scar that inhibits axon growth. J. Anat. 207: 717-725.

96. Fitch MT & Silver J. 1997. Activated macrophages and the blood-brain barrier: inflammation after CNS injury leads to increases in putative inhibitory molecules. Exp. Neurol. 148: 587-603.

97. Wong EV, David S, Jacob MH & Jay DG. 2003. Inactivation of myelin-associated glycoprotein enhances optic nerve regeneration. J. Neurosci. 23: 3112-3117.

98. Fawcett JW & Asher RA. 1999. The glial scar and central nervous system repair. Brain Res. Bull. 49: 377-391.

99. Bush TG, Savidge TC, Freeman TC, Cox HJ, Campbell EA, Mucke L, Johnson MH & Sofroniew MV. 1998. Fulminant jejuno-ileitis following ablation of enteric glia in adult transgenic mice. Cell. 93: 189-201.

100. Bush TG, Puvanachandra N, Horner CH, Polito A, Ostenfeld T, Svendsen CN, Mucke L, Johnson MH & Sofroniew MV. 1999. Leukocyte infiltration, neuronal

degeneration, and neurite outgrowth after ablation of scar-forming, reactive astrocytes in adult transgenic mice. Neuron. 23: 297-308.

101. Kokoris MS & Black ME. 2002. Characterization of herpes simplex virus type 1 thymidine kinase mutants engineered for improved ganciclovir or acyclovir activity. Protein Sci. 11: 2267-2272.

102. Sun D, Lye-Barthel M, Masland RH & Jakobs TC. 2010. Structural remodeling of fibrous astrocytes after axonal injury. J. Neurosci. 30: 14008-14019.

103. Sun D, Qu J & Jakobs TC. 2013. Reversible reactivity by optic nerve astrocytes. Glia. 61: 1218-1235.

104. Son JL, Soto I, Oglesby E, Lopez-Roca T, Pease ME, Quigley HA & Marsh-Armstrong N. 2010. Glaucomatous optic nerve injury involves early astrocyte reactivity and late oligodendrocyte loss. Glia. 58: 780-789.

105. Sacca SC, Rolando M, Marletta A, Macri A, Cerqueti P & Ciurlo G. 1998. Fluctuations of intraocular pressure during the day in open-angle glaucoma, normal-tension glaucoma and normal subjects. Ophthalmologica. 212: 115-119.

106. Hong S, Seong GJ & Hong YJ. 2007. Long-term intraocular pressure fluctuation and progressive visual field deterioration in patients with glaucoma and low intraocular pressures after a triple procedure. Arch. Ophthalmol. 125: 1010-1013.

107. Lye-Barthel M, Sun D & Jakobs TC. 2013. Morphology of astrocytes in a glaucomatous optic nerve. Invest. Ophthalmol. Vis. Sci. 54: 909-917.

108. Neufeld AH. 1999. Microglia in the optic nerve head and the region of parapapillary chorioretinal atrophy in glaucoma. Arch. Ophthalmol. 117: 1050-1056.

109. Wilms H, Hartmann D & Sievers J. 1997. Ramification of microglia, monocytes and macrophages in vitro: influences of various epithelial and mesenchymal cells and their conditioned media. Cell Tissue Res. 287: 447-458.

110. Ling EA & Wong WC. 1993. The origin and nature of ramified and amoeboid microglia: a historical review and current concepts. Glia. 7: 9-18.

111. Nimmerjahn A, Kirchhoff F & Helmchen F. 2005. Resting microglial cells are highly dynamic surveillants of brain parenchyma in vivo. Science. 308: 1314-1318.

112. Neumann H, Kotter MR & Franklin RJ. 2009. Debris clearance by microglia: an essential link between degeneration and regeneration. Brain. 132: 288-295.

113. Sokolowski JD & Mandell JW. 2011. Phagocytic clearance in neurodegeneration. Am. J. Pathol. 178: 1416-1428.

114. Kreutzberg GW. 1996. Microglia: a sensor for pathological events in the CNS. Trends Neurosci. 19: 312-318.

115. Liu B & Hong JS. 2003. Role of microglia in inflammation-mediated neurodegenerative diseases: mechanisms and strategies for therapeutic intervention. J. Pharmacol. Exp. Ther. 304: 1-7.

116. Zhang W, Wang T, Pei Z, Miller DS, Wu X, Block ML, Wilson B, Zhang W, Zhou Y, Hong JS & Zhang J. 2005. Aggregated alpha-synuclein activates microglia: a process leading to disease progression in Parkinson's disease. FASEB J. 19: 533-542.

117. Andersen JK. 2004. Oxidative stress in neurodegeneration: cause or consequence? Nat. Med. 10 Suppl: S18-25.

118. Uttara B, Singh AV, Zamboni P & Mahajan RT. 2009. Oxidative stress and neurodegenerative diseases: a review of upstream and downstream antioxidant therapeutic options. Curr. Neuropharmacol. 7: 65-74.

119. Babior BM. 1999. NADPH oxidase: an update. Blood. 93: 1464-1476.

120. Loane DJ & Byrnes KR. 2010. Role of microglia in neurotrauma. Neurotherapeutics. 7: 366-377.

121. Hill KE, Zollinger LV, Watt HE, Carlson NG & Rose JW. 2004. Inducible nitric oxide synthase in chronic active multiple sclerosis plaques: distribution, cellular expression and association with myelin damage. J. Neuroimmunol. 151: 171-179.

122. Pinteaux-Jones F, Sevastou IG, Fry VA, Heales S, Baker D & Pocock JM. 2008. Myelin-induced microglial neurotoxicity can be controlled by microglial metabotropic glutamate receptors. J. Neurochem. 106: 442-454.

123. van Horssen J, Witte ME, Schreibelt G & de Vries HE. 2011. Radical changes in multiple sclerosis pathogenesis. Biochim. Biophys. Acta. 1812: 141-150.

124. Haider L, Fischer MT, Frischer JM, Bauer J, Hoftberger R, Botond G, Esterbauer H, Binder CJ, Witztum JL & Lassmann H. 2011. Oxidative damage in multiple sclerosis lesions. Brain. 134: 1914-1924.

125. Reichert F, Saada A & Rotshenker S. 1994. Peripheral nerve injury induces Schwann cells to express two macrophage phenotypes: phagocytosis and the galactose-specific lectin MAC-2. J. Neurosci. 14: 3231-3245.

126. Reichert F & Rotshenker S. 1996. Deficient activation of microglia during optic nerve degeneration. J. Neuroimmunol. 70: 153-161.

127. Liu KM & Shen CL. 1985. Ultrastructural sequence of myelin breakdown during Wallerian degeneration in the rat optic nerve. Cell Tissue Res. 242: 245-256.

128. Ludwin SK. 1990. Phagocytosis in the rat optic nerve following Wallerian degeneration. Acta Neuropathol. 80: 266-273.

129. Lassmann H, Ammerer HP & Kulnig W. 1978. Ultrastructural sequence of myelin degradation. I. Wallerian degeneration in the rat optic nerve. Acta Neuropathol. 44: 91-102.

130. Gitik M, Liraz-Zaltsman S, Oldenborg PA, Reichert F & Rotshenker S. 2011. Myelin down-regulates myelin phagocytosis by microglia and macrophages through interactions between CD47 on myelin and SIRPalpha (signal regulatory protein-alpha) on phagocytes. J. Neuroinflammation. 8: 24-2094-8-24.

131. Yuan L & Neufeld AH. 2001. Activated microglia in the human glaucomatous optic nerve head. J. Neurosci. Res. 64: 523-532.

132. Yuan L & Neufeld AH. 2000. Tumor necrosis factor-alpha: a potentially neurodestructive cytokine produced by glia in the human glaucomatous optic nerve head. Glia. 32: 42-50.

133. Yan X, Tezel G, Wax MB & Edward DP. 2000. Matrix metalloproteinases and tumor necrosis factor alpha in glaucomatous optic nerve head. Arch. Ophthalmol. 118: 666-673.

134. Neufeld AH, Hernandez MR & Gonzalez M. 1997. Nitric oxide synthase in the human glaucomatous optic nerve head. Arch. Ophthalmol. 115: 497-503.

135. Pang IH, Johnson EC, Jia L, Cepurna WO, Shepard AR, Hellberg MR, Clark AF & Morrison JC. 2005. Evaluation of inducible nitric oxide synthase in glaucomatous optic neuropathy and pressure-induced optic nerve damage. Invest. Ophthalmol. Vis. Sci. 46: 1313-1321.

136. Libby RT, Howell GR, Pang IH, Savinova OV, Mehalow AK, Barter JW, Smith RS, Clark AF & John SW. 2007. Inducible nitric oxide synthase, Nos2, does not mediate optic neuropathy and retinopathy in the DBA/2J glaucoma model. BMC Neurosci. 8: 108.

137. Bosco A, Steele MR & Vetter ML. 2011. Early microglia activation in a mouse model of chronic glaucoma. J. Comp. Neurol. 519: 599-620.

138. Inman DM & Horner PJ. 2007. Reactive nonproliferative gliosis predominates in a chronic mouse model of glaucoma. Glia. 55: 942-953.

139. Luft JH. 1956. The fine structure of the electric organ of the electric eel and torpedo ray; preliminary communication. J. Biophys. Biochem. Cytol. 2: 229-232.

140. Carlson SS & Kelly RB. 1980. An antiserum specific for cholinergic synaptic vesicles from electric organ. J. Cell Biol. 87: 98-103.

141. Maroteaux L, Campanelli JT & Scheller RH. 1988. Synuclein: a neuron-specific protein localized to the nucleus and presynaptic nerve terminal. J. Neurosci. 8: 2804-2815.

142. Maroteaux L & Scheller RH. 1991. The rat brain synucleins; family of proteins transiently associated with neuronal membrane. Brain Res. Mol. Brain Res. 11: 335-343.

143. Lavedan C. 1998. The synuclein family. Genome Res. 8: 871-880.

144. Surguchov A. 2008. Molecular and cellular biology of synucleins. Int. Rev. Cell. Mol. Biol. 270: 225-317.

145. Ueda K, Fukushima H, Masliah E, Xia Y, Iwai A, Yoshimoto M, Otero DA, Kondo J, Ihara Y & Saitoh T. 1993. Molecular cloning of cDNA encoding an unrecognized component of amyloid in Alzheimer disease. Proc. Natl. Acad. Sci. U. S. A. 90: 11282-11286.

146. Jakes R, Spillantini MG & Goedert M. 1994. Identification of two distinct synucleins from human brain. FEBS Lett. 345: 27-32.

147. Waxman EA, Mazzulli JR & Giasson BI. 2009. Characterization of hydrophobic residue requirements for alpha-synuclein fibrillization. Biochemistry. 48: 9427-9436.

148. Bondareff W, Wischik CM, Novak M & Roth M. 1991. Sequestration of tau by granulovacuolar degeneration in Alzheimer's disease. Am. J. Pathol. 139: 641-647.

149. George JM, Jin H, Woods WS & Clayton DF. 1995. Characterization of a novel protein regulated during the critical period for song learning in the zebra finch. Neuron. 15: 361-372.

150. Jin H & Clayton DF. 1997. Synelfin regulation during the critical period for song learning in normal and isolated juvenile zebra finches. Neurobiol. Learn. Mem. 68: 271-284.

151. Burre J, Sharma M, Tsetsenis T, Buchman V, Etherton MR & Sudhof TC. 2010. Alpha-synuclein promotes SNARE-complex assembly in vivo and in vitro. Science. 329: 1663-1667.

152. Nemani VM, Lu W, Berge V, Nakamura K, Onoa B, Lee MK, Chaudhry FA, Nicoll RA & Edwards RH. 2010. Increased expression of alpha-synuclein reduces

neurotransmitter release by inhibiting synaptic vesicle reclustering after endocytosis. Neuron. 65: 66-79.

153. Scott D & Roy S. 2012. alpha-Synuclein inhibits intersynaptic vesicle mobility and maintains recycling-pool homeostasis. J. Neurosci. 32: 10129-10135.

154. Scott DA, Tabarean I, Tang Y, Cartier A, Masliah E & Roy S. 2010. A pathologic cascade leading to synaptic dysfunction in alpha-synuclein-induced neurodegeneration. J. Neurosci. 30: 8083-8095.

155. Verhage M, Maia AS, Plomp JJ, Brussaard AB, Heeroma JH, Vermeer H, Toonen RF, Hammer RE, van den Berg TK, Missler M, Geuze HJ & Sudhof TC. 2000. Synaptic assembly of the brain in the absence of neurotransmitter secretion. Science. 287: 864-869.

156. Uversky VN, Li J & Fink AL. 2001. Evidence for a partially folded intermediate in alpha-synuclein fibril formation. J. Biol. Chem. 276: 10737-10744.

157. Neumann M, Kahle PJ, Giasson BI, Ozmen L, Borroni E, Spooren W, Muller V, Odoy S, Fujiwara H, Hasegawa M, Iwatsubo T, Trojanowski JQ, Kretzschmar HA & Haass C. 2002. Misfolded proteinase K-resistant hyperphosphorylated alpha-synuclein in aged transgenic mice with locomotor deterioration and in human alpha-synucleinopathies. J. Clin. Invest. 110: 1429-1439.

158. Miake H, Mizusawa H, Iwatsubo T & Hasegawa M. 2002. Biochemical characterization of the core structure of alpha-synuclein filaments. J. Biol. Chem. 277: 19213-19219.

159. Kayed R, Head E, Thompson JL, McIntire TM, Milton SC, Cotman CW & Glabe CG. 2003. Common structure of soluble amyloid oligomers implies common mechanism of pathogenesis. Science. 300: 486-489.

160. Winner B, Jappelli R, Maji SK, Desplats PA, Boyer L, Aigner S, Hetzer C, Loher T, Vilar M, Campioni S, Tzitzilonis C, Soragni A, Jessberger S, Mira H, Consiglio A, Pham E, Masliah E, Gage FH & Riek R. 2011. In vivo demonstration that alpha-synuclein oligomers are toxic. Proc. Natl. Acad. Sci. U. S. A. 108: 4194-4199.

161. Volles MJ & Lansbury PT,Jr. 2003. Zeroing in on the pathogenic form of alpha-synuclein and its mechanism of neurotoxicity in Parkinson's disease. Biochemistry. 42: 7871-7878.

162. Mazzulli JR, Xu YH, Sun Y, Knight AL, McLean PJ, Caldwell GA, Sidransky E, Grabowski GA & Krainc D. 2011. Gaucher disease glucocerebrosidase and alpha-synuclein form a bidirectional pathogenic loop in synucleinopathies. Cell. 146: 37-52.

163. Ji H, Liu YE, Jia T, Wang M, Liu J, Xiao G, Joseph BK, Rosen C & Shi YE. 1997. Identification of a breast cancer-specific gene, BCSG1, by direct differential cDNA sequencing. Cancer Res. 57: 759-764.

164. Gupta A, Inaba S, Wong OK, Fang G & Liu J. 2003. Breast cancer-specific gene 1 interacts with the mitotic checkpoint kinase BubR1. Oncogene. 22: 7593-7599.

165. Miao S, Wu K, Zhang B, Weng Z, Zhu M, Lu Y, Krishna R & Shi YE. 2014. Synuclein gamma compromises spindle assembly checkpoint and renders resistance to antimicrotubule drugs. Mol. Cancer. Ther. 13: 699-713.

166. Inaba S, Li C, Shi YE, Song DQ, Jiang JD & Liu J. 2005. Synuclein gamma inhibits the mitotic checkpoint function and promotes chromosomal instability of breast cancer cells. Breast Cancer Res. Treat. 94: 25-35.

167. Lavedan C, Leroy E, Dehejia A, Buchholtz S, Dutra A, Nussbaum RL & Polymeropoulos MH. 1998. Identification, localization and characterization of the human gamma-synuclein gene. Hum. Genet. 103: 106-112.

168. Buchman VL, Hunter HJ, Pinon LG, Thompson J, Privalova EM, Ninkina NN & Davies AM. 1998. Persyn, a member of the synuclein family, has a distinct pattern of expression in the developing nervous system. J. Neurosci. 18: 9335-9341.

169. Galvin JE, Uryu K, Lee VM & Trojanowski JQ. 1999. Axon pathology in Parkinson's disease and Lewy body dementia hippocampus contains alpha-, beta-, and gamma-synuclein. Proc. Natl. Acad. Sci. U. S. A. 96: 13450-13455.

170. Galvin JE, Giasson B, Hurtig HI, Lee VM & Trojanowski JQ. 2000. Neurodegeneration with brain iron accumulation, type 1 is characterized by alpha-, beta-, and gamma-synuclein neuropathology. Am. J. Pathol. 157: 361-368.

171. Surgucheva I, McMahan B, Ahmed F, Tomarev S, Wax MB & Surguchov A. 2002. Synucleins in glaucoma: implication of gamma-synuclein in glaucomatous alterations in the optic nerve. J. Neurosci. Res. 68: 97-106.

172. Surgucheva I, Weisman AD, Goldberg JL, Shnyra A & Surguchov A. 2008. Gamma-synuclein as a marker of retinal ganglion cells. Mol. Vis. 14: 1540-1548.

173. Fink AL. 2006. The aggregation and fibrillation of alpha-synuclein. Acc. Chem. Res. 39: 628-634.

174. Ninkina N, Peters O, Millership S, Salem H, van der Putten H & Buchman VL. 2009. Gamma-synucleinopathy: neurodegeneration associated with overexpression of the mouse protein. Hum. Mol. Genet. 18: 1779-1794.

175. Peters OM, Millership S, Shelkovnikova TA, Soto I, Keeling L, Hann A, Marsh-Armstrong N, Buchman VL & Ninkina N. 2012. Selective pattern of motor system damage in gamma-synuclein transgenic mice mirrors the respective pathology in amyotrophic lateral sclerosis. Neurobiol. Dis. 48: 124-131.

176. Ninkina N, Papachroni K, Robertson DC, Schmidt O, Delaney L, O'Neill F, Court F, Rosenthal A, Fleetwood-Walker SM, Davies AM & Buchman VL. 2003. Neurons expressing the highest levels of gamma-synuclein are unaffected by targeted inactivation of the gene. Mol. Cell. Biol. 23: 8233-8245.

177. Jia T, Liu YE, Liu J & Shi YE. 1999. Stimulation of breast cancer invasion and metastasis by synuclein gamma. Cancer Res. 59: 742-747.

178. Wu K, Weng Z, Tao Q, Lin G, Wu X, Qian H, Zhang Y, Ding X, Jiang Y & Shi YE. 2003. Stage-specific expression of breast cancer-specific gene gamma-synuclein. Cancer Epidemiol. Biomarkers Prev. 12: 920-925.

179. Chen J, Jiao L, Xu C, Yu Y, Zhang Z, Chang Z, Deng Z & Sun Y. 2012. Neural protein gamma-synuclein interacting with androgen receptor promotes human prostate cancer progression. BMC Cancer. 12: 593-2407-12-593.

180. Ninkina NN, Alimova-Kost MV, Paterson JW, Delaney L, Cohen BB, Imreh S, Gnuchev NV, Davies AM & Buchman VL. 1998. Organization, expression and polymorphism of the human persyn gene. Hum. Mol. Genet. 7: 1417-1424.

181. Ito D, Imai Y, Ohsawa K, Nakajima K, Fukuuchi Y & Kohsaka S. 1998. Microglia-specific localisation of a novel calcium binding protein, Iba1. Brain Res. Mol. Brain Res. 57: 1-9.

182. Bosco A, Steele MR & Vetter ML. 2011. Early microglia activation in a mouse model of chronic glaucoma. J. Comp. Neurol. 519: 599-620.

183. Block ML, Zecca L & Hong JS. 2007. Microglia-mediated neurotoxicity: uncovering the molecular mechanisms. Nat. Rev. Neurosci. 8: 57-69.

184. Takeda A, Hashimoto M, Mallory M, Sundsumo M, Hansen L, Sisk A & Masliah E. 1998. Abnormal distribution of the non-Abeta component of Alzheimer's disease amyloid precursor/alpha-synuclein in Lewy body disease as revealed by proteinase K and formic acid pretreatment. Lab. Invest. 78: 1169-1177.

185. Takeda A, Hashimoto M, Mallory M, Sundsumo M, Hansen L & Masliah E. 2000. C-terminal alpha-synuclein immunoreactivity in structures other than Lewy bodies in neurodegenerative disorders. Acta Neuropathol. 99: 296-304.

186. Kinchen JM & Ravichandran KS. 2007. Journey to the grave: signaling events regulating removal of apoptotic cells. J. Cell. Sci. 120: 2143-2149.

187. Asano K, Miwa M, Miwa K, Hanayama R, Nagase H, Nagata S & Tanaka M. 2004. Masking of phosphatidylserine inhibits apoptotic cell engulfment and induces autoantibody production in mice. J. Exp. Med. 200: 459-467.

188. Howell GR, Walton DO, King BL, Libby RT & John SW. 2011. Datgan, a reusable software system for facile interrogation and visualization of complex transcription profiling data. BMC Genomics. 12: 429-2164-12-429.

189. Howell GR, Macalinao DG, Sousa GL, Walden M, Soto I, Kneeland SC, Barbay JM, King BL, Marchant JK, Hibbs M, Stevens B, Barres BA, Clark AF, Libby RT & John SW. 2011. Molecular clustering identifies complement and endothelin induction as early events in a mouse model of glaucoma. J. Clin. Invest. 121: 1429-1444.

190. Howell GR, Walton DO, King BL & John SWM. 2009-2014. Glaucoma Discovery Platform. The Jackson Laboratory. http://glaucomadb.jax.org/glaucoma.

191. Mabuchi F, Aihara M, Mackey MR, Lindsey JD & Weinreb RN. 2003. Optic nerve damage in experimental mouse ocular hypertension. Invest. Ophthalmol. Vis. Sci. 44: 4321-4330.

192. Vidal-Sanz M, Villegas-Perez MP, Bray GM & Aguayo AJ. 1988. Persistent retrograde labeling of adult rat retinal ganglion cells with the carbocyanine dye diI. Exp. Neurol. 102: 92-101.

193. Li M, Yin Y, Hua H, Sun X, Luo T, Wang J & Jiang Y. 2010. The reciprocal regulation of gamma-synuclein and IGF-I receptor expression creates a circuit that modulates IGF-I signaling. J. Biol. Chem. 285: 30480-30488.

194. Jiang Y, Liu YE, Goldberg ID & Shi YE. 2004. Gamma synuclein, a novel heat-shock protein-associated chaperone, stimulates ligand-dependent estrogen receptor alpha signaling and mammary tumorigenesis. Cancer Res. 64: 4539-4546.

195. Shi YE, Chen Y, Dackour R, Potters L, Wang S, Ding Q, Wang Z & Liu YE. 2010. Synuclein gamma stimulates membrane-initiated estrogen signaling by chaperoning estrogen receptor (ER)-alpha36, a variant of ER-alpha. Am. J. Pathol. 177: 964-973.

196. Li JY, Englund E, Widner H, Rehncrona S, Bjorklund A, Lindvall O & Brundin P. 2010. Characterization of Lewy body pathology in 12- and 16-year-old intrastriatal mesencephalic grafts surviving in a patient with Parkinson's disease. Mov. Disord. 25: 1091-1096.

197. Li JY, Englund E, Holton JL, Soulet D, Hagell P, Lees AJ, Lashley T, Quinn NP, Rehncrona S, Bjorklund A, Widner H, Revesz T, Lindvall O & Brundin P. 2008. Lewy bodies in grafted neurons in subjects with Parkinson's disease suggest host-to-graft disease propagation. Nat. Med. 14: 501-503.

198. Kordower JH, Chu Y, Hauser RA, Freeman TB & Olanow CW. 2008. Lewy body-like pathology in long-term embryonic nigral transplants in Parkinson's disease. Nat. Med. 14: 504-506.

199. Hansen C, Angot E, Bergstrom AL, Steiner JA, Pieri L, Paul G, Outeiro TF, Melki R, Kallunki P, Fog K, Li JY & Brundin P. 2011. alpha-Synuclein propagates from mouse brain to grafted dopaminergic neurons and seeds aggregation in cultured human cells. J. Clin. Invest. 121: 715-725.

200. Desplats P, Lee HJ, Bae EJ, Patrick C, Rockenstein E, Crews L, Spencer B, Masliah E & Lee SJ. 2009. Inclusion formation and neuronal cell death through neuron-to-neuron transmission of alpha-synuclein. Proc. Natl. Acad. Sci. U. S. A. 106: 13010-13015.

201. Lee HJ, Suk JE, Patrick C, Bae EJ, Cho JH, Rho S, Hwang D, Masliah E & Lee SJ. 2010. Direct transfer of alpha-synuclein from neuron to astroglia causes inflammatory responses in synucleinopathies. J. Biol. Chem. 285: 9262-9272.

202. Lööv C, Hillered L, Ebendal T & Erlandsson A. 2012. Engulfing astrocytes protect neurons from contact-induced apoptosis following injury. PLoS One. 7: e33090.

203. Chung WS, Clarke LE, Wang GX, Stafford BK, Sher A, Chakraborty C, Joung J, Foo LC, Thompson A, Chen C, Smith SJ & Barres BA. 2013. Astrocytes mediate synapse elimination through MEGF10 and MERTK pathways. Nature. 504: 394-400.

204. Kinchen JM, Cabello J, Klingele D, Wong K, Feichtinger R, Schnabel H, Schnabel R & Hengartner MO. 2005. Two pathways converge at CED-10 to mediate actin rearrangement and corpse removal in C. elegans. Nature. 434: 93-99.

205. Barondes SH, Castronovo V, Cooper DN, Cummings RD, Drickamer K, Feizi T, Gitt MA, Hirabayashi J, Hughes C & Kasai K. 1994. Galectins: a family of animal beta-galactoside-binding lectins. Cell. 76: 597-598.

206. Reichert F & Rotshenker S. 1999. Galectin-3/MAC-2 in experimental allergic encephalomyelitis. Exp. Neurol. 160: 508-514.

207. Rotshenker S. 2009. The role of Galectin-3/MAC-2 in the activation of the innate-immune function of phagocytosis in microglia in injury and disease. J. Mol. Neurosci. 39: 99-103.

208. Boiko T, Rasband MN, Levinson SR, Caldwell JH, Mandel G, Trimmer JS & Matthews G. 2001. Compact myelin dictates the differential targeting of two sodium channel isoforms in the same axon. Neuron. 30: 91-104.

209. Craner MJ, Lo AC, Black JA & Waxman SG. 2003. Abnormal sodium channel distribution in optic nerve axons in a model of inflammatory demyelination. Brain. 126: 1552-1561.

210. Mantegazza M, Curia G, Biagini G, Ragsdale DS & Avoli M. 2010. Voltage-gated sodium channels as therapeutic targets in epilepsy and other neurological disorders. Lancet Neurol. 9: 413-424.

211. Smith KJ. 2007. Sodium channels and multiple sclerosis: roles in symptom production, damage and therapy. Brain Pathol. 17: 230-242.

212. Waxman SG. 2008. Mechanisms of disease: sodium channels and neuroprotection in multiple sclerosis-current status. Nat. Clin. Pract. Neurol. 4: 159-169.

213. Waxman SG. 2002. Sodium channels as molecular targets in multiple sclerosis. J. Rehabil. Res. Dev. 39: 233-242.

214. Black JA, Newcombe J, Trapp BD & Waxman SG. 2007. Sodium channel expression within chronic multiple sclerosis plaques. J. Neuropathol. Exp. Neurol. 66: 828-837.

215. Craner MJ, Hains BC, Lo AC, Black JA & Waxman SG. 2004. Co-localization of sodium channel Nav1.6 and the sodium-calcium exchanger at sites of axonal injury in the spinal cord in EAE. Brain. 127: 294-303.

216. Stys PK, Waxman SG & Ransom BR. 1992. Ionic mechanisms of anoxic injury in mammalian CNS white matter: role of Na+ channels and Na(+)-Ca2+ exchanger. J. Neurosci. 12: 430-439.

217. Knoferle J, Koch JC, Ostendorf T, Michel U, Planchamp V, Vutova P, Tonges L, Stadelmann C, Bruck W, Bahr M & Lingor P. 2010. Mechanisms of acute axonal degeneration in the optic nerve in vivo. Proc. Natl. Acad. Sci. U. S. A. 107: 6064-6069.

218. Morsali D, Bechtold D, Lee W, Chauhdry S, Palchaudhuri U, Hassoon P, Snell DM, Malpass K, Piers T, Pocock J, Roach A & Smith KJ. 2013. Safinamide and flecainide protect axons and reduce microglial activation in models of multiple sclerosis. Brain. 136: 1067-1082.

219. Tarnawa I, Bolcskei H & Kocsis P. 2007. Blockers of voltage-gated sodium channels for the treatment of central nervous system diseases. Recent. Pat. CNS Drug Discov. 2: 57-78.

220. Eijkelkamp N, Linley JE, Baker MD, Minett MS, Cregg R, Werdehausen R, Rugiero F & Wood JN. 2012. Neurological perspectives on voltage-gated sodium channels. Brain. 135: 2585-2612.

221. Yang LJ, Zeller CB, Shaper NL, Kiso M, Hasegawa A, Shapiro RE & Schnaar RL. 1996. Gangliosides are neuronal ligands for myelin-associated glycoprotein. Proc. Natl. Acad. Sci. U. S. A. 93: 814-818.

222. Trapp BD, Andrews SB, Cootauco C & Quarles R. 1989. The myelin-associated glycoprotein is enriched in multivesicular bodies and periaxonal membranes of actively myelinating oligodendrocytes. J. Cell Biol. 109: 2417-2426.

223. Heath JW, Inuzuka T, Quarles RH & Trapp BD. 1991. Distribution of P0 protein and the myelin-associated glycoprotein in peripheral nerves from Trembler mice. J. Neurocytol. 20: 439-449.

224. Vyas AA, Patel HV, Fromholt SE, Heffer-Lauc M, Vyas KA, Dang J, Schachner M & Schnaar RL. 2002. Gangliosides are functional nerve cell ligands for myelin-associated glycoprotein (MAG), an inhibitor of nerve regeneration. Proc. Natl. Acad. Sci. U. S. A. 99: 8412-8417.

225. Mehta NR, Lopez PH, Vyas AA & Schnaar RL. 2007. Gangliosides and Nogo receptors independently mediate myelin-associated glycoprotein inhibition of neurite outgrowth in different nerve cells. J. Biol. Chem. 282: 27875-27886.

226. DeBellard ME, Tang S, Mukhopadhyay G, Shen YJ & Filbin MT. 1996. Myelin-associated glycoprotein inhibits axonal regeneration from a variety of neurons via interaction with a sialoglycoprotein. Mol. Cell. Neurosci. 7: 89-101.

227. Li C, Tropak MB, Gerlai R, Clapoff S, Abramow-Newerly W, Trapp B, Peterson A & Roder J. 1994. Myelination in the absence of myelin-associated glycoprotein. Nature. 369: 747-750.

228. Susuki K, Baba H, Tohyama K, Kanai K, Kuwabara S, Hirata K, Furukawa K, Furukawa K, Rasband MN & Yuki N. 2007. Gangliosides contribute to stability of paranodal junctions and ion channel clusters in myelinated nerve fibers. Glia. 55: 746-757.

229. Marcus J, Dupree JL & Popko B. 2002. Myelin-associated glycoprotein and myelin galactolipids stabilize developing axo-glial interactions. J. Cell Biol. 156: 567-577.

230. Bosio A, Binczek E & Stoffel W. 1996. Molecular cloning and characterization of the mouse CGT gene encoding UDP-galactose ceramide-galactosyltransferase (cerebroside synthetase). Genomics. 35: 223-226.

231. Ransom BR & Orkand RK. 1996. Glial-neuronal interactions in non-synaptic areas of the brain: studies in the optic nerve. Trends Neurosci. 19: 352-358.

232. Bergles DE & Jahr CE. 1998. Glial contribution to glutamate uptake at Schaffer collateral-commissural synapses in the hippocampus. J. Neurosci. 18: 7709-7716.

233. Tanaka K, Watase K, Manabe T, Yamada K, Watanabe M, Takahashi K, Iwama H, Nishikawa T, Ichihara N, Kikuchi T, Okuyama S, Kawashima N, Hori S, Takimoto M &

Wada K. 1997. Epilepsy and exacerbation of brain injury in mice lacking the glutamate transporter GLT-1. Science. 276: 1699-1702.

234. Arranz AM, Hussein A, Alix JJ, Perez-Cerda F, Allcock N, Matute C & Fern R. 2008. Functional glutamate transport in rodent optic nerve axons and glia. Glia. 56: 1353-1367.

235. Goritz C, Mauch DH, Nagler K & Pfrieger FW. 2002. Role of glia-derived cholesterol in synaptogenesis: new revelations in the synapse-glia affair. J. Physiol. Paris. 96: 257-263.

236. Pfrieger FW. 2003. Role of cholesterol in synapse formation and function. Biochim. Biophys. Acta. 1610: 271-280.

237. Pfrieger FW & Barres BA. 1997. Synaptic efficacy enhanced by glial cells in vitro. Science. 277: 1684-1687.

238. Matsuo A, Lee GC, Terai K, Takami K, Hickey WF, McGeer EG & McGeer PL. 1997. Unmasking of an unusual myelin basic protein epitope during the process of myelin degeneration in humans: a potential mechanism for the generation of autoantigens. Am. J. Pathol. 150: 1253-1266.

239. Matsuo A, Akiguchi I, Lee GC, McGeer EG, McGeer PL & Kimura J. 1998. Myelin degeneration in multiple system atrophy detected by unique antibodies. Am. J. Pathol. 153: 735-744.

240. Wakita H, Tomimoto H, Akiguchi I, Matsuo A, Lin J, Ihara M & McGeer P. 2002. Axonal damage and demyelination in the white matter after chronic cerebral hypoperfusion in the rat. Brain Res. 924: 63-70.

241. Belogurov AA,Jr, Kurkova IN, Friboulet A, Thomas D, Misikov VK, Zakharova MY, Suchkov SV, Kotov SV, Alehin AI, Avalle B, Souslova EA, Morse HC,3rd, Gabibov AG & Ponomarenko NA. 2008. Recognition and degradation of myelin basic protein peptides by serum autoantibodies: novel biomarker for multiple sclerosis. J. Immunol. 180: 1258-1267.

242. Ponomarenko NA, Durova OM, Vorobiev II, Belogurov AA,Jr, Kurkova IN, Petrenko AG, Telegin GB, Suchkov SV, Kiselev SL, Lagarkova MA, Govorun VM, Serebryakova MV, Avalle B, Tornatore P, Karavanov A, Morse HC,3rd, Thomas D, Friboulet A & Gabibov AG. 2006. Autoantibodies to myelin basic protein catalyze site-specific degradation of their antigen. Proc. Natl. Acad. Sci. U. S. A. 103: 281-286.

243. Carbonell AL, Boya J, Calvo JL & Marin JF. 1991. Ultrastructural study of the neuroglial and macrophagic reaction in Wallerian degeneration of the adult rat optic nerve. Histol. Histopathol. 6: 443-451.

244. Listenberger LL & Brown DA. 2007. Fluorescent detection of lipid droplets and associated proteins. Curr. Protoc. Cell. Biol. Chapter 24: Unit 24.2.

245. McDonough PM, Agustin RM, Ingermanson RS, Loy PA, Buehrer BM, Nicoll JB, Prigozhina NL, Mikic I & Price JH. 2009. Quantification of lipid droplets and associated proteins in cellular models of obesity via high-content/high-throughput microscopy and automated image analysis. Assay Drug Dev. Technol. 7: 440-460.

246. Kinkel AD, Fernyhough ME, Helterline DL, Vierck JL, Oberg KS, Vance TJ, Hausman GJ, Hill RA & Dodson MV. 2004. Oil red-O stains non-adipogenic cells: a precautionary note. Cytotechnology. 46: 49-56.

247. Brasaemle DL, Barber T, Wolins NE, Serrero G, Blanchette-Mackie EJ & Londos C. 1997. Adipose differentiation-related protein is an ubiquitously expressed lipid storage droplet-associated protein. J. Lipid Res. 38: 2249-2263.

248. Heid HW, Moll R, Schwetlick I, Rackwitz HR & Keenan TW. 1998. Adipophilin is a specific marker of lipid accumulation in diverse cell types and diseases. Cell Tissue Res. 294: 309-321.

249. Xu G, Sztalryd C, Lu X, Tansey JT, Gan J, Dorward H, Kimmel AR & Londos C. 2005. Post-translational regulation of adipose differentiation-related protein by the ubiquitin/proteasome pathway. J. Biol. Chem. 280: 42841-42847.

250. Young KM, Psachoulia K, Tripathi RB, Dunn SJ, Cossell L, Attwell D, Tohyama K & Richardson WD. 2013. Oligodendrocyte dynamics in the healthy adult CNS: evidence for myelin remodeling. Neuron. 77: 873-885.

251. Brusaferri F & Candelise L. 2000. Steroids for multiple sclerosis and optic neuritis: a meta-analysis of randomized controlled clinical trials. J. Neurol. 247: 435-442.

252. Brusa A, Jones SJ & Plant GT. 2001. Long-term remyelination after optic neuritis: A 2-year visual evoked potential and psychophysical serial study. Brain. 124: 468-479.

253. Lachapelle F, Bachelin C, Moissonnier P, Nait-Oumesmar B, Hidalgo A, Fontaine D & Baron-Van Evercooren A. 2005. Failure of remyelination in the nonhuman primate optic nerve. Brain Pathol. 15: 198-207.

254. Kotter MR, Li WW, Zhao C & Franklin RJ. 2006. Myelin impairs CNS remyelination by inhibiting oligodendrocyte precursor cell differentiation. J. Neurosci. 26: 328-332.

255. Duncan ID, Brower A, Kondo Y, Curlee JF,Jr & Schultz RD. 2009. Extensive remyelination of the CNS leads to functional recovery. Proc. Natl. Acad. Sci. U. S. A. 106: 6832-6836.

256. LaVail MM. 1976. Rod outer segment disk shedding in rat retina: relationship to cyclic lighting. Science. 194: 1071-1074.

257. Boulton M & Marshall J. 1986. Effects of increasing numbers of phagocytic inclusions on human retinal pigment epithelial cells in culture: a model for aging. Br. J. Ophthalmol. 70: 808-815.

258. Kennedy CJ, Rakoczy PE & Constable IJ. 1995. Lipofuscin of the retinal pigment epithelium: a review. Eye (Lond). 9 (Pt 6): 763-771.

259. Sundelin S, Wihlmark U, Nilsson SE & Brunk UT. 1998. Lipofuscin accumulation in cultured retinal pigment epithelial cells reduces their phagocytic capacity. Curr. Eye Res. 17: 851-857.

260. Terman A & Brunk UT. 2004. Lipofuscin. Int. J. Biochem. Cell Biol. 36: 1400-1404.

261. Terman A, Gustafsson B & Brunk UT. 2007. Autophagy, organelles and ageing. J. Pathol. 211: 134-143.

262. Imanishi Y, Batten ML, Piston DW, Baehr W & Palczewski K. 2004. Noninvasive two-photon imaging reveals retinyl ester storage structures in the eye. J. Cell Biol. 164: 373-383.

263. Orban T, Palczewska G & Palczewski K. 2011. Retinyl ester storage particles (retinosomes) from the retinal pigmented epithelium resemble lipid droplets in other tissues. J. Biol. Chem. 286: 17248-17258.

264. Guo Y, Cordes KR, Farese RV,Jr & Walther TC. 2009. Lipid droplets at a glance. J. Cell. Sci. 122: 749-752.

265. Farese RV,Jr & Walther TC. 2009. Lipid droplets finally get a little R-E-S-P-E-C-T. Cell. 139: 855-860.

266. Murphy DJ. 2001. The biogenesis and functions of lipid bodies in animals, plants and microorganisms. Prog. Lipid Res. 40: 325-438.

267. Cheng J, Fujita A, Ohsaki Y, Suzuki M, Shinohara Y & Fujimoto T. 2009. Quantitative electron microscopy shows uniform incorporation of triglycerides into existing lipid droplets. Histochem. Cell Biol. 132: 281-291.

268. Fujimoto T & Parton RG. 2011. Not just fat: the structure and function of the lipid droplet. Cold Spring Harb Perspect. Biol. 3: 10.1101/cshperspect.a004838.

269. Bartz R, Li WH, Venables B, Zehmer JK, Roth MR, Welti R, Anderson RG, Liu P & Chapman KD. 2007. Lipidomics reveals that adiposomes store ether lipids and mediate phospholipid traffic. J. Lipid Res. 48: 837-847.

270. Wolins NE, Brasaemle DL & Bickel PE. 2006. A proposed model of fat packaging by exchangeable lipid droplet proteins. FEBS Lett. 580: 5484-5491.

271. Imanishi Y, Gerke V & Palczewski K. 2004. Retinosomes: new insights into intracellular managing of hydrophobic substances in lipid bodies. J. Cell Biol. 166: 447-453.

272. Bickel PE, Tansey JT & Welte MA. 2009. PAT proteins, an ancient family of lipid droplet proteins that regulate cellular lipid stores. Biochim. Biophys. Acta. 1791: 419-440.

273. Kimmel AR, Brasaemle DL, McAndrews-Hill M, Sztalryd C & Londos C. 2010. Adoption of PERILIPIN as a unifying nomenclature for the mammalian PAT-family of intracellular lipid storage droplet proteins. J. Lipid Res. 51: 468-471.

274. Greenberg AS, Egan JJ, Wek SA, Garty NB, Blanchette-Mackie EJ & Londos C. 1991. Perilipin, a major hormonally regulated adipocyte-specific phosphoprotein associated with the periphery of lipid storage droplets. J. Biol. Chem. 266: 11341-11346.

275. Wolins NE, Rubin B & Brasaemle DL. 2001. TIP47 associates with lipid droplets. J. Biol. Chem. 276: 5101-5108.

276. Jiang HP, Harris SE & Serrero G. 1992. Molecular cloning of a differentiation-related mRNA in the adipogenic cell line 1246. Cell Growth Differ. 3: 21-30.

277. Hsieh K, Lee YK, Londos C, Raaka BM, Dalen KT & Kimmel AR. 2012. Perilipin family members preferentially sequester to either triacylglycerol-specific or cholesteryl-ester-specific intracellular lipid storage droplets. J. Cell. Sci. 125: 4067-4076.

278. Listenberger LL, Ostermeyer-Fay AG, Goldberg EB, Brown WJ & Brown DA. 2007. Adipocyte differentiation-related protein reduces the lipid droplet association of adipose triglyceride lipase and slows triacylglycerol turnover. J. Lipid Res. 48: 2751-2761.

279. MacPherson RE, Ramos SV, Vandenboom R, Roy BD & Peters SJ. 2013. Skeletal muscle PLIN proteins, ATGL and CGI-58, interactions at rest and following stimulated contraction. Am. J. Physiol. Regul. Integr. Comp. Physiol. 304: R644-50.

280. Senthivinayagam S, McIntosh AL, Moon KC & Atshaves BP. 2013. Plin2 inhibits cellular glucose uptake through interactions with SNAP23, a SNARE complex protein. PLoS One. 8: e73696.

281. Millership S, Ninkina N, Guschina IA, Norton J, Brambilla R, Oort PJ, Adams SH, Dennis RJ, Voshol PJ, Rochford JJ & Buchman VL. 2012. Increased lipolysis and altered lipid homeostasis protect gamma-synuclein-null mutant mice from diet-induced obesity. Proc. Natl. Acad. Sci. U. S. A. 109: 20943-20948.

282. Heid HW, Schnolzer M & Keenan TW. 1996. Adipocyte differentiation-related protein is secreted into milk as a constituent of milk lipid globule membrane. Biochem. J. 320 (Pt 3): 1025-1030.

283. Chong BM, Reigan P, Mayle-Combs KD, Orlicky DJ & McManaman JL. 2011. Determinants of adipophilin function in milk lipid formation and secretion. Trends Endocrinol. Metab. 22: 211-217.

284. McManaman JL, Reyland ME & Thrower EC. 2006. Secretion and fluid transport mechanisms in the mammary gland: comparisons with the exocrine pancreas and the salivary gland. J. Mammary Gland Biol. Neoplasia. 11: 249-268.

285. Herms A, Bosch M, Ariotti N, Reddy BJ, Fajardo A, Fernandez-Vidal A, Alvarez-Guaita A, Fernandez-Rojo MA, Rentero C, Tebar F, Enrich C, Geli MI, Parton RG, Gross SP & Pol A. 2013. Cell-to-cell heterogeneity in lipid droplets suggests a mechanism to reduce lipotoxicity. Curr. Biol. 23: 1489-1496.

286. Herker E & Ott M. 2012. Emerging role of lipid droplets in host/pathogen interactions. J. Biol. Chem. 287: 2280-2287.

287. Welte MA. 2007. Proteins under new management: lipid droplets deliver. Trends Cell Biol. 17: 363-369.

288. Krishnamoorthy RR, Clark AF, Daudt D, Vishwanatha JK & Yorio T. 2013. A forensic path to RGC-5 cell line identification: lessons learned. Invest. Ophthalmol. Vis. Sci. 54: 5712-5719.

289. Van Bergen NJ, Wood JP, Chidlow G, Trounce IA, Casson RJ, Ju WK, Weinreb RN & Crowston JG. 2009. Recharacterization of the RGC-5 retinal ganglion cell line. Invest. Ophthalmol. Vis. Sci. 50: 4267-4272.

290. Ducas VC & Rhoades E. 2012. Quantifying interactions of beta-synuclein and gamma-synuclein with model membranes. J. Mol. Biol. 423: 528-539.

291. Sung YH & Eliezer D. 2006. Secondary structure and dynamics of micelle bound beta- and gamma-synuclein. Protein Sci. 15: 1162-1174.

292. Sztalryd C, Bell M, Lu X, Mertz P, Hickenbottom S, Chang BH, Chan L, Kimmel AR & Londos C. 2006. Functional compensation for adipose differentiation-related protein (ADFP) by Tip47 in an ADFP null embryonic cell line. J. Biol. Chem. 281: 34341-34348.

293. Shu X, Lev-Ram V, Deerinck TJ, Qi Y, Ramko EB, Davidson MW, Jin Y, Ellisman MH & Tsien RY. 2011. A genetically encoded tag for correlated light and electron microscopy of intact cells, tissues, and organisms. PLoS Biol. 9: e1001041.

294. Davidson WS, Jonas A, Clayton DF & George JM. 1998. Stabilization of alpha-synuclein secondary structure upon binding to synthetic membranes. J. Biol. Chem. 273: 9443-9449.

295. Eliezer D, Kutluay E, Bussell R,Jr & Browne G. 2001. Conformational properties of alpha-synuclein in its free and lipid-associated states. J. Mol. Biol. 307: 1061-1073.

296. Chandra S, Chen X, Rizo J, Jahn R & Sudhof TC. 2003. A broken alpha -helix in folded alpha -Synuclein. J. Biol. Chem. 278: 15313-15318.

297. Cole NB, Murphy DD, Grider T, Rueter S, Brasaemle D & Nussbaum RL. 2002. Lipid droplet binding and oligomerization properties of the Parkinson's disease protein alpha-synuclein. J. Biol. Chem. 277: 6344-6352.

298. Imanishi Y, Sun W, Maeda T, Maeda A & Palczewski K. 2008. Retinyl ester homeostasis in the adipose differentiation-related protein-deficient retina. J. Biol. Chem. 283: 25091-25102.

299. Regan MR, Huang YH, Kim YS, Dykes-Hoberg MI, Jin L, Watkins AM, Bergles DE & Rothstein JD. 2007. Variations in promoter activity reveal a differential expression and physiology of glutamate transporters by glia in the developing and mature CNS. J. Neurosci. 27: 6607-6619.

300. Li Y, Schlamp CL & Nickells RW. 1999. Experimental induction of retinal ganglion cell death in adult mice. Invest. Ophthalmol. Vis. Sci. 40: 1004-1008.

301. McCarthy KD & de Vellis J. 1980. Preparation of separate astroglial and oligodendroglial cell cultures from rat cerebral tissue. J. Cell Biol. 85: 890-902.

302. Norton WT & Poduslo SE. 1973. Myelination in rat brain: method of myelin isolation. J. Neurochem. 21: 749-757.

303. Stevens B, Allen NJ, Vazquez LE, Howell GR, Christopherson KS, Nouri N, Micheva KD, Mehalow AK, Huberman AD, Stafford B, Sher A, Litke AM, Lambris JD, Smith SJ, John SW & Barres BA. 2007. The classical complement cascade mediates CNS synapse elimination. Cell. 131: 1164-1178.

304. Rasband WS. 1997-2014. ImageJ. U. S. National Institutes of Health. http://imagej.nih.gov/ij/.

305. Leighton SB. 1981. SEM images of block faces, cut by a miniature microtome within the SEM - a technical note. Scan. Electron Microsc. (Pt 2): 73-76.

306. Denk W & Horstmann H. 2004. Serial block-face scanning electron microscopy to reconstruct three-dimensional tissue nanostructure. PLoS Biol. 2: e329.

307. Walton J. 1979. Lead asparate, an en bloc contrast stain particularly useful for ultrastructural enzymology. J. Histochem. Cytochem. 27: 1337-1342.

308. Kremer JR, Mastronarde DN & McIntosh JR. 1996. Computer visualization of three-dimensional image data using IMOD. J. Struct. Biol. 116: 71-76.

309. Sun MG, Williams J, Munoz-Pinedo C, Perkins GA, Brown JM, Ellisman MH, Green DR & Frey TG. 2007. Correlated three-dimensional light and electron microscopy reveals transformation of mitochondria during apoptosis. Nat. Cell Biol. 9: 1057-1065.

Curriculum Vitae

Judy Van K. Nguyen	August 4, 2014

Educational History:

Ph.D. expected	2014	Program in Biochemistry, Cellular, and Molecular Biology - Neuroscience Mentor: Nicholas Marsh-Armstrong, Ph.D Johns Hopkins School of Medicine
B.S.	2006	Zoology and Biomedical Sciences University of Oklahoma

Other Professional Experience:

Research Rotation	2009	Lab of Solomon H. Snyder, MD Johns Hopkins School of Medicine
Research Rotation	2009	Lab of Mollie Meffert, MD-Ph.D Johns Hopkins School of Medicine
Research Rotation	2009	Lab of Jonathan Pevsner, Ph.D Johns Hopkins School of Medicine
Associate Research Assistant	2006-2008	Lab of Susannah Rankin, Ph.D Oklahoma Medical Research Foundation

Scholarships, fellowships, or other external funding:

2013	Travel Fellowship	International Society for Eye Research

Academic honors:

2006	Graduation with distinction	University of Oklahoma

Publications, Peer Reviewed:

Davis CH, Kim KY, Bushong EA, Mills EA, Boassa D, Shih T, Kinebuchi M, Phan S, Zhou Y, Bihlmeyer NA, **Nguyen JV**, Jin Y, Ellisman MH, Marsh-Armstrong N. (2014) Transcellular degradation of axonal mitochondria. Proceedings of the National Academy of Sciences. 1;111(26):9633-8. PMCID: PMC4084443.

Welsbie DS, Yang Z, Ge Y, Mitchell KL, Zhou X, Martin SE, Berlinicke CA, Hackler L Jr, Fuller J, Fu J, Cao LH, Han B, Auld D, Xue T, Hirai S, Germain L, Simard-Bisson C, Blouin R, **Nguyen JV**, Davis CH, Enke RA, Boye SL, Merbs SL, Marsh-Armstrong N, Hauswirth WW, DiAntonio A, Nickells RW, Inglese J, Hanes J, Yau KW, Quigley HA, Zack DJ. (2013) Functional genomic screening identifies dual leucine zipper kinase as a key mediator of retinal ganglion cell death. Proceedings of the National Academy of Sciences. 110(10):4045-50. PMCID: PMC3593842.

Nguyen JV, Soto I, Kim K, Bushong EA, Oglesby E, Valiente-Soriano FJ, Yang Z, Davis CO, Bedont JL, Son JL, Wei JO, Buchman VL, Zack DJ, Vidal-Sanz M, Ellisman MH, and Marsh-Armstrong N. (2011) Myelination transition zone astrocytes are constitutively phagocytic and have synuclein dependent reactivity in glaucoma. Proceedings of the National Academy of Sciences. 108(3):1176-81. PMCID: PMC3024691.

Wu FM, **Nguyen JV**, Rankin S. (2011) A conserved motif at the C terminus of sororin is required for sister chromatid cohesion. J Biology Chemistry. 286(5):3579-86. PMCID: PMC3030362.

Kornberg MD, Sen N, Hara MR, Juluri KR, **Nguyen JV**, Snowman AM, Law L, Hester LD, Snyder SH. (2010) GAPDH mediates nitrosylation of nuclear proteins. Nature Cell Biology. 12(11):1094-1100. PMCID: PMC2972384.

Conference presentations:

Nguyen JV, Davis CH, Bushong EA, Kim KY, Ellisman MH, Marsh-Armstrong N. (2013) Myelin degeneration and astrocyte phagocytosis in glaucoma. International Society for Eye Research, Sarasota Symposium. Sarasota, FL. October 2013. Oral.

Nguyen JV, Bushong EA, Kim KY, Ellisman MH, Marsh-Armstrong N. (2012) Alterations of lipid-related markers concides with astrocyte phagocytosis of axons. American Society for Neurochemistry. Baltimore, MD. March 2012. Poster.

Nguyen JV, Bushong EA, Kim KY, Karukonda P, Ganfornina MD, Sanchez D, Ellisman MH, Marsh-Armstrong N. (2011) Astrocyte phagocytosis of axons associated with alterations of lipid-related markers. Society for Neuroscience, Washington, DC. November 2011. Poster.